UNDERSTANDING AND DEVELOPING FIRE-THROUGH DIELECTRIC CONTACTS ON HIGHLY EFFICIENT SILICON SOLAR CELLS

by

Veysel Unsur

A dissertation submitted to the faculty of
The University of North Carolina at Charlotte
in partial fulfillment of the requirements
for the degree of Doctor of Philosophy in
Electrical Engineering

Charlotte

2018

Approved by:

Dr. Abasifreke Ebong

Dr. Edward Stokes

Dr. Yasin Raja

Dr. Tony Schmitz

ABSTRACT

VEYSEL UNSUR. Understanding and developing fire through dielectric contacts on highly efficient silicon solar cells. (Under the direction of Dr. ABASIFREKE EBONG)

Photovoltaic is a quick and efficient way of responding to the scarcity of fossil fuels and increasing environmental pollution. For the last two decades, photovoltaic technology has been the fastest growing industry among the renewable energy sources. However, the cost of per kWh of solar electricity is still the main challenge to be tackled. Cost and efficiency are the two opposing challenges that must be overcome for cost-effective solar electricity. Metallization is one of the key fabrication steps, especially for crystalline silicon solar cells which dominates the market, that can be tailored to reduce cost by using less silver along with fine gridlines while increasing the efficiency. Thus, the comprehensive investigation of the front grid metallization designs to reduce the amount of Ag used and the alternative such as Ni/Cu to reduce the cost of metallization even further have been carried out.

Firstly, a comprehensive empirical grid model was first established to investigate the front grid designs with 3-, 4- and 5 busbars. The results are compared to numerical analysis using Griddler 2-D modeling program. A combination of segmented tapered metal grids (SG) and uneven busbars (UEB) led to increased short circuit current density (J_{SC}) and open circuit voltage (V_{OC}) without sacrificing the fill factor (*FF*). The 5-busbar SG-UEB combination resulted in ≥ 20 % efficient

Al-BSF and ≥21 % PERC solar cell. The results demonstrated that, in addition to high efficiency, the cost of front Ag metallization can be reduced by 1.4¢ per cell through SG-UEB combination as opposed to non-segmented approach.

Secondly, the front designs were implemented taking into account the impact of Ag paste composition and sintering on contact and series resistance, which tend to impact the FF. The Ag paste used in the experiments had the right composition to result in (i) narrow gridlines according to the screen design, after printing (ii) low contact and gridline resistances after sintering. This resulted in PERC structure efficiency of ~21%. Noted in the used paste, according to the SEM study, is the Ag crystallites, which tend to be more when nano Ag particle is used than the micro Ag particle counterpart. Also, gridline porosity is reduced by use of nano Ag particle in the paste as well as the contact resistance from high density and uniform Ag crystallites with very thin (~ 0.1 nm) glass layer.

Thirdly, having established the baseline process to achieve ~21% PERC cell with a belt speed of 230 IPM in the infrared belt rapid thermal annealing furnace, the impact of belt speed on the cell performance was investigated. Since rapid thermal processing (RTP) is a key technology in the screen-printed Ag paste contacts to silicon solar cells; the ramp up and ramp down rates, which depends on belt speed, were investigated. It is noted that, the faster the belt speed the shorter the dwell time, which enhances the front contact quality. By doubling the belt speed from 180 to 375 ipm, the V_{OC} was observed to increase by ~5 mV along with ~1-2 % absolute increase in fill factor with zero cost to production. Thus, by doubling the

belt speed, higher efficiency is obtained and cost is conserved. This is one of the ways to further decrease cost of production with increased output performance.

Finally, in quest to reduce cost further, starting with metallization cost, alternative to Ag, Ni/Cu is a contender. However, aerosol jet printing, which is a non-contact printing method, may be explored instead of screen-printing to maintain control over gridline width and height. Aerosol printing is a high throughput process that can easily be integrated into commercial silicon solar manufacturing. Gridlines of silver frit, nickel frit, silver/nickel stacks, and silver/nickel/copper stacks were investigated as a first approach. The Ag Frit/Ni/Cu stack displayed ~19% pseudo efficiency with ~85% pFF and gridlines of 100 μm wide, and 3.25 μm height. However, the Ni frit ink showed better adhesion over the Ag counterpart. This is quite fascinating preliminary results, which suggests that the Ni/Cu is a good candidate as alternative to Ag. Ni is lower cost than Ag and can provide up to 30% cost reduction in manufacturing.

ACKNOWLEDGEMENTS

First of all, I would like to express my feelings that I am grateful to find an opportunity to work on solar cells that, somehow I believe, is going to change the direction of humanity towards the greater good. And it would make me deeply appreciate, if this study contribute to that purpose in any way possible.

Next, I would like to thank Dr. Abasifreke U. Ebong, the principal investigator of this study and my academic advisor. It has been long and fruitful journey during my M.Sc and Ph.D degrees with him. In addition, I would like to thank Dr. Yasin Raja, Dr. Ed. Stokes, and Dr. Tony Schmitz for taking the time to serve on my dissertation committee and for helping to improve my understanding of scientific research.

Finally I would like to thank my family for their support and compromise that has allowed me to achieve my goals.

TABLE OF CONTENTS

LIST OF FIGURES

LIST OF TABLES

LIST OF ABBREVIATIONS

2D	two-dimensional
3-BB	3-busbar
4-BB	4-busbar
5-BB	5-busbar
Ag	silver
Al	aluminum
ARC	antireflection coating
a-Si	amorphous silicon
BBR	busbar to busbar resistance
BOS	balance of system
BSF	back surface field
BSRV	back surface recombination velocity
CdTe	cadmium telluride
CIGS	copper indium gallium selenide
CO_2	carbon dioxide
¢/W	cent per wattage
c-Si	crystalline silicon
CZ	Czochralski
DP	double-printing
EL	electroluminescence
EQE	external quantum efficiency

EWT	emitter wrap through
FBR	front busbar resistance
FF	fill factor
FSF	front surface filed
FSRV	front surface recombination velocity
FZ	float-zone
HIT	heterojunction with intrinsic thin-layer
IBC	interdigitated back contact
IPM	inch per minute
IQE	internal quantum efficiencies
ITO	indium tin oxide
J_L	light-generated current density
J_{o1}	saturation current density
J_{o2}	junction reverse saturation current density
J_{ob}	base saturation current density
J_{oe}	emitter saturation current density
J_{sc}	short circuit current density
LCOE	levelized cost of electricity
LID	light-induced degradation
LIV	light current voltage
LPS	liquid phase sintering
MIS	metal insulator semiconductor
MWT	metal wrap through

PC1D	Computer program for one dimensional modeling
PC2D	Excel-based program for two dimensional modeling
PECVD	Plasma-enhanced chemical vapor deposition
PERC	passivated emitter and rear cell
PERL	passivated emitter with rear locally diffused
PSG	phosphosilicate glass
R_s	series resistance
SEM	scanning electron microscopy
SiN_x	silicon nitride
SiO_2	silicon dioxide
SP	single-printing
SRV	surface recombination velocity
STC	standard test condition
TBW	total busbar width
TCO	transparent conductive oxide
V_{OC}	open circuit voltage

CHAPTER 1 :
INTRODUCTION TO PHOTOVOLTAICS

1.1 Energy and Humanity

Energy as a word itself originates from the Greek "enérgia", first developed by Aristotle, and refers to "being at work". Energy is defined in various ways: it is the conserved quantity of matter and space in physics; it is a property of a substance that stems from its atomic structure in chemistry; and it is an electric charge that lets work to accomplished in electrical engineering. Regardless of its definition, the supply and demand of energy has determined the level of global development in every sphere of human activity. Thus, energy consumption in today's world can be a great indicator of a country's advancement level. Figure 1.1 demonstrates the relationship between electricity consumption[1] and the human development index (HDI) for selected countries[2] worldwide as of 2015. HDI [1] is a metric that indicates the quality of life in such terms as life expectancy, education level, and technology introduced by the World Bank. It can be concluded from Figure 1.1 that energy fuels the development in which quality of life rises in the index as energy usage increases. Figure 1.2 shows electricity consumption against per capita income instead of HDI in order to quantify the development. The same conclusion can be extracted that the energy usage also fuels the per capita income. Figure 1.2 also illustrates the reality that more than 70% of the world population does not demand the same

[1] Even though there are different types of energy being consumed by human being, specifically electricity consumption is being considered in this example.
[2] These countries are selected randomly from each continent to show a general picture.

amount of energy compared to their counterparts. The expectation is that there will be a drastic increase in demand of electricity as these countries (in the circle), especially Asia and Africa, reach developed-country levels in the near future.

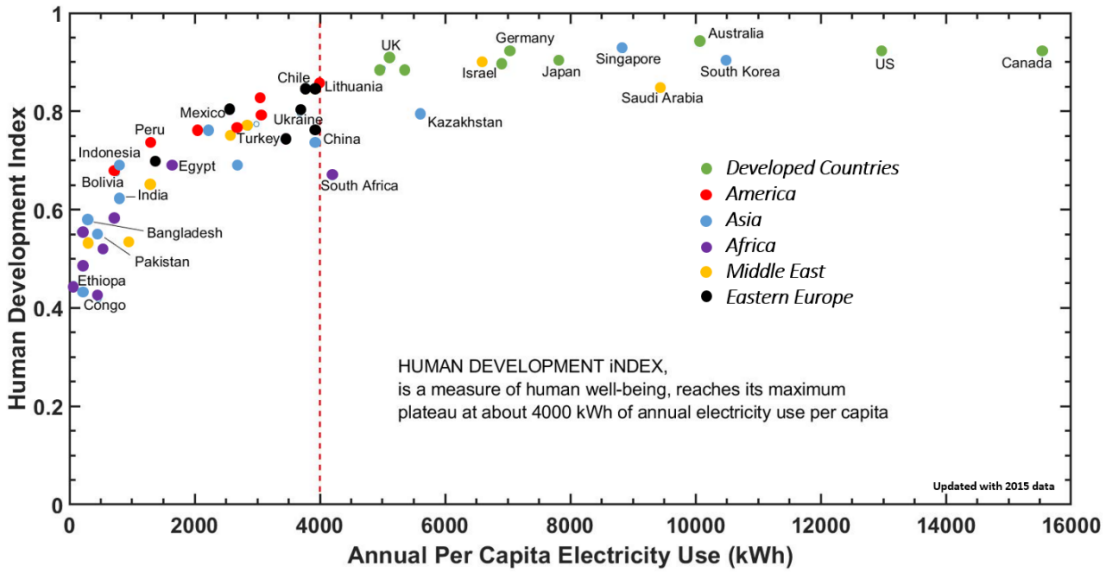

Figure 1.1: Human development index vs. per capita electricity use for selected countries as of 2015

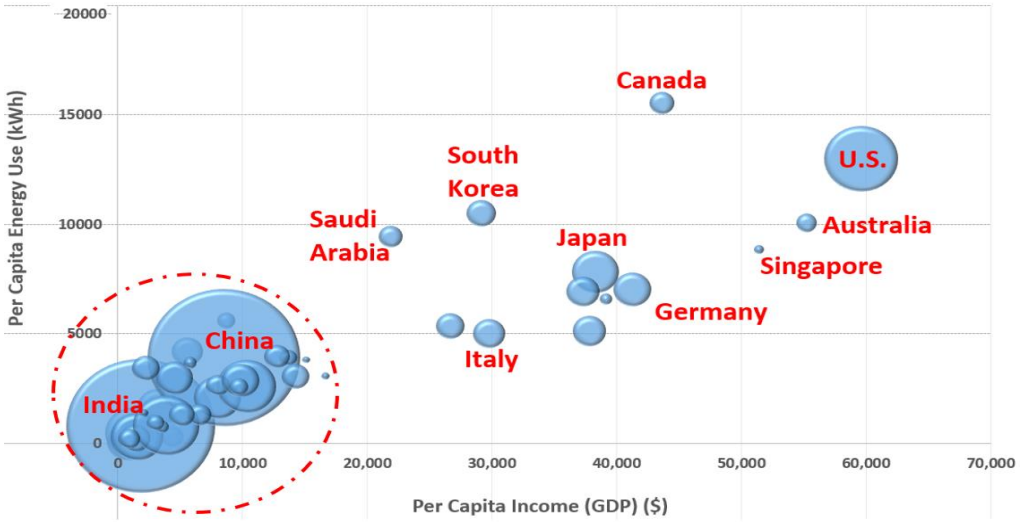

Figure 1.2: The relationship between GDP and energy consumption for selected countries. The size of the bubbles in this chart indicates the size of the population of the countries.

The main source of energy for the world's ever-increasing demand had been biomass until mid-19th century, and then carbon-based coal, petroleum, and natural gas has gained dominance. Since then, there has been a substantial dependency on extracted fossil fuels as energy sources. This dependency carries the risks of discontinuity of the supply due to scarcity of resources, as well as the environmental pollution. The effects of fossil fuel usage on the environment has been discussed and articulated by different international institutes [1-3]. According to the fifth Intergovernmental Panel on Climate Change (IPCC) Report [4], carbon dioxide (CO_2) is the most important anthropogenic greenhouse gas produced by combustion of fossil fuel (see Figure 1.3). Emission of CO_2 from fossil fuel combustion and industrial processes contributed about 78% of the total greenhouse gas emission increase from 1970 to 2010, with larger absolute increases from 2000 to 2010 [4]. Although the direct and primary effects of the pollution on human beings have received more focus, the indirect effects through ecological change could be far more devastating. Figure 1.4 [5] shows the increase in surface temperature for the last century, which decreases the solubility of oxygen in water. This subsequently results in the population of species starts to diminish as the temperature increases.

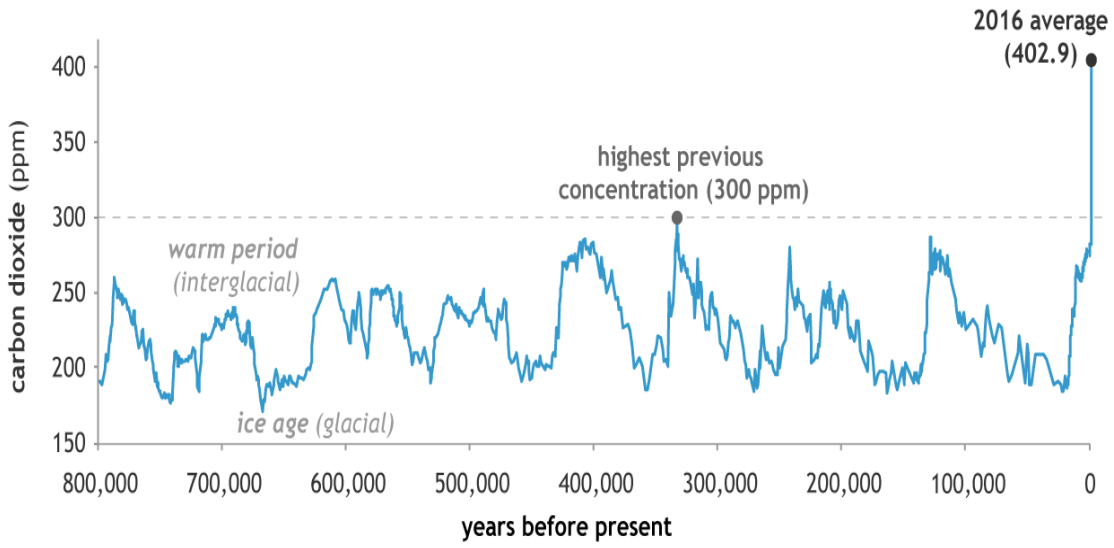

Figure 1.3: Atmospheric carbon dioxide concentrations in parts per million (ppm) for the past 800,000 years, based on EPICA (ice core) data

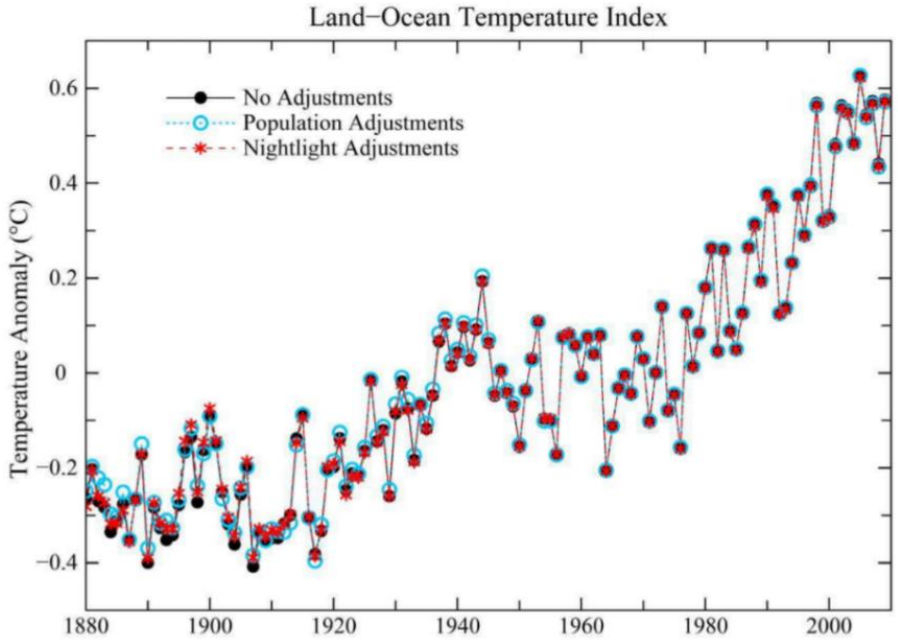

Figure 1.4: Annual mean land-ocean temperature index

In conclusion, the adverse outcomes of global warming caused by the energy supplied from fossil fuels seem to be faced in the very near future. One quick and efficient way of responding to this problem is to harvest the Sun as an energy source.

The sun is a clean, free, and inexhaustible source of energy. It incidents 120,000 TW of radiation on the surface of the Earth [6], which is sufficient to power today's world ~25,000 times. A solar insolation (kWh/m²) map of the world is shown in Figure 1.5, while Figure 1.6 shows the insolation for different countries against HDI. It is both surprising and fortunate that the countries ranked at the bottom of the development index are at top of the insolation map. Therefore, not only will utilization of solar energy solve the world's energy problem, but also it will help with poverty and environmental problems.

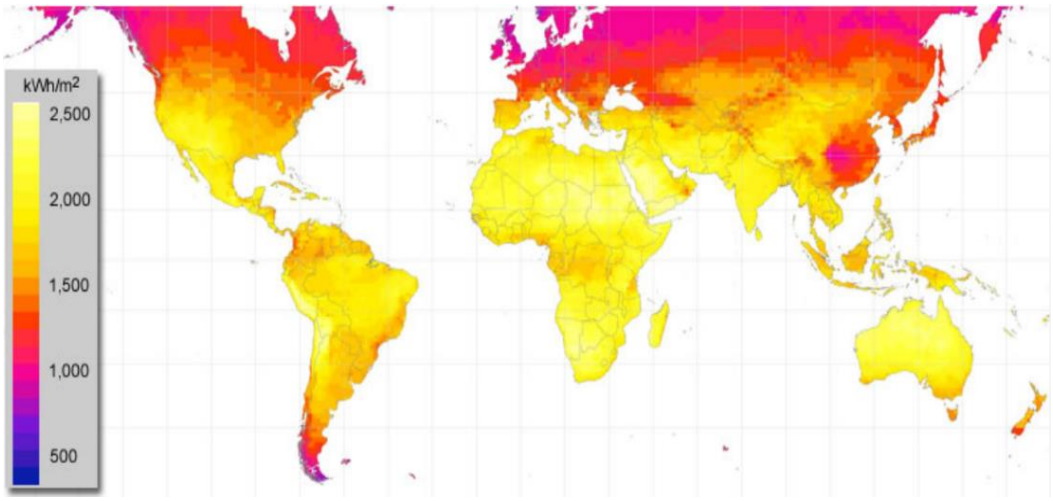

Figure 1.5: Solar insolation (kWh/m²) map for the world

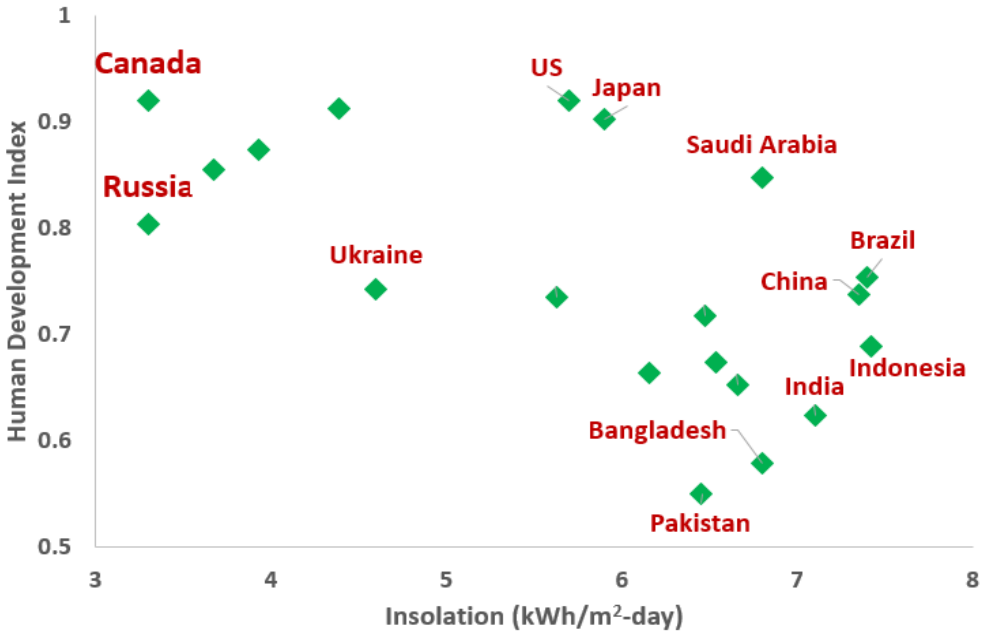

Figure 1.6: HDI vs insolation (how much sun-hour throughout the day) for different countries

1.2 Photovoltaics

Photovoltaic device is one particular embodiment of solar energy where it converts sunlight into electricity without generating any polluting by product. The discovery of photovoltaic effect is credited to French physicist Alexandre Edmond Becquerel, who conducted an experiment in 1839 referred as "*Action of Radiation on the Metal Blades*" [7]. Soon after, in 1877, Adams and Day successfully repeated the experiment in a selenium (Se) solid system [8]. In 1883, Fritts was able to prepare a thin Se film as a "thin film" photovoltaic device. More than a century after photovoltaic effect discovery, Bell Labs announced the invention of the first embodiment of modern silicon solar cell with an efficiency of 6% in 1954 [9]. Since

then, the rapidly expanding photovoltaic industry has reached to 400 GW in 2017 (see Figure 1.7 [10]).

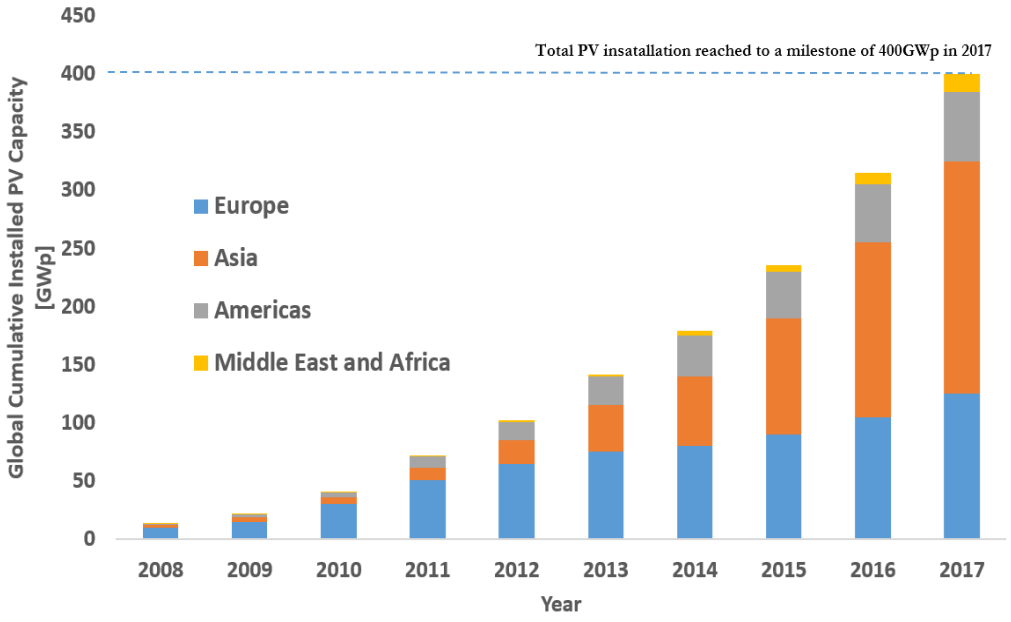

Figure 1.7: Evolution of PV penetration and total PV installed capacity from 2005 to 2017

From the 1950s onwards, different solar cell concepts and semiconductor materials were investigated and the conversion efficiency and module power was steeply increased. The industry has been dominated by mono- and multi-crystalline silicon solar cells that represent more than 90% of the global PV market and production capacity in 2017, as shown in Figure 1.8 [11]. A variety of silicon solar cell concepts with the purpose of high conversion efficiency and low cost processing flow have been introduced.

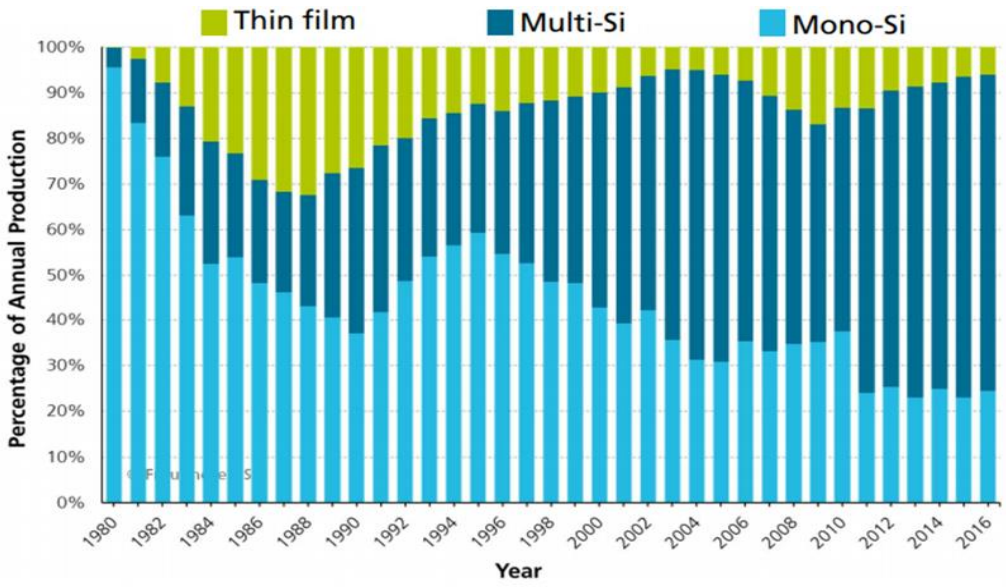

Figure 1.8: PV module production capacity share based on different technologies

1.3 Crystalline Silicon Solar Cell Technologies

A solar cell operates in the order of light absorption, charge excitation, charge separation and lastly charge collection. In order to absorb the light and to excite the charges an emitter at the device is formed. Charge separation occurs at the p-n junction and metal electrodes are accountable for charge collection. Basically, a solar cell is a p-n junction device that absorbs photons and converts them directly to electrons. Figure 1.9 shows the basic schematic of a solar cell. As a base material, p-type material is used while the emitter is n^+ diffused. When the cell is illuminated from the emitter side, charges (electrons and holes) are generated and separated at the depletion region of the p-n junction towards contacts. The electrons move towards the front while the holes are transported to the back contacts. This movement creates a voltage inside the device and when it is connected to a load, the

electrons can be extracted at the front contacts and a current flows through the external load.

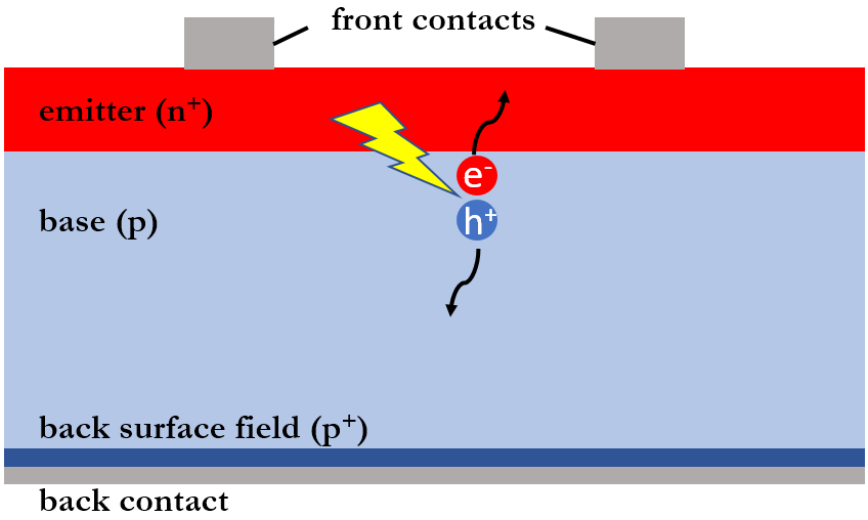

Figure 1.9: Schematic diagram of a simple solar cell with p-type base n-type emitter

In order to either increase the efficiency or decrease the cost of a device, different cell architectures are introduced (see Figure 1.10). The most common industrial cell concept is the aluminum back surface field (Al-BSF) because of its simplicity and fewer processing steps. The passivated emitter rear cell (PERC) concept using p-type base as the Al-BSF is also expected to be major cell technology in the near future [12]. Therefore, these two concepts will be the focus of this dissertation.

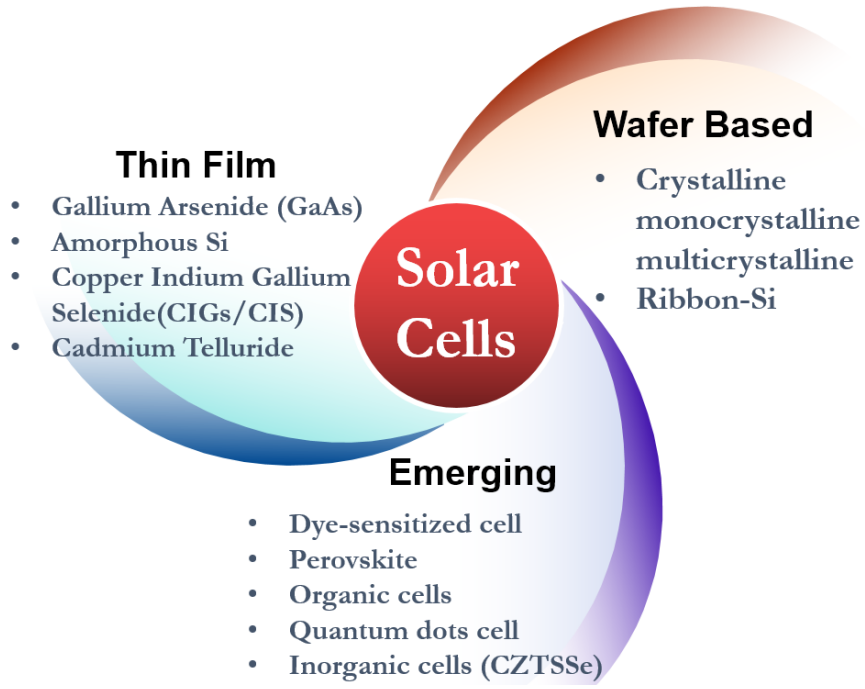

Figure 1.10: Different solar cell architecture categories

1.3.1 The Al-BSF Design

The full Al-BSF cells are characterized by p-type textured mono/multi crystalline silicon (Si) wafer base, an anti-reflection coating (ARC) and passivation layer of SiN_X and lastly screen printed silver (Ag) front and aluminum (Al) back contacts. Fully printed Al on the backside alloys with silicon during contact co-firing and forms a layer of p^+ called back surface field (BSF), see Figure 1.11. The normal cell-processing sequence consists of:

(i) saw damage removal, chemical texturing and cleaning;

(ii) phosphorus diffusion;

(iii) phosphorus glass (PSG) removal and edge isolation;

(iv) silicon nitride (SiNx) deposition for front surface AR-coating;

(v) front Ag paste screen-printing and drying;

(vi) rear Al/Ag screen-printing and drying;

(vii) co-firing of screen-printed metal electrodes;

(viii) cell light current voltage (LIV) testing and sorting.

While the conversion efficiency of Al-BSF cells is around 20% in cell level [13], the module efficiencies are still 16-17%.

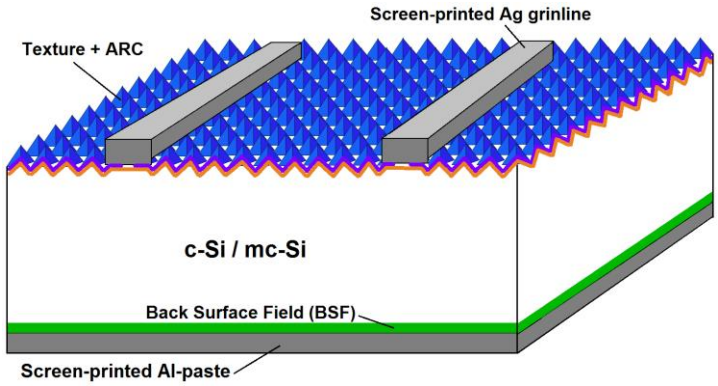

Figure 1.11: A schematic structure for conventional solar cell with full Al-BSF

The homogeneous doping of emitter and the BSF formation on the backside are its main conceptual advantages. The requirement of low resistance ohmic contacts, on the other hand, entail a high doping concentration on the emitter which leads to high front surface recombination losses. Also, full area back contacts leads to high back surface recombination velocities. Although, Al-BSF design has a very simple processing flow (meaning lower cost), the efficiency suffers from the above-mentioned flaws of the design.

1.3.2 The PERC design

In order to decrease the recombination on the backside due to full aluminum, PERC concept embraces as an extra passivation layer of SiO_X/AlO_X on the back side compared to the Al-BSF. Since there is an AlO_X stack as a dielectric to enhance thermal and radiation stability, local openings on the passivation layers are formed via laser ablation to ensure the Al contact can make a connection with silicon (see Figure 1.12). Today, industrial PERC cell's efficiencies are exceeding 22% [14, 15] and there are convincing roadmaps of efficiencies reaching to 24% [16].

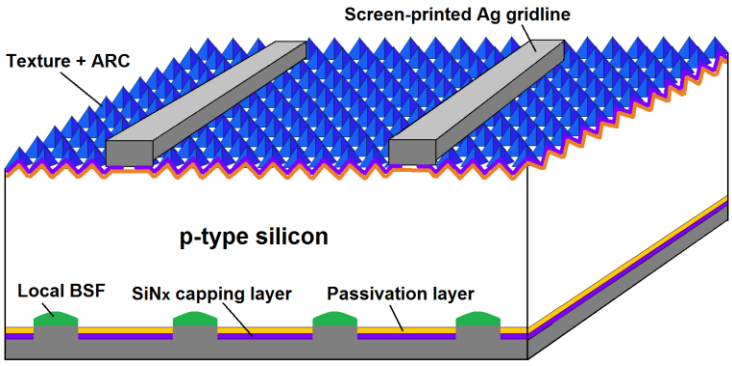

Figure 1.12: A schematic structure for PERC cells

1.4 *IV* Characteristics of a Solar Cell

Efficiency (η) is the key metric for a solar cell and it is the product of three electrical parameters; short circuit current (I_{SC}) open circuit voltage (V_{OC}) and fill factor (FF). A typical solar cell behaves like a traditional diode whose equivalent circuit is shown in Figure 1.13. An ideal solar may be modelled by a current source in parallel with a diode. However, no solar cell is ideal, so a shunt resistance (R_{SH}) and a series resistance (R_S) components are added to the model.

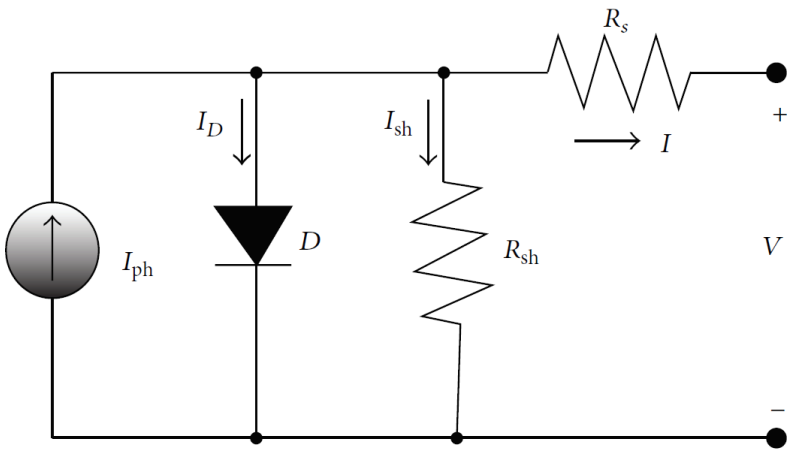

Figure 1.13: Single diode equivalent circuit of a solar cell

The IV characteristic of an ideal cell is defined by the one-diode equation;

$$I = I_0 \cdot \left(e^{\frac{q \cdot V}{k \cdot T}} - 1\right) - I_{sc} \tag{1.1}$$

where I is the net current flowing through the diode, I_o is the saturation current, k is the Boltzman constant, q is the carrier charge, T is the temperature, and V is the applied voltage across the terminals of the diode When there is no current flow, the condition of open circuit, the V_{OC} can be obtained as;

$$V_{oc} = \frac{k \cdot T}{q} \cdot \ln\left(\frac{I_{sc}}{I_0}\right) \tag{1.2}$$

As shown in Figure 1.14, the FF corresponds to the ratio of the rectangular areas beneath the light IV curve. The ratio of the maximum power Pmpp (Vmpp·Impp) and the product of V_{OC} and I_{SC} is defined as fill factor;

$$FF = \frac{V_{mpp} I_{mpp}}{I_{sc} V_{oc}} \tag{1.3}$$

With all these three electrical output parameters of a solar cell, the conversion efficiency can be defined as;

$$\eta = \frac{P_{mpp}}{P_{light}} = \frac{I_{sc} \cdot V_{oc} \cdot FF}{P_{light}} \tag{1.4}$$

Figure 1.14 shows the typical dark and light IV curves of a solar cell. From a dark IV curve, series resistance is the slope in the first quadrant and depends on resistances of bulk semiconductor and contacts. Shunt resistance, on the other hand, can be derived from the slope at near-zero voltage, and depends on material defects in semiconductor. From a light IV curve, maximum current and voltage (Imp and Vmp), the I_{SC}, the V_{OC}, and the FF can be extracted.

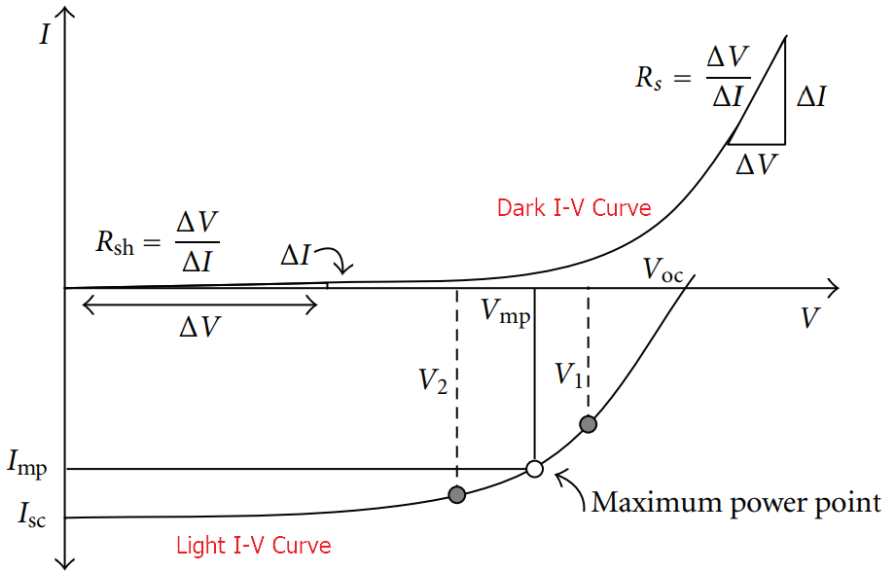

Figure 1.14: I-V characteristic of a solar cell. Rs is the series and Rsh is the shunt resistances

1.5 The Loss Mechanisms in a Solar Cell

The maximum conversion efficiency of an ideal silicon solar cell is calculated to be 29.8% [17, 18] after excluding fundamental losses such as atmospheric filter on the incident sunlight and photons that have energy less than the material's band

gap. The best mono-crystalline silicon solar cell fabricated in a research lab efficiency is 24% [19]. On the other hand, commercial solar cell's efficiencies are significantly lower than lab efficiencies. In a non-ideal solar cell, there are additional loss mechanism that leads to power losses by reducing one (or more) of electrical output parameters that cause to lower efficiencies. These mechanisms can be brought to three main categories of optical, resistance, and recombination losses.

Optical losses arise from reflection on the illuminated surface and shading caused by metallization and module design. The loss of incident light leads to a reduced I_{SC} and hence lower efficiency. There are ways to overcome optical losses such as texturing the illuminated surface and applying anti reflection coating (ARC) layer to reduce the reflection. Texturing the front surface bring downs the reflection to ~10% compared to ~35% of a flat silicon surface (see Figure 1.15). ARC layer also helps further reducing the reflection to around ~5%. The thickness of the ARC layer must be properly designed to avoid absorption in the ARC, which does not contribute to current collection

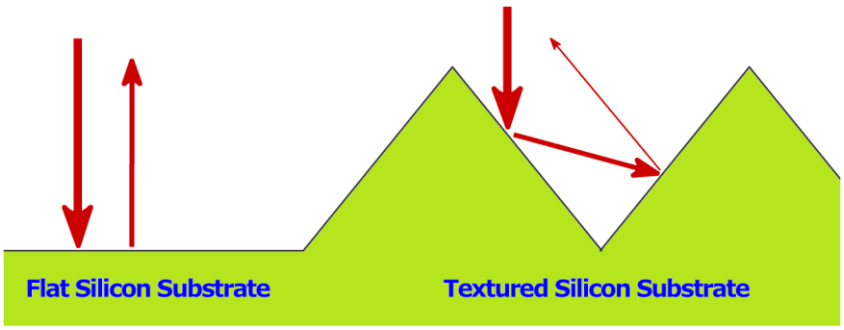

Figure 1.15: Flat surface and textured surface are compared. Texturing gives light more than one chance to be absorbed that leads to less reflection

The resistance losses can be considered as series resistance (R_S) and shunt resistance (R_{SH}). The R_S comprises six components of gridline ($R_{Gridline}$), busbar (R_{Busbar}) contact ($R_{Contact}$), emitter ($R_{Emitter}$), base (R_{Base}), back contact ($R_{Bcontact}$) resistances (see Figure 1.16). Three of which are ohmic resistances within the metal contacts and the other three are material-related resistances. R_{SH} is the leaking currents at the edges of the solar cell as well as interruptions of the p-n junction that may be caused by insufficient emitter diffusion or deep metal diffusion towards the junction etc.

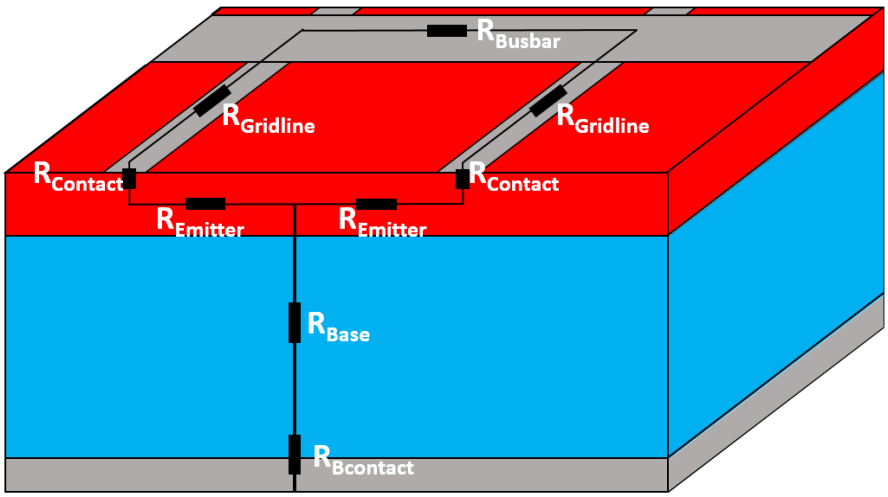

Figure 1.16: Series resistance components shown in a finished cell

Recombination losses occurs when the photogenerated charge carriers (electrons and holes) recombine with one another before the electrons reach to the load. The understanding of which is crucial so that the V_{OC} is not affected and hence the efficiency. It happens mainly in the bulk, front and back surfaces. Figure 1.17 shows the three common recombination mechanisms in a solar cell. Radiative recombination occurs when an electron shifts from conduction band to valance

band, Shockley-Reed-Hall takes place via an extra energy level[3] in the band gap and finally Auger recombination happens when one electron in the conduction band recombines with a hole in the valance band and give its energy to second electron in the conduction band. Using high quality bulk material to keep the Shockley-Reed-Hall low is one solution to have high V_{OC}. Surface passivation to deactivate the dangling bonds on the surfaces and having a BSF region are to keep other recombination losses as low as possible.

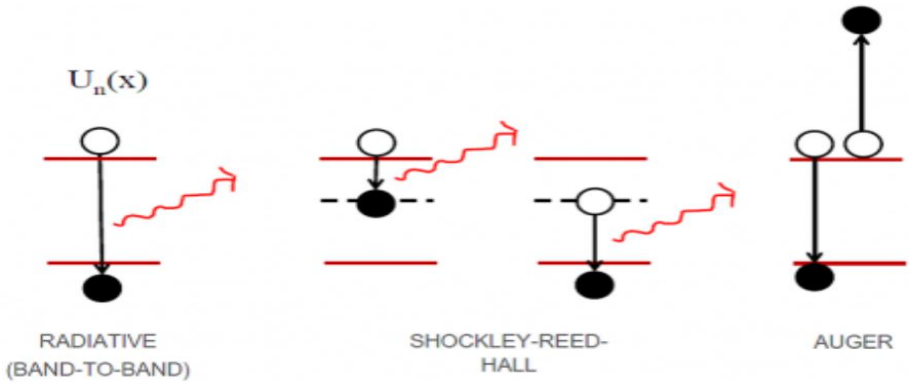

Figure 1.17: Three common recombination types.

1.6 Statement of the Problem and Motivation

The advantages of photovoltaics over fossil fuel counterparts lend itself to being the ultimate energy source. For the last two decades, photovoltaic technology has been the fastest growing industry among the renewable energy sources. Continuing at the present growth rate of ~ 40% for the next two decades will allow photovoltaics to be the world's largest energy source. However the levelized cost of

[3] Extra energy level in a band gap is caused by defects in a semiconductor material such as doping impurities, foreign atoms (iron) etc.

electricity (LCOE) for solar must decrease below \$50/MW_h (or <5 ¢/kWh) with no governmental subsidies in order to render solar cell technologies economically competitive according to the Department of Energy SunShot program [20-22]. Today the manufacturing cost of PV can be broken down into four categories including (i) 37% module fabrication, (ii) 16% wafer, (iii) 24% polysilicon, and (iv) 23% cell processing [12]. And cell processing cost itself can be broken down into 10% of texturing, 23% of pn junction formation, 12% of ARC deposition and 55% of metallization [23].

The best way to achieve competitive solar electricity is to either increase the efficiency or/and decrease the cost of manufacturing, or/and improve the reliability of solar cells. And the challenges to obtain this reliable and high efficient solar cell at low cost include

(i) manufacturing high quality, large area, and thin silicon wafers with no negative impact on the performance,

(ii) improving metallization quality and maintaining low cost, and

(iii) implementing simple and low cost processing sequence.

In this dissertation, the focus will be specifically on cost effective metallization in order to establish fine gridline structure which minimizes shading with increased throughput and efficiency.

The metallization impacts the performance of a solar cell electrically and optically. Electrically, the inherent resistance of the front metal gridlines and their

contact with emitter impacts the series resistance (R_S). Optically, the metal front gridline coverage contributes to shading, which directly, influences the I_{SC}. Depending on the design and printing quality of the metal electrodes, the gridline geometry (width, height, continuity, and separation) can make or break the cell performance. This geometry is a function of the metallic paste and printing technique. Thus, forming high quality contact to solar cells is inevitable to achieving high efficient solar cells.

This dissertation, therefore, addresses the most important processing step, "the metallization" in fabricating a solar cell, in a cost-effective fashion with improved energy conversion efficiency. This is done through a step-wise methodology including

(i) design and modeling of front screen-printed contact patterns,

(ii) fabrication of commercial size silicon solar cells with PERC and Al-BSF structures,

(iii) investigation of the effect of rapid thermal firing on the electrical output performance and followed by,

(iv) electrical and structural characterization, and analyses.

CHAPTER 2 :
FIRE THROUGH DIELECTRIC METALLIZATION TECHNIQUES FOR SOLAR CELLS

2.1 Introduction

The quality of metal contacts to a semiconductor is controlled by the magnitude of potential barrier height between metal and semiconductor, which prevents electrons from passing from one to the other (see Figure 2.1). The potential barrier results from the difference between the minimum energy needed to take an electron from the interior to outside of the metal (work function) and the minimum energy required to move an electron from the bottom of the conduction band to the vacuum level (the electron affinity of semiconductor). To achieve minimal resistance across the metal-semiconductor contact, the work function of the metal must be close to (or smaller) than the sum of electron affinity and the bandgap energy [24, 25].

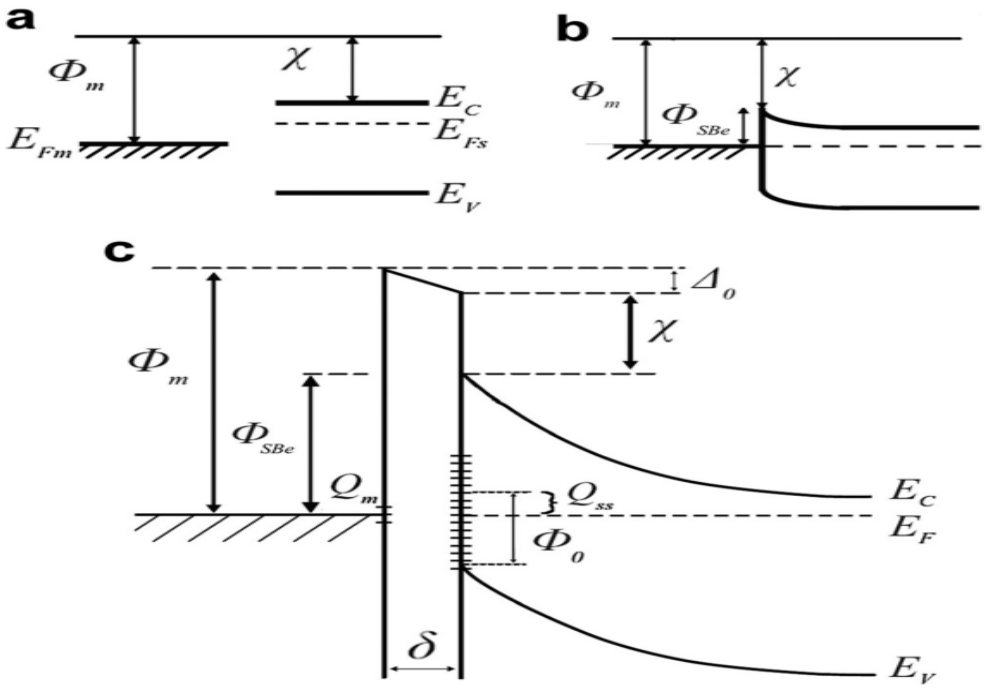

Figure 2.1: (a) Energy band diagram before contact is made between a metal and a semiconductor. (b) When contact is made, the Fermi levels equilibrate and a Schottky barrier arise. (c) Energy band diagram of a contact between metal and a semiconductor with interface states in the band gap at the semiconductor surface

Every semiconductor device requires an ohmic contact to enable carriers to be collected without any power loss. A solar cell requires two polarity-biasing because the current on the surface of a solar cell flows laterally between the gridlines. It is challenging to find a suitable metal for Si since every solar cell requires an ohmic contact that leads to minimum resistance. Figure 2.2 [26] shows the work function for different metal and semiconductors. While Si has ~4.05 eV electron affinity, silver (Ag) and aluminum (Al) have 4.26 eV and 4.28 eV respectively, which makes them an appropriate applicant to be contacts to the Si. Therefore Ag for the front and Al for the back contacts are vastly used for contact formation in the industry.

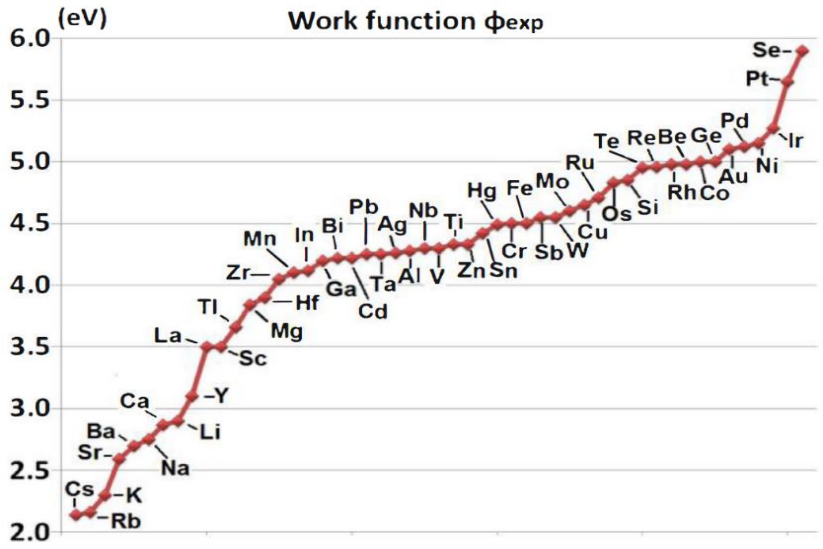

Figure 2.2: Plot of experimental work functions for different elements.

There are different technologies for contact formation in solar industry such as photolithography, laser grooving and fire through dielectric (FTD) with printed metal. Having to use UV light source for photolithography and laser for laser grooving followed by plating makes these processes expensive and complicated. Thus, the FTD stands out as a viable method, which will be focus of this work. Fire through dielectric is the process in which a metal paste, typically Ag containing, is printed on the surface and is fired through the dielectric in order to form the contact between metal and semiconductor. The printed contacts etch through the dielectric to the silicon surface and penetrate below the Si peak surface concentrations of phosphorus (or boron). There are many methods that use the FTD technology. As shown in Figure 2.3 this technology can be categorized as impact and non-impact. However, screen printing is widely adopted because of its low cost, high throughput and simplicity in addition to maturity. A quick review of the literature on all these

technologies is given her to further support why screen printing is the technology of choice for dispensing the gridlines for the FTD contacts in this work.

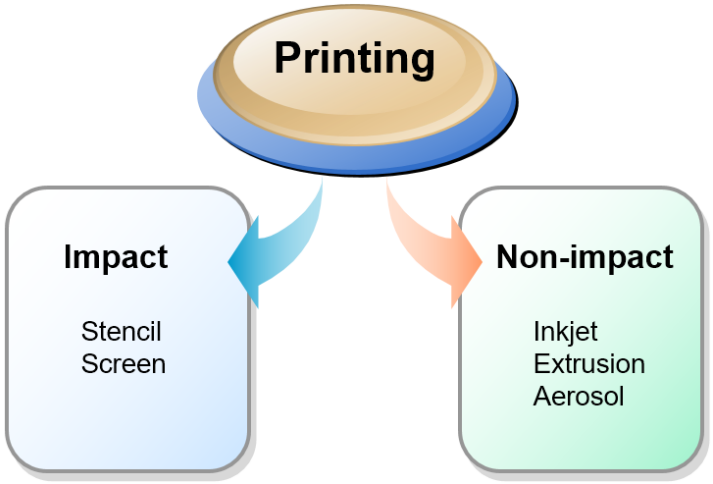

Figure 2.3: Printing technologies separated into impact and non-impact printing

2.2 Non-Impact Printing

The advantages of non-impact printing include the processing of thin silicon solar cells to reduce cost of Si in addition to precision in the gridline width and uniformity over a cell. The non-impact enables the use of nano-particle size Ag, which can lead to large area contacts and near-bulk resistivity for low series resistance.

2.2.1 Aerosol Printing

Aerosol technology, developed by Optomec, Inc., USA (see Figure 2.4 [27]) depends on the aerodynamic focusing of an aerosol that consists of ink droplets entrained in a carrier gas to form deposition.

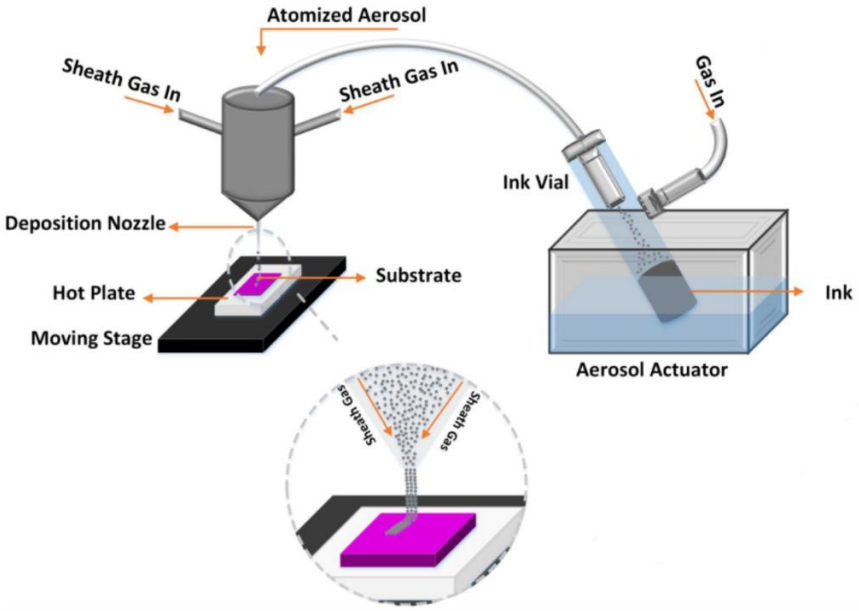

Figure 2.4: Aerosol printing setup illustration

Gridlines and busbars can be printed at the ambient temperature without mask or stencil via aerosol technology. Gridline widths between 18 µm and 60 µm have been produced with aerosol systems [28]. The narrow, high integrity gridlines have higher conductivity, low shadowing effect, which led to low series resistance, increased FF, and $J_{SC,}$ and hence the efficiency Aerosol technology can be used in conjunction with thinner wafers because there is no impact, thus breakage is never the case as in screen printing technique.

Table 2.1 shows a comparison between screen and aerosol printing. The aspect ratio which aerosol printing may provide is far more greater than screen printing, which results in low contact resistance. It also benefits from using nano Ag particles so that the gridline resistance can be improved by sintering. The

disadvantage of the system, on the other hand, is its complexity and non-integrability to existing production lines easily.

Table 2.1: The comparison of aerosol printing with screen printing

	Aerosol Printing	Screen Printing
Aspect Ratio (height/width)	~ 0.65	~ 0.25
Best Efficiency	18.2%	20.15%
System's Throughput	Medium	High
Ag Particle Size	Nano	Macro
Ease of Implementation	Hard	Easy
Finished Product	Yes	Yes

2.2.2 Inkjet Printing

Inkjet can broadly be defined as a process where individual droplets of liquid are ejected through an orifice in a controlled manner [29]. As an attractive alternative to screen-printing or vacuum evaporation for the fabrication of the front contacts to solar cells, the digital inkjet printing (DIP) is the most promising method [30].

With inkjet printing of metal inks, gridline widths of 20μm, which results in significant reduction in shading losses and $R_{Contact}$ compared to screen printing can be achieved. This implies better gridline resolution and improved aspect ratios for the conducting gridlines.

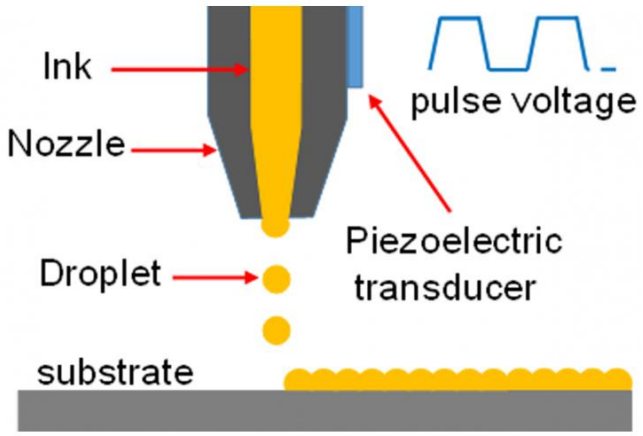

Figure 2.5: Inkjet printing setup illustration

Table 2.2 shows the comparison between screen and inkjet printing. Inkjet printing can achieve higher aspect ratios than screen printing, as all other nozzle system printing techniques. It also utilizes nano Ag particle paste which can help with gridline resistance. Although inkjet printing is a promising alternative method, the machinery that is fully capable to handle mass productions is yet to exist. Also, there is no commercial equipment that can support high throughput ink dispensation.

Table 2.2: The comparison of inkjet printing with screen printing

	Inkjet Printing	Screen Printing
Aspect Ratio (height/width)	~ 0.55	~ 0.25
Best Efficiency	18.9%	20.15%
System's Throughput	High	High
Ag Particle Size	Nano	Macro
Ease of Implementation	Hard	Easy
Finished Product	No	Yes

2.3 Impact Printing

The advantages of impact printings include being unsophisticated process, high throughputs, and its low cost. Even though the quality of contacts is not as much of contactless printing counterparts, the trade-off between cost and efficiency is being made.

2.3.1 Extrusion Printing

The working principle of the extrusion printing is relative movement between print head and wafer with an actively controlled print gap, while a defined paste compound volume extruded behind the nozzle, see Figure 2.6. Using the principle of hydrodynamic focusing, it is possible to extrude a metal paste structure smaller than all other lateral dimensions within the paste flow channel [31].

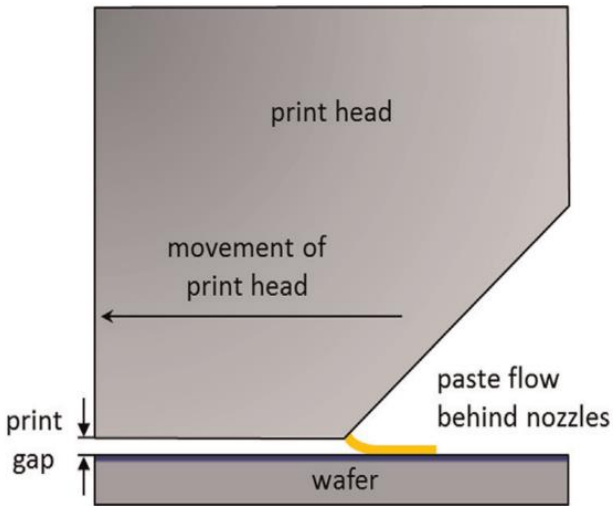

Figure 2.6: Extrusion printing setup illustration

Table 2.3 shows the comparison between screen printing and extrusion printing. Although it seems a promising way to have contacts with high aspect ratios, the main reason why extrusion is not adopted is its costs

Table 2.3: The comparison of extrusion printing with screen printing

	Extrusion Printing	Screen Printing
Aspect Ratio (height/width)	~ 0.40	~ 0.25
Best Efficiency	18%	20.15%
System's Throughput	Low	High
Ag Particle Size	Macro	Macro
Ease of Implementation	Hard	Easy
Finished Product	No	Yes

2.3.2 Stencil Printing

Stencil printing has been used mostly in circuit board manufacturing. It was first introduced by [32, 33] in solar cell industry. The main advantage of stencil printing over screen-printing is the ability to print finer lines with a higher aspect ratio and the non-wear character of the stencil. Unlike screens with wire mesh, a stencil features 100% open area in the gridline openings (see Figure 2.7 [34]), which leads to an excellent paste transfer and printed line height uniformity when compared with a mesh screen open area of around 60% [35].

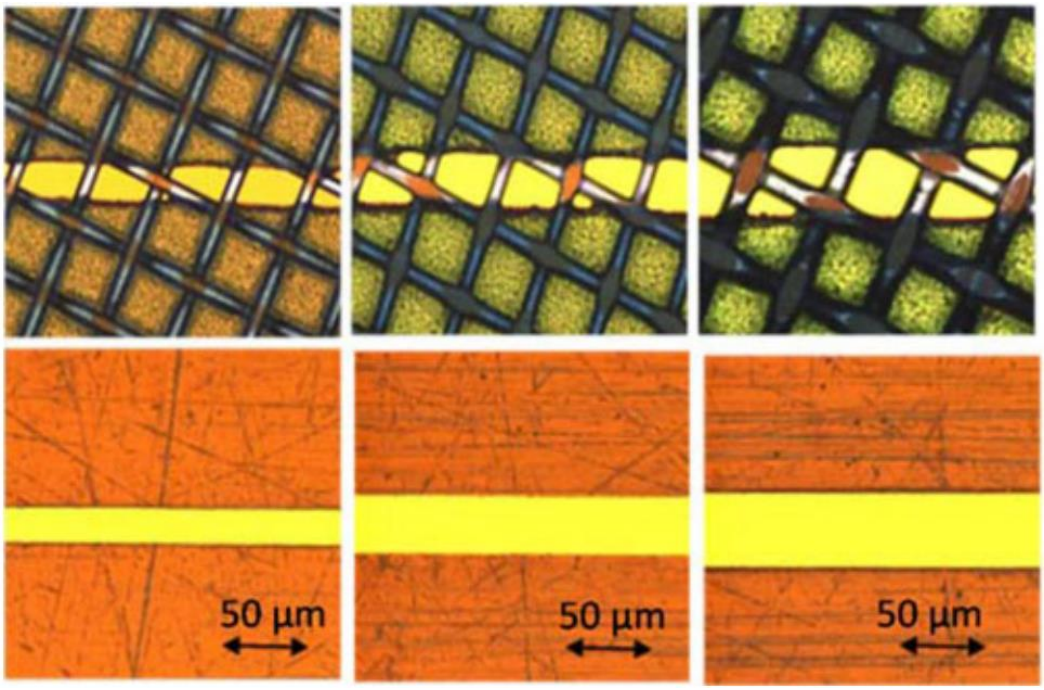

Figure 2.7: Optical microscopic images of the screen (top) and stencil (bottom) for different finger openings (30, 45, and 60 µm, respectively)

As seen in Table 2.4, stencil printing is only incrementally different from screen printing. It uses the same base equipment and pastes that are used for the screen printing, which makes it readily adoptable. It also has advantages over screen printing in terms of aspect ratio. Stencil printing is not adopted widely but it emerges as a very promising candidate for the dual printing process, which separates busbar and gridline printing into two different steps.

Table 2.4: The comparison between stencil and screen printing

	Stencil Printing	Screen Printing
Aspect Ratio (height/width)	~ 0.40	~ 0.25
Best Efficiency	19.9%	20.15%
System's Throughput	High	High
Ag Particle Size	Macro	Macro
Ease of Implementation	Medium	Easy
Finished Product	Yes	Yes

2.3.3 Screen Printing

Screen printing (SP) is a high throughput industrial method for making contacts to a solar cell. It is also cost effective compared to photolithography and buried-contact technologies. SP was reported by [36] and [37] as a viable option for metallization of solar cell because it provides fast metallization at comparatively low cost. SP is a process in which a metal-containing conductive paste is forced through the openings of a screen onto a wafer to form the contacts. By using SP technique to form the front and back contact of the solar cell, a reliable and fast process was established.

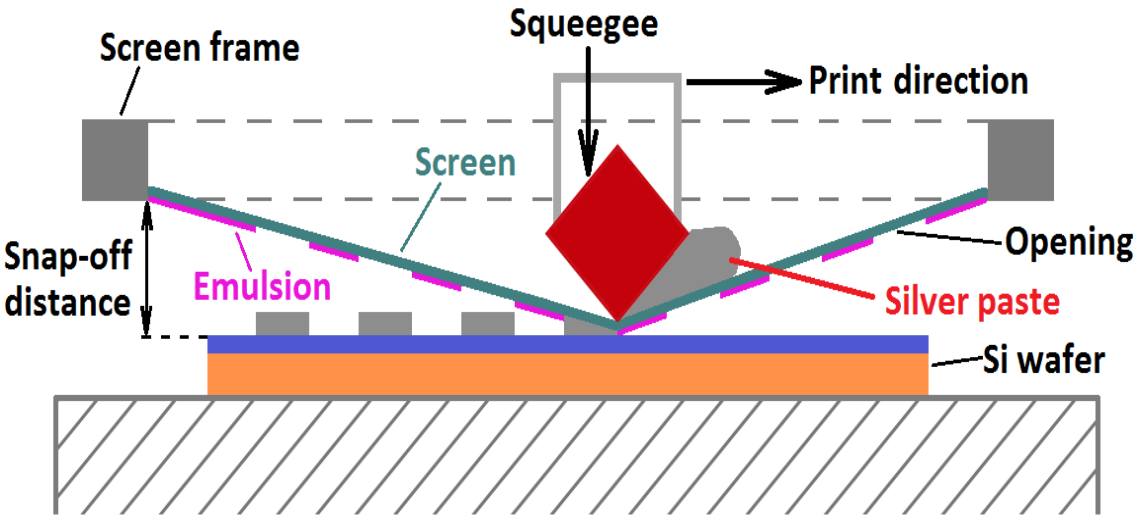

Figure 2.8: Screen printing setup illustration

Figure 2.8 shows the schematic diagram of screen printing. The process starts with the creation of a mask (emulsion) which is bonded to a metal screen (see Figure 2.9). The screen is placed in close contact with the solar cell, and a squeegee pushes metallic paste through the screen dispensing it onto the solar cell in the prescribed pattern. Using this basic method, gridlines width of 40-70 µm wide and an average height of ~15 µm can be obtained from a screen having an opening of 30-60µm wide.

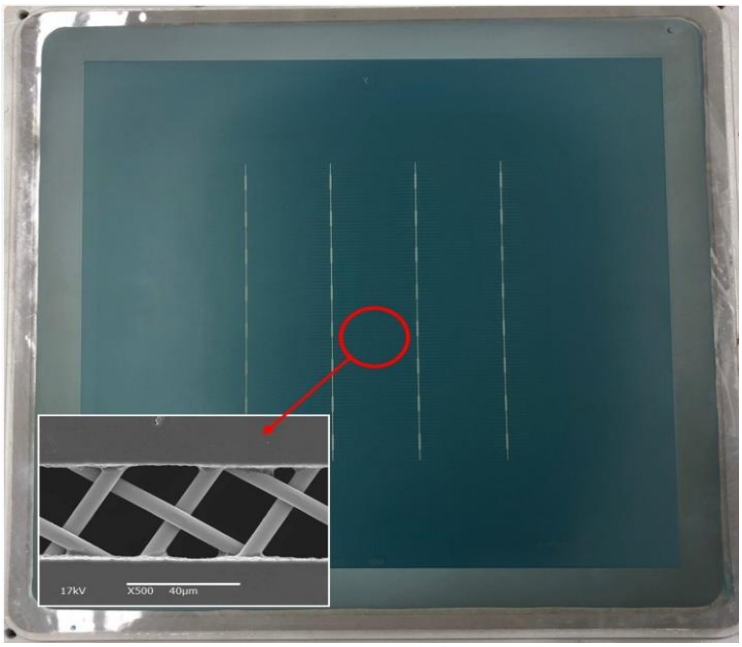

Figure 2.9: A practical screen for screen printing. The inset picture shows the meshes of the openings

Regardless of printing method, the goal of every concept is to have fine gridlines / busbars resulting in less shading area so that the I_{SC} is not affected. Gridline geometry may also impact the R_S and leads to low efficiency. Therefore, the metallization pattern is an important step to achieve desired gridlines on the solar cells. That is why, in the next chapter, designing and modelling the gridline patterns will be carried out to ensure having the most beneficial pattern.

CHAPTER 3 :
DESIGN AND MODELING OF METTALIZATION PATTERN ON THE FRONT SIDE OF SOLAR CELLS

The front shadowing loss, series resistance and silver paste consumption are functions of metal grid designs and metallization technology. In order to decrease the shadowing loss, the conventional screen-printed silicon solar cell front metal coverage has decreased remarkably from 8% to <4% through gridline width of <50 μm. Although, it should be noted that reduced shadowing loss can lead to increased series resistance because of higher contact and gridline resistances Therefore, printed gridlines require uniform gridline profile from busbar to busbar in conjunction with high aspect ratio.

Metallization cost plays a big role in the overall cost of the cell, and therefore, must be accounted for if a cost-effective solar cell is desired. Thus, the gridline design plays a great role in alleviating the series resistance constraint placed by narrow gridlines or aspect ratio. Chen et. al. [38] showed that for a given number of busbars, the gridline height would have negligible impact on the cell conversion efficiency after it had increased to a certain value. This suggests that the aspect ratio requirements of gridlines for a cost-effective solar cell can be relaxed with increased number of busbars.

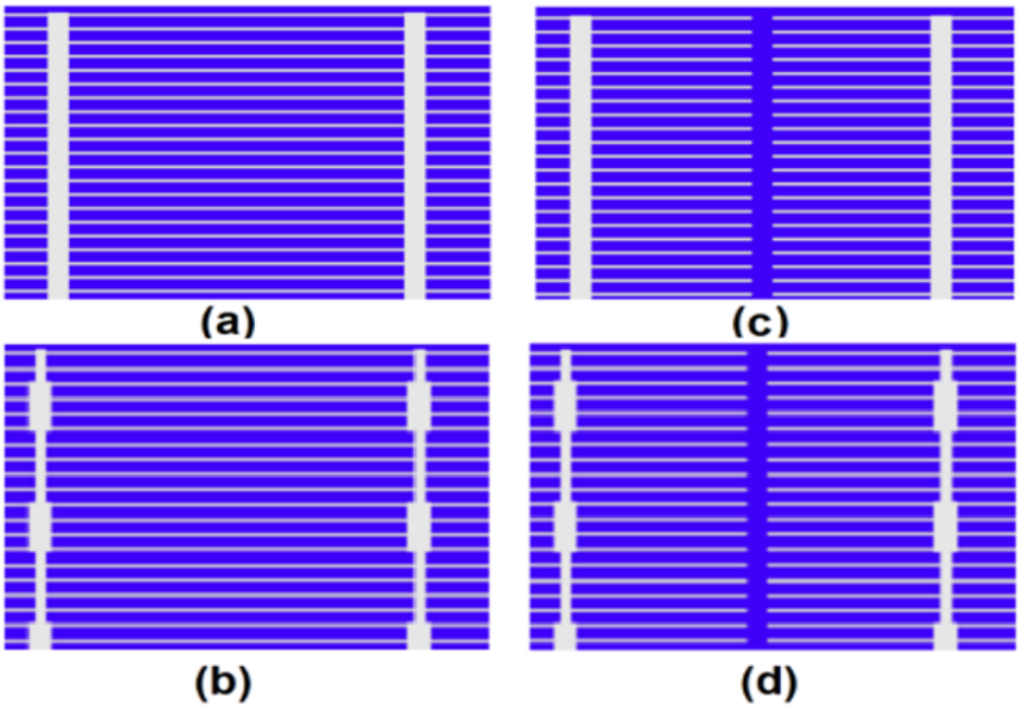

Figure: 3.1: Different design patterns for front metal contacts. (a) Even busbar + continuous gridlines (EB-CG); (b) uneven busbar + continuous gridline (UEB-CG); (c) even busbar + segmented gridline (EB-SG); (d) uneven busbar + segmented gridline (UEB-SG).

In this chapter, a comprehensive empirical grid model was first established and then used to investigate front grid metallization patterns. The open circuit voltage (V_{OC}), short circuit current (J_{SC}), fill factor (FF), and hence the efficiency of Al-BSF for each pattern was assessed. In particular, the impact of the segmented gridlines and multiple uneven busbars [39] on the electrical output parameters of the Al-BSF was assessed. The results were compared to Gridler 2D modeling [40] for accuracy. The gridline patterns assessed are shown in Figure: 3.1, which includes:

a. even busbar + continuous gridlines or EB-CG;
b. uneven busbar + continuous gridline or UEB-CG;
c. even busbar + segmented gridline or EB-SG; and

d. uneven busbar + segmented gridline or UEB-SG.

Each of these four patterns was investigated with the empirical model as well as in Griddler 2D model. The Ag cost-savings for each four patterns was assessed as well.

3.1 Arithmetical Description of Segmented Grid

For optimal grid pattern trends versus solar cell efficiency, different grid models [41-44] have been developed to assess the total series resistance and the corresponding resistive components such as emitter, gridline, busbar, and contact, etc. Because of non-uniformity and porosity of printed metal gridlines and busbars, and non-rectangular shape of gridline's cross section, as shown in Figure 3.2, the assumptions in those grid models disagree with the practically printed metal grid. This often results in inconsistencies between the calculated and measured total series resistance values. To overcome this discrepancy, direct measurements of busbar-to-busbar and the front busbar resistances were implemented by Meier et al. [45, 46]. Also, the Gaussian shaped gridline was employed by Jiang et al [47] to simulate the practical shape of the screen-printed gridline. However, the direct measurements of busbar-to-busbar and front busbar resistances are not feasible due to segmented grids. Therefore, the need to establish the grid model to assess the series resistance of segmented gridlines and the impact, as discussed below.

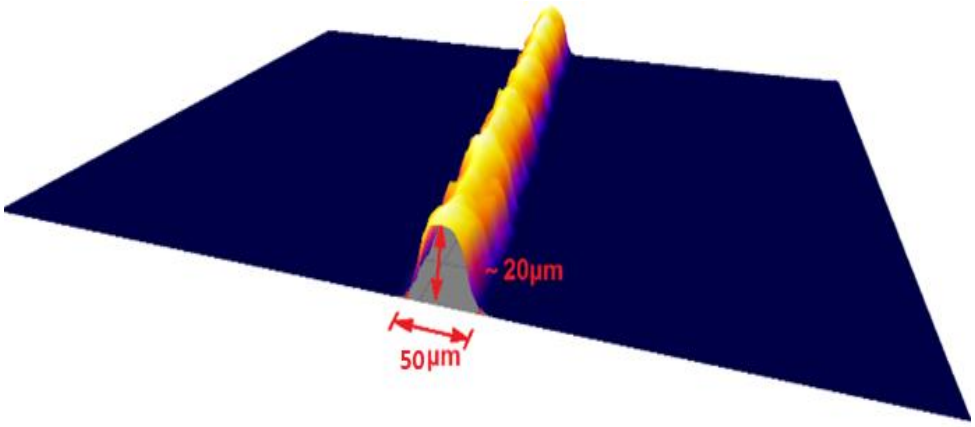

Figure 3.2: Practical profile of a screen printed gridline

Figure: 3.3 shows a unit cell used in the model calculation of the series resistance. The unit cell has $d+a+w'$ units long and $n(2b+w)$ units wide, where n is the number of gridlines assigned to each unit cell, $2b$ is the distance between the edges of the neighboring gridlines, $2d$ is the length of gridline segmentation, w is the width of gridline, $2w'$ is the width of busbar, and a is the length of gridline in the unit cell, as shown in Figure: 3.4. The entire solar cell is then composed of repeated unit cells across the full cell area.

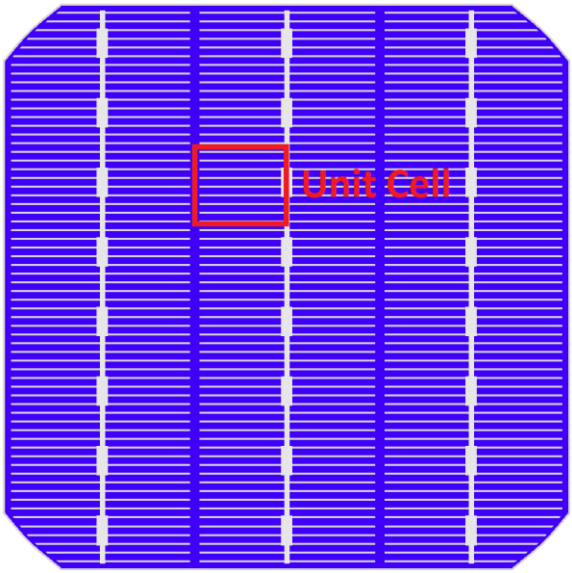

Figure: 3.3: Front grid design of 3-busbar solar cell with segmented gridlines and busbars

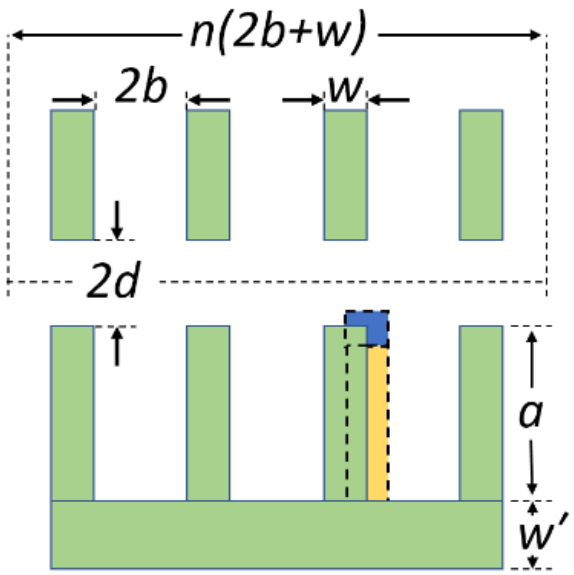

Figure: 3.4: Simple grid pattern for solar cells with segmentation of gridlines.
Active unit cell area is n·(2b+w)(d+a+w′)

The power loss due to series resistance is associated with current traveling through the emitter, the contact resistance, gridlines, busbars, and through the base

of the cell. From Meier et al. [43], for diffused emitter layer in the yellow region (Figure: 3.4), the power loss is given by;

$$P_{emitter1} = \frac{1}{3} J_L{}^2 \left(a - \frac{w}{2}\right) b^3 R_{sheet} \tag{3.1}$$

where J_L is the light-generated current density, R_{sheet} is the emitter sheet resistance, a-$w/2$ is the length of emitter in the yellow region (Figure: 3.4), and $2b$ is the spacing of gridline.

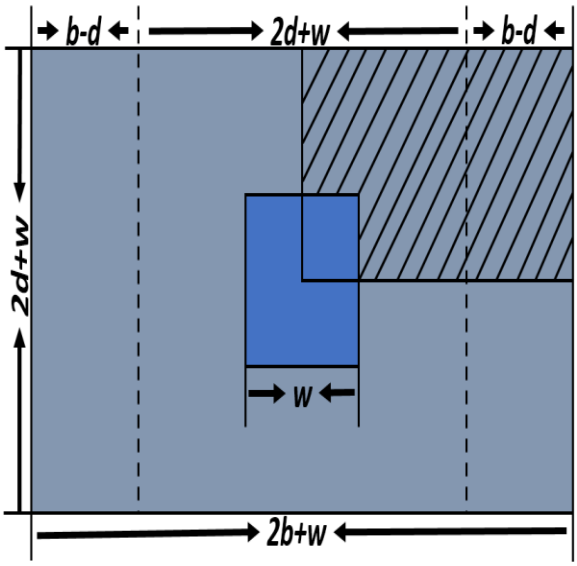

Figure: 3.5: A non-square subdivision element (hatch shading area) of the unit cell with three mirror symmetries (b ≥d)

The diffused emitter layer in the blue region (Figure: 3.4) is shown in the hatch shading area of Figure: 3.5. The combination of the hatch shading area with its three mirror symmetries, as demonstrated in Figure: 3.5, resembles the subdivision of a symmetry element of an EWT solar cell. According to Fallisch et al. [48], the power loss of the whole green region in Figure: 3.5 can be written as;

$$P_{emitter2} = \frac{{J_L}^2 R_{sheet}(2d+w)^4}{2\pi}\left(ln\left(\frac{2d+w}{w}\right) - \frac{3}{4} + \frac{w^2}{(2d+w)^2}\right.$$

$$\left. - \frac{w^4}{4(2d+w)^4}\right) \cdot \left(1 + f \cdot \frac{2b-2d}{2d+w}\right) \qquad (3.2)$$

$$+ \frac{2{J_L}^2 R_{sheet}(2d+w)(b-d)^3}{3}$$

where $f = 0.61+0.44 \cdot exp\{w/(2d+w)\}$. Note that the above expression for the power loss is obtained based on the assumption that $b \geq d$. For $b \leq d$, the subdivision element in Figure: 3.5 can be transformed into the counterpart shown in Figure: 3.6.

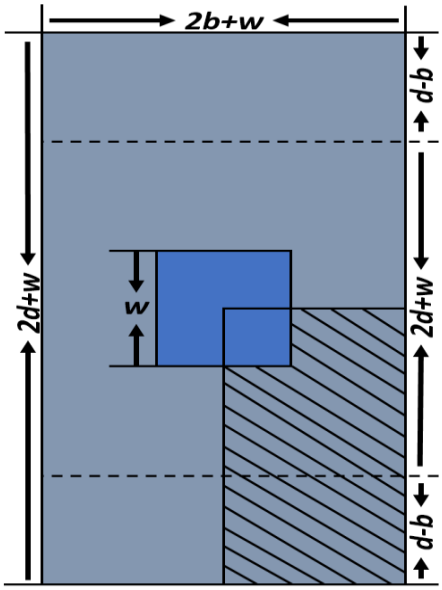

Figure: 3.6: A non-square subdivision element (hatch shading area) of the unit cell with three mirror symmetries (b ≤d)

Similarly, the power loss can be written as;

$$P'_{emitter2} = \frac{{J_L}^2 R_{sheet}(2b+w)^4}{2\pi}\left(ln\left(\frac{2b+w}{w}\right) - \frac{3}{4} + \frac{w^2}{(2b+w)^2}\right.$$

$$\left. - \frac{w^4}{4(2b+w)^4}\right) \cdot \left(1 + f' \cdot \frac{2d-2b}{2b+w}\right) \quad (3.3)$$

$$+ \frac{2{J_L}^2 R_{sheet}(2b+w)(d-b)^3}{3}$$

where f' =0.61+0.44·exp{w/(2d+w)}.

Therefore the total power loss associated with the emitter in the unit cell shown in Figure: 3.3 can be given as;

$$P_{emitter} = \begin{cases} 2n(P_{emitter1} + \frac{P_{emitter2}}{4}), & b \geq d \\ 2n(P_{emitter1} + \frac{P'_{emitter2}}{4}), & b \leq d \end{cases} \quad (3.4)$$

The power loss associated with the contact resistance is;

$$P_{contact} = n \cdot (I^2 R_c) \quad (3.5)$$

According to the theory of transmission line model, the contact resistance (R_c) is given by [38];

$$R_c = \frac{R_{sheet} L_T}{a} \cdot coth\left(\frac{w}{L_T}\right) \quad (3.6)$$

$$R_c = \frac{\rho_c}{a L_T} \cdot coth\left(\frac{w}{L_T}\right) \quad (3.7)$$

where the transfer length L_T is defined as;

$$L_T = \sqrt{\rho_c / R_{sheet}} \quad (3.8)$$

Note that two cases lead to simplifications of Eq.(). For $w \leq 0.5L_T$, $coth(w/L_T) \approx L_T/w$ and;

$$R_c \approx \frac{\rho_c}{aw} \tag{3.9}$$

For w ≥1.5L_T, coth(w/L_T) ≈ 1 and;

$$R_c \approx \frac{\sqrt{\rho_c R_{sheet}}}{a} \tag{3.10}$$

Suppose ρ_c =3 mΩ-cm², R_{sheet} = 80 Ω/sq, then we have L_T ≈60 μm. This means that to take advantage of the approximation in Eq. (3.10)(3.10), the width of gridline has to be greater than ~90 μm, which is contrary to the shrinking gridline width driven by silver cost-reduction and more advanced printing technologies such as inkjet printing [49, 50]. Therefore with;

$$I = J_L \left[2ab + 2d\left(b + \frac{w}{2}\right)\right] \tag{3.11}$$

the expression for contact resistance dissipated power yields;

$$P_{contact} = 4n{J_L}^2 \left[ab + d\left(b + \frac{w}{2}\right)\right]^2 \frac{R_{sheet}L_T}{a} \cdot coth\left(\frac{w}{L_T}\right) \tag{3.12}$$

Associated with current flow along the gridline, the power loss is;

$$P_{gridline} = n\int_0^a I^2(y)dR \tag{3.13}$$

where *I(y)* is the accumulated current in the gridline at location *y*. To simplify the calculation, we can assume that the photogenerated current at the segmented region goes to the gridline at location *y* = *a*, so we have;

$$I(y) = J_L d(2b + w) + 2\int_y^a J_L b dy = J_L[d(2b + w) + 2b(a - y)] \tag{3.14}$$

The resistance of *dR* as an element of the gridline is represented by;

$$dR = \frac{\rho_f}{A_f} dy' \tag{3.15}$$

where ρ_f is the resistivity of gridline material, and A_f is the cross-sectional area of the gridline. Since the cross section of the practical gridline is not ideally rectangular, a Gaussian curve is used to simulate the shape of gridline, as shown in Figure: 3.7.

The profile of a Gaussian shape gridline can be described as Eq.(3.16), with the peak of H_o and the standard deviation of σ;

$$f(x) = H_o \cdot e^{-\frac{x^2}{2\sigma^2}} \tag{3.16}$$

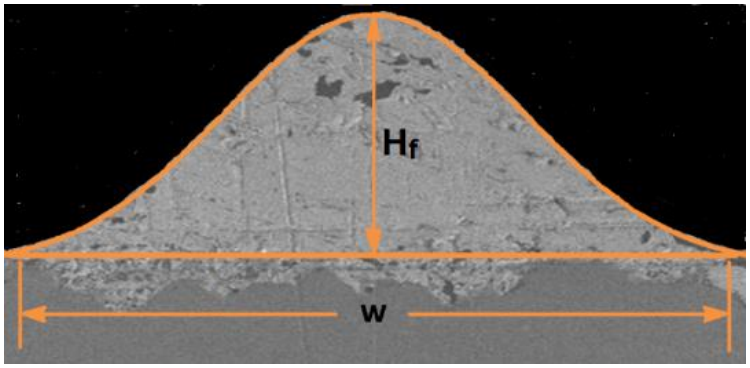

Figure: 3.7: Gaussian shape of screen-printed metal gridline having a width of w and height of Hf

To find gridline width (w) in the Gaussian profile, we assume that w equals $1/e^2$ width of the Gaussian profile, which is defined as the distance between the two points (x_1, $f(x_1)$), (x_2, $f(x_2)$) on the Gaussian curve where $f(x_1) = f(x_2) = H_o/e^2$. Then we have;

$$w = 2\sigma - (-2\sigma) = 4\sigma \tag{3.17}$$

And gridline height H_f can be calculated as;

$$H_f = H_o(1 - \frac{1}{e^2}) \tag{3.18}$$

The cross-sectional area of gridline can thus be obtained as;

$$\begin{aligned} A_f &= H_o \int_{-2\sigma}^{2\sigma} e^{-\frac{x^2}{2\sigma^2}} dx - 4\sigma \cdot (H_o - H_f) \\ &= \sqrt{2\pi}\sigma \cdot erf(\sqrt{2}) H_o - \frac{4\sigma H_o}{e^2} \end{aligned} \tag{3.19}$$

Combining Eqs. (3.17), (3.18), and (3.19) gives;

$$A_f = (\frac{\sqrt{2\pi}}{4} \cdot erf(\sqrt{2}) - \frac{1}{e^2}) \cdot wH_f \cdot \frac{e^2}{e^2 - 1} \tag{3.20}$$

Substitute Eqs.(3.14), (3.15)and (3.20) into(3.13), the power loss with gridlines in the unit cell yields;

$$\begin{aligned} P_{gridline} = &\frac{n{J_L}^2 \rho_f}{(\frac{\sqrt{2\pi}}{4} \cdot erf(\sqrt{2}) - \frac{1}{e^2}) \cdot wH_f \cdot \frac{e^2}{e^2 - 1}} \\ &\cdot \left[\frac{4}{3} b^2 a^3 + 2bda^2(2b + w) + d^2 a(2b + w)^2\right] \end{aligned} \tag{3.21}$$

In addition to emitter, contact and gridlines, the fourth contribution to power loss is the busbar. In the unit cell, the current enters the busbar from the individual gridlines in discrete quantities, then flows along the busbar and leaves the unit cell from a contact probe at the center of the busbar (Figure: 3.4). To simplify the calculation, the current will be treated as if it enters the busbar continuously. The power loss associated with the busbar is thus given as;

$$P_{busbar} = 2\int_0^{n(b+\frac{w}{2})} {I_b}^2 dR' \tag{3.22}$$

where I_b can be expressed as;

$$\begin{aligned} I_b &= \int_x^{n\left(b+\frac{w}{2}\right)} J_L\left(a + d - \frac{aw}{2b+w}\right)dx \\ &= J_L\left(a + d - \frac{aw}{2b+w}\right)\left[n\left(b+\frac{w}{2}\right) - x\right] \end{aligned} \tag{3.23}$$

The resistance dR' of an element of busbar is given by;

$$dR' = \frac{\rho_f}{A_b}dx' \tag{3.24}$$

Since the busbar width is much wider than that of gridline, it is technologically easier to print the busbar with a rectangular cross-sectional area, therefore;

$$A_b = 2w' \cdot H_b \tag{3.25}$$

where $2w'$ is the busbar width, and H_b the busbar height. Substitute Eqs. (3.23), (3.24), and (3.25) into(3.22), the expression for power loss associated with busbar can be deduced as;

$$P_{busbar} = \frac{\rho_f {J_L}^2 n^3}{3w'H_B}\left(a + d - \frac{aw}{2b+w}\right)^2 (b + w/2)^3 \tag{3.26}$$

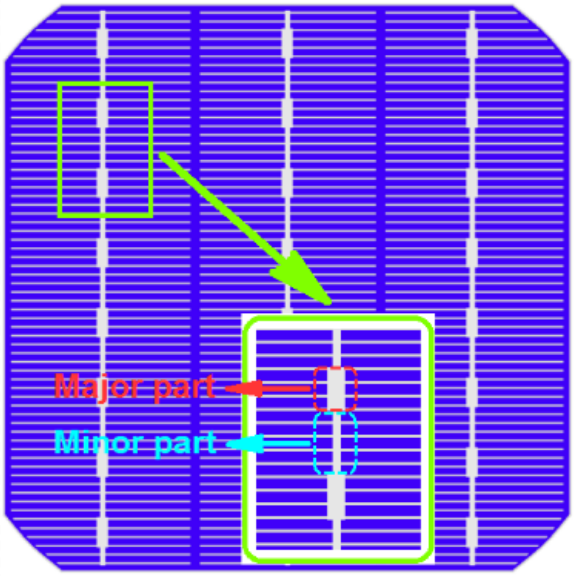

Figure: 3.8: Solar cell designed with uneven busbars with the major part of busbar having regular width, and the minor part having shrunk width.

For solar cells designed with uneven busbars, Figure: 3.8, we can similarly calculate the power loss with busbars by combining the losses from both the major and the minor parts. Assume the ratio of the length of major part to the total busbar length is s, the width of the major part is $2w_1$, and the minor part is $2w_2$, then we have;

$$P_{minor} = \frac{\rho_f {J_L}^2 n^3}{3w_2 H_B}\left(a + d - \frac{aw}{2b + w}\right)^2 \left(b + \frac{w}{2}\right)^3 (1 - s)^3 \tag{3.27}$$

$$P_{major} = \frac{\rho_f {J_L}^2 n^3}{3w_1 H_B}\left(a + d - \frac{aw}{2b + w}\right)^2 \left(b + \frac{w}{2}\right)^3 [1 + (s - 1)^3] \tag{3.28}$$

Therefore the total power loss associated with the busbar is;

$$P_{busbar}{}' = \frac{\rho_f {J_L}^2 n^3}{3H_B}\left(a + d - \frac{aw}{2b+w}\right)^2 \left(b + \frac{w}{2}\right)^3 \left[\frac{1+(s-1)^3}{w_1} + \frac{(1-s)^3}{w_2}\right] \tag{3.29}$$

Current flow through the base of the cell results in a power loss given simply by;

$$P_{base} = I^2 R_{base} \tag{3.30}$$

with;

$$I = 2nJ_L\left[ab + d\left(b + \frac{w}{2}\right)\right] \tag{3.31}$$

$$R_{base} = \frac{\rho_w t_w}{A_{cell}} = \frac{\rho_w t_w}{n(2b+w)(d+a+w')} \tag{3.32}$$

where ρ_w is the base resistivity, t_w is the thickness of the bulk, and A_{cell} the area of the unit cell. Thus the power loss with the base can be rewritten as;

$$P_{base} = 4n{J_L}^2\left[ab + d\left(b + \frac{w}{2}\right)\right]^2 \cdot \frac{\rho_w t_w}{(2b+w)(d+a+w')} \tag{3.33}$$

Finally, the power loss resulting from front shadowing of the cell by both gridlines and busbar is;

$$P_{shadow} = P_L \eta n[aw + w'(2b+w)] \tag{3.34}$$

where P_L is the power density of the incident light and η is the energy conversion efficiency of the cell.

For the power loss with the back metallization, because the entire back side of the silicon wafer is contacted by full aluminum and silver strips, the power loss

associated with the back contact and back metal is relatively smaller than other losses and can be ignored in the calculation.

To better assess the total power loss of the cell, the corresponding losses with different components of series resistance from Equations (3.4), (3.12), (3.21), (3.26), (3.29), (3.33), and (3.34) are then normalized to unit cell area of n(2b+w)(d+a+w′), and the summary of expressions are listed in Table 3.1.

Table 3.1: Summary Of Power Loss Expressions

Power Loss Factors	Normalized expression
Emitter	$p_{emitter} = P_{emitter} / \{ n(2b+w)(d+a+w')\}$
Front Contact	$p_{contact} = P_{contact} / \{ n(2b+w)(d+a+w')\}$
Gridline	$p_{gridline} = P_{gridline} / \{ n(2b+w)(d+a+w')\}$
Busbar (even)	$p_{busbar} = P_{busbar} / \{ n(2b+w)(d+a+w')\}$
Busbar (uneven)	$p_{busbar}' = P_{busbar} / \{ n(2b+w)(d+a+w')\}$
Base	$p_{base} = P_{base} / \{ n(2b+w)(d+a+w')\}$
Shadowing	$p_{shadow} = P_{shadow} / \{ n(2b+w)(d+a+w')\}$

*n(2b+w)(d+a+w′) is the area of unit cell defined in Fig. 2.1.

The overall power loss normalized to unit area is the sum of power loss from the emitter, contact, gridlines, busbar, base, plus the shadowing loss;

$$p_{R_s} = p_{emitter} + p_{contact} + p_{gridline} + p_{busbar} + p_{base} \quad (3.35)$$

$$p_{total} = p_{R_s} + p_{shadow} \tag{3.36}$$

The cell series resistance (Ω-cm²), normalized to unit area is;

$$r_s = p_{R_s}/J_L^2 \tag{3.37}$$

3.2 Modeling Parameters

Table 3.2 shows the input parameters that is taken into account while modeling empirically and using Griddler 2D computer program. After establishing the segmented grid model, the experimentally measured electrical parameters of an industrial size (156x156 mm²) three-busbar monocrystalline Al-BSF silicon solar cell was modeled. Some of the output cell parameters are listed in Table 3.2. Note that the gridline and busbar segmentations were set to zero to simulate continuous metal gridline as the reference cell. Taking the modeled cell as the baseline, the grid segmentations were varied to evaluate the effect on solar cell performance.

Table 3.2: Device And Material Parameters For Reference Cell And Modeled Cell Without Segmentations In Metal Grids

Parameters	Reference-Cell	Modeled Cell
Wafer thickness (μm)	180	180
Emitter sheet resistance (Ω/sq)	100	100
Gridline width (μm)	~60	40-50-60
Gridline height (μm)	~15	15
Busbar widths (mm)	1.2	1.2-0.9-0.72
Busbar height (μm)	~15	15
Base resistivity (Ω-cm)	1.5	1.5
Contact resistivity ($m\Omega\text{-}cm^2$)	3.5	3.5
Gridline resistivity (Ω-cm)	5.0E-06	5.0E-06
V_{OC} (mV)	640.4	640.3
J_{SC} (mA/cm^2)	37.81	37.77
Fill factor	0.8030	0.8033
Efficiency (%)	19.44	19.43

3.3 Results and Discussion

3.3.1 Impact of gridline segmentation width (mm) on solar cell efficiency and series resistance

The relationship between solar cell efficiency and gridline segmentation width is shown in Figure: 3.9. The efficiency increases slightly as the gridline segmentation width until after ~ 2 mm, it starts decreasing. A reduction in gridline shadowing as segmentation width increases gives rise to higher J_{SC}. However, because of increased series resistance, the *FF* decreases, and hence the drop in efficiency for >2 mm width. This trend is true, irrespective of the number of busbars.

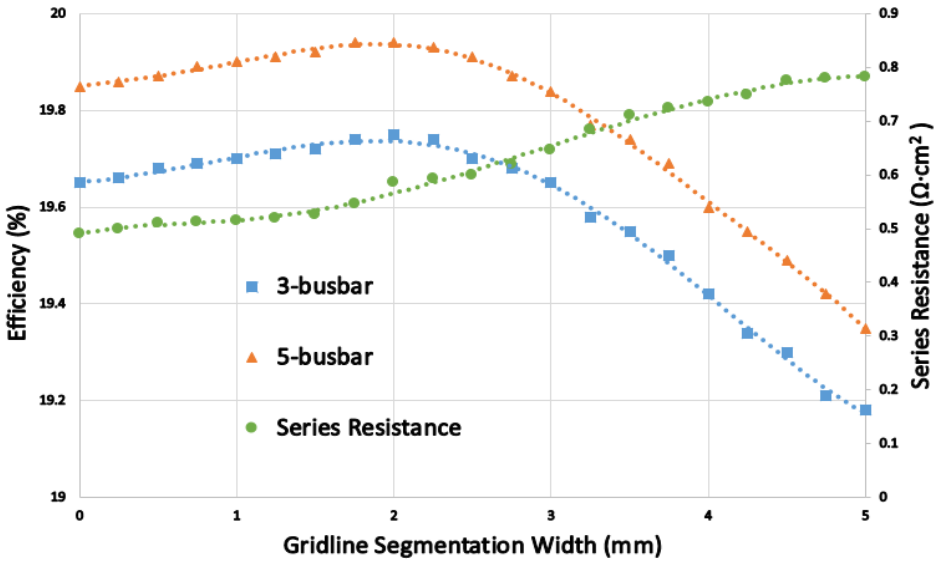

Figure: 3.9: Modeled 3-busbar and 5-busbar solar cell efficiency as a function of gridline segmentation width

3.3.2 Impact of uneven busbars on solar cell efficiency

To further reduce the shadowing effect of the continuous bus bars, the uneven busbars, as shown in Figure: 3.8, were assessed. The 3-, and 5-busbar solar

cells were modeled in conjunction with the segmented gridlines. The variation of front shadowing, J_{SC}, FF and efficiency with the ratio of major to total busbar (s), and minor busbar width ($2w_2$) were investigated.

Figure: 3.10 shows the efficiency as a function of s for continuous and segmented gridlines. Note that s=1 represents uniform busbar width of 1.2 mm and 0.72 mm (major busbar width) for 3- and 5-busbar cells, respectively. While s=0 represents uniform busbar width of 0.6 mm and 0.36 mm (minor busbar width) for 3- and 5- busbar counterparts, respectively.

As s decreases from 1 to 0, the average busbar width shrinks due to reduction in total major busbar length. Because the busbar resistance does not carry much weight in series resistance (R_S), the decrease in average busbar width only has very small impact in total R_S. As s varies from 0 to 1, for instance, the modeled busbar resistance only decreases from 0.044 $\Omega \cdot cm^2$ to 0.012 $\Omega \cdot cm^2$ for both 3- and 5-busbar solar cells.

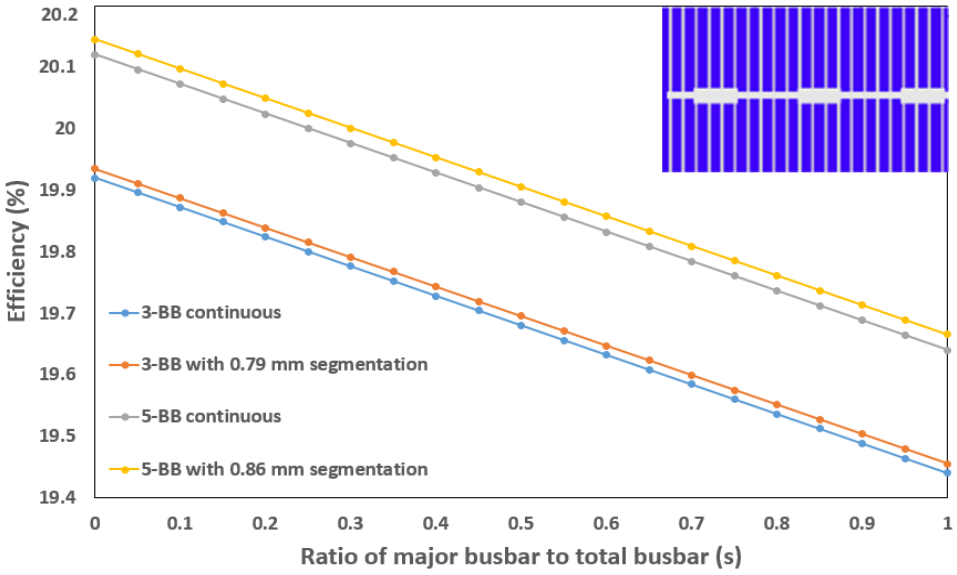

Figure: 3.10: Modeled 3- and 5-busbar solar cell efficiencies as a function of s for continuous gridlines and gridlines with optimal segmentation (minor busbar width = 0.6 mm)

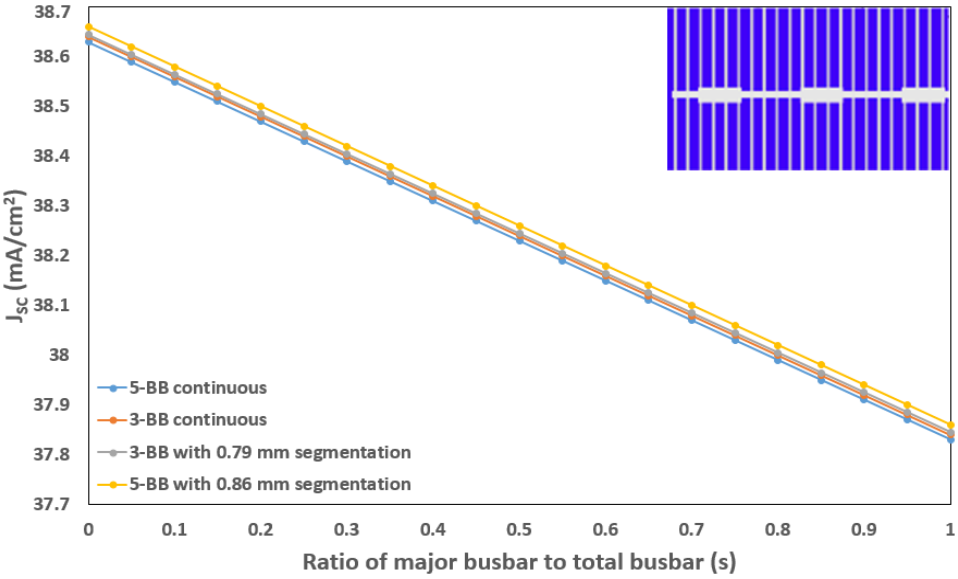

Figure: 3.11: Modeled 3- and 5-busbar solar cell short-circuit currents plotted as a function of s for continuous gridlines and gridlines with optimal segmentation (minor busbar width = 0.6 mm)

However, the improvement in J_{SC} is pronounced for all solar cell designs as s decreases from 1 to 0 as shown in Figure: 3.11 A ~0.86 J_{SC} mA/cm² J_{SC} enhancement

is realized due to decrease shadowing as the average busbar width shrinks. More so, the 5-busbar design has more potential than the 3-busbar counterpart to obtaining > 20% efficiency. This can be attributed to relatively shorter effective gridline length accompanied by reduced series resistance.

To further evaluate the enhancement in J_{SC} with shrunk average busbar width, the 3-busbar solar cell was taken as an example to investigate the change of front metal shadowing with *s*, as shown in Figure: 3.12. It is apparent that the variation in front shading is dominated by the change in busbar shading as *s* decreases from 1 to 0. It is worth mentioning that the reduction in metal shading can be as high as $2.13\%_{absolute}$ when the average busbar width decreases from 1.5 mm to 0.6 mm. This explains the noticeable improvement in J_{SC}, and hence efficiency.

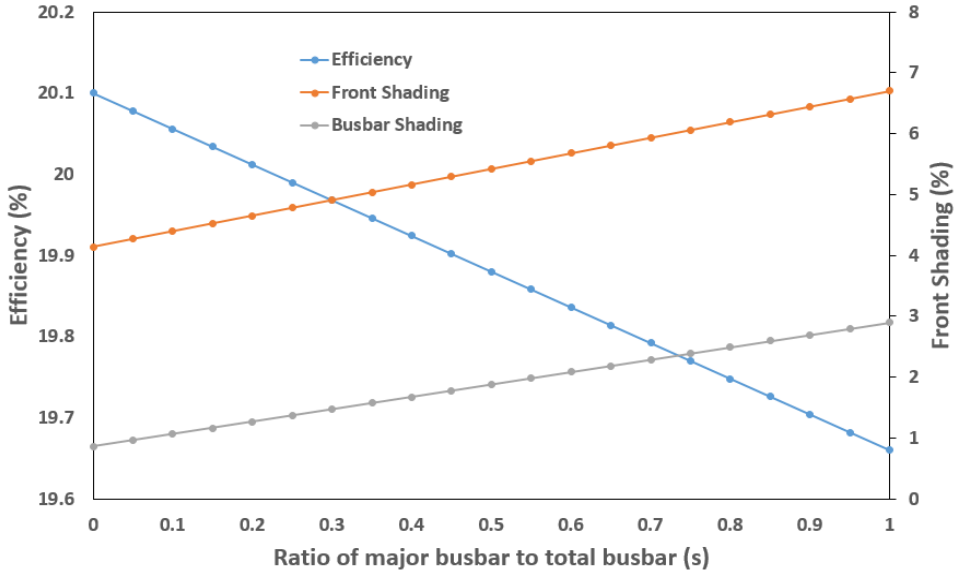

Figure: 3.12: Modeled 3-busbar solar cell efficiencies and front shading plotted as a function of s for continuous gridlines (minor busbar width = 0.6 mm)

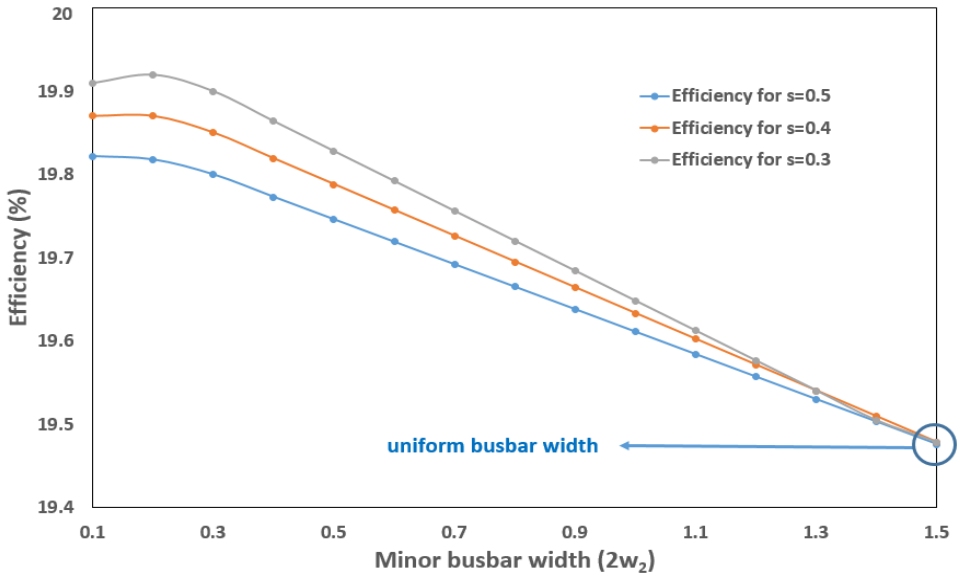

Figure 3.13: Modeled 3-busbar solar cell efficiencies plotted as a function of minor busbar width (2w2) for continuous gridlines with s = 0.3, 0.4 and 0.5

To determine the optimal minor busbar width, practical values for *s* were employed to assess the variation in efficiency as minor busbar width ($2w_2$) changes, Figure 3.13. Note that the minor busbar width of 1.5 mm represents uniform busbar width along total busbar length, and efficiency stays the same irrespective of *s* value. As minor busbar width decreases from 1.5 mm to 0.1 mm, the efficiency keeps increasing for *s* equals 0.4 and 0.5. While for *s* equal to 0.3, the efficiency reaches the peak. Also, for smaller *s* values, the impact of minor busbar width on conversion efficiency gets stronger as it decreases. This indicates that the design of uneven busbar needs to be optimized at cell level before connected in module.

To better interpret the enhancement in efficiency brought by different values of *s* as well as the minor busbar width, the front metal shadowing and J_{SC} were also investigated correspondingly, as illustrated in Figure 3.14.

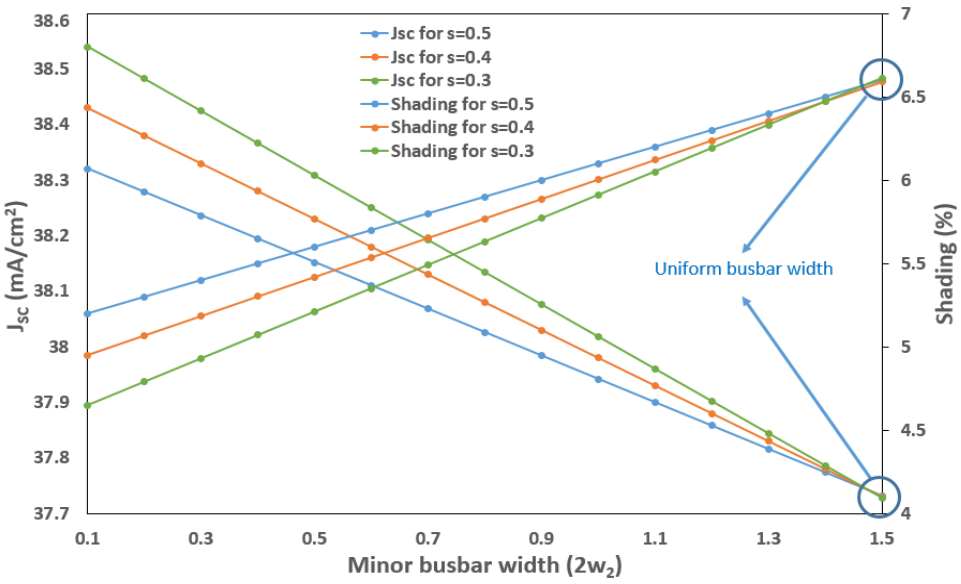

Figure 3.14: Modeled 3-busbar solar cell short-circuit current and front shading plotted as a function of minor busbar width (2w2) for continuous gridlines with s = 0.3, 0.4 and 0.5

It is shown that for any given *s*, the front shading increases as minor busbar width increases, which explains the decreasing J_{SC} accordingly. When minor busbar width reaches 1.5 mm, the front metal shadowing and J_{SC} associated with different *s* converge at the same point, respectively. Thus, the busbar width along the busbar gets uniform such that the cell I-V data becomes independent of *s*. However, as the minor busbar width falls below 1.5 mm, *s* of 0.3 provides the lowest front shading and the highest J_{SC}, which corresponds to the highest efficiency.

3.3.3 Validation of Empirical Model Using 2-D Griddler 2.5

To validate the empirical model, the Griddler 2.5 [40], a 2-D computer modelling program was employed. The input to Griddler model, is the screen design imported directly from AutoCAD as a .dfx file. Once the design is imported into, then the procedure of generating the front and rear meshes follow and then the

modeling. Table 3.3 is an example of the electrical output parameters for a 3BB cell with different patterns. The sheet resistance of 100 ohm/sq, J_{01} of 100fA/cm² and 1000fA/cm², respectively, for the passivated and metal contact regions, and J_{02} of 3nA/cm² were used. For the 3-, 4- and 5-BB even busbar and continuous gridline (EB-CG) design, gridline and busbar openings of 60 μm and 1.2 mm, respectively, were used. Whereas, for the 5-BB uneven busbar and continuous gridline (UEB-CG) design, 0.72 mm and 0.36 mm, respectively, major and minor busbars and tapered gridline of 60-50-40 μm openings were used. But for the 4-BB UEB-CG, 0.9 mm and 0.45 mm, respectively, were the openings for the major and minor BB, while maintaining tapered gridline opening of 60-50-40 μm. And the 3-BB UEB-CG had 1.2 mm and 0.6 mm, respectively, major and minor BB opening but same tapered gridline opening as other designs.

Table 3.3: Modeled 3-Busbar Cell I-V Data With Different Segmentations

Screen design	V_{oc} (mV)	J_{sc} (mA/cm^2)	FF	Efficiency (%)
EB-CG	644.35	37.37	81.24	19.54
UEB-CG	645.65	37.93	80.95	19.80
UEB-1mm SG	645.70	37.94	80.95	19.81
UEB-2mm SG	645.95	37.95	80.87	19.80
UEB-3mm SG	646.01	37.97	80.63	19.74
UEB-4mm SG	646.02	38.00	80.24	19.65
UEB-5mm SG	646.06	38.02	79.18	19.40

Figure 3.15 shows the modeling results, which depicts the empirical counterparts shown in Figure: 3.9. Griddler simulations suggests, just as the empirical model, that the 5-BB design is superior to 3-BB counterpart. It should be noted that there is an average 0.35% efficiency increase from the regular design to uneven busbar even without gridline segmentation.

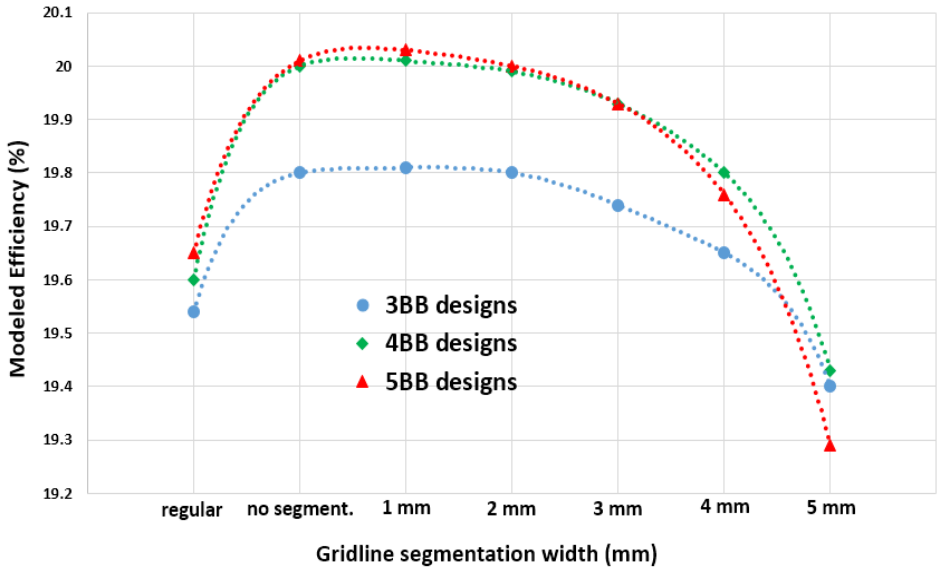

Figure 3.15: Griddler model for efficiency with different screen designs. Regular refers to no segmentation and no uneven busbars, no segmentation refers to straight gridlines with uneven busbars, 1-5mm is the gridline segmentation with uneven busbars

3.4 Conclusion

In this chapter, gridline segmentation combined with an uneven busbar concept was investigated. This a low-cost pathway to achieving >20% and >22% energy conversion efficiency for the industrial Al-BSF and PERC solar cells respectively without any additional cost. This was achieved by first, establishing an empirical comprehensive grid model, which results were compared to the established 2-D Griddler. The results were identical, which confirmed the validity of the established empirical grid model. Thus, a combination of UEB and SG, does not only increase the efficiency but decreases the Ag usage and hence cost effective and high efficiency solar cells.

CHAPTER 4 :
THE IMPACT OF Ag PARTICLE SIZE ON SCREEN PRINTED SILICON SOLAR CELLS

Metallization of commercial solar cells require the use of metal paste having appropriate viscosity and good thixotropy. The metal pastes commonly used are aluminum (Al) for back contact and silver (Ag) paste for the front grid. The content of these pastes include: 70-80% (weight) silver powder, 15-20% organics and 1-5% glass frit (PbO, ZnO, Al_2O_3, SiO_2, and TiO_2) (see Figure 4.1). Silver powder is offered as the best option for front metallization paste because of its excellent conductivity and solder-ability. Its relatively low diffusion coefficient in silicon guarantees good contact with silicon substrate and longevity of the solar cell. The organics controls the rheology of the paste, which is responsible for the quick recovery of the elasticity of the paste during printing to produce continuous gridlines. The glass frit is responsible for etching of the ARC layer as well as providing the medium for dissolution of Ag particle and silicon. It also promotes the formation of contact between Ag-bulk and Si, and the adhesion of the gridline to silicon.

Sintering of the front printed gridline is critical to the gridline resistance, contact resistance and gridline adhesion. The goal is to achieve excellent adhesion to the substrate and obtain the lowest possible gridline and contact resistances. Sintering influences the effectiveness of vanishing porosity in fired gridlines. The contact resistance is affected by the glass frit and contact firing conditions [50]. Therefore the role of Ag paste and its content on contact formation needs to be well understood. This chapter investigates

i. the impact of organics, which dictates the paste rheology, on the performance of solar cells,

ii. effect of Ag nanoparticles on gridline sintering as it impacts the total series resistance of the finished solar cell and

iii. the impact of the belt speed on the fill factor of the screen-printed solar cells.

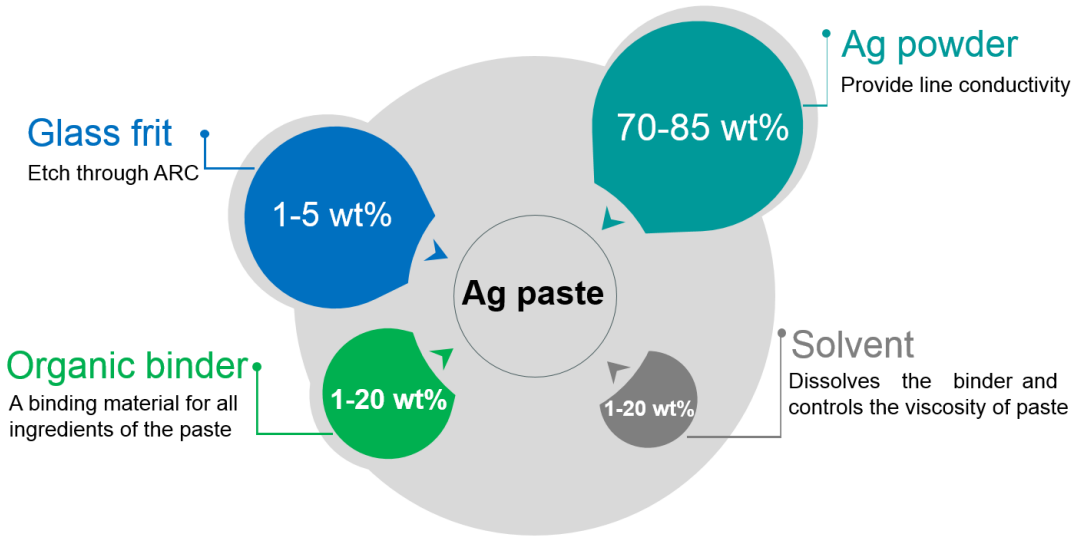

Figure 4.1: The composition of a typical metallic Ag paste used silicon solar cell front contact formation

4.1 Impact of paste Rheology in Ag-Paste for solar cell application

Ag paste for solar cell application is a suspension of micro (or nano)-sized silver particles and a glass frit in a solvent to which some binders are added [51]. The Ag particle morphology is either flakes of ~5μm size, or spherical of 1nm-10μm size. It also comprises a small amount of organic additives that act as a vehicle for the powders and evaporate during the firing process. The glass frit in the paste is a

mixture of metal oxides such as PbO, ZnO, Al_2O_3, SiO_2, and TiO_2 etc., which improves mechanical adhesion of the contacts to silicon. The importance of rheology characteristics of the paste relies on the demand of having biggest cross-sectional area of the contacts. However, the contacts must be as narrow as possible to avoid shading loss on the front surface which implies that the narrow contacts should be as high as possible to keep cross-sectional area bigger. Therefore, solar cell applications require thick film Ag pastes having appropriate viscosity and good thixotropy during printing to avoid gridline breakage.

Thixotropy stands for a time-dependent change in viscosity due to structural changes in the medium (such as speed and movement). Thixotropy of an Ag paste may vary depending on the method used to print on a solar cell. The continuity of Ag paste in the gridlines and the paste relaxation (slumping effect) in the first couple of milliseconds after the printing process is controlled by the thixotropy – ability to return to its viscous state after stroking with squeegee. Two effects can result from poor thixotropy including line breakage and slumping, which could result in high series resistance. Minimizing the slumping of the paste can lead to high aspect ratio of the gridlines. Thus, fine and more gridlines can printed without increasing the metal coverage on the front surface and hence improve the FF.

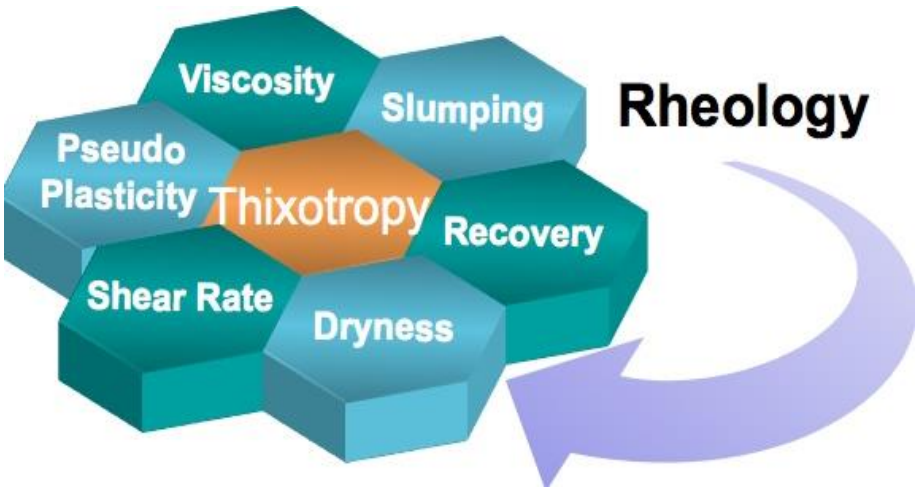

Figure 4.2: Correlation of the Ag paste rheology

In order to understand the impact of organics on the paste rheology, two front Ag pastes with different organics were tested compared to the baseline front paste. Table 4.1, Table 4.2, and Table 4.3 show the cell electrical parameters with the baseline paste, baseline plus organic A, and baseline plus organic B, respectively. All cells are commercial 239cm^2 area with 65ohm/sq emitter. The width of fingers after firing is 73µm, 65µm and 64µm for baseline, baseline plus organics A and baseline plus organics B respectively. The LIV measurements shows the average efficiency of 18.6%, 18.8% and 18.7% for baseline, organics A and organics B respectively. The drop in metal coverage from ~6.91% to ~6.12% with less slumping effect is obtained with the existence of organics added to baseline Ag paste. Therefore the average efficiency increases to 0.2% without changing anything but some organics in the paste.

Table 4.1: Electrical Outputs Of Silicon Solar Cells With The Baseline Paste

# of Cells	V_{OC} (V)	J_{SC} (mA)	FF (%)	Eff (%)
#1	0.632	36.9	79.8	18.6
#2	0.632	36.9	79.5	18.5
#3	0.632	37.0	79.3	18.6
#4	0.633	37.1	79.5	18.6
Average	0.632	37.0	79.5	18.6

Table 4.2: Electrical Outputs Of Silicon Solar Cells With The Baseline Paste + Organic A

# of Cells	V_{OC} (V)	J_{SC} (mA)	FF(%)	Eff (%)
#5	0.635	37.3	79.4	18.8
#6	0.634	37.3	79.6	18.8
#7	0.634	37.3	79.6	18.8
#8	0.633	37.1	79.4	18.7
Average	0.634	37.3	79.5	18.8

Table 4.3: Electrical Outputs Of Silicon Solar Cells With The Baseline Paste + Organic B

# of Cells	V_{OC} (V)	J_{SC} (mA)	FF (%)	Eff (%)
#9	0.633	37.4	79.8	18.6
#10	0.633	37.4	79.5	18.7
#11	0.633	37.3	79.3	18.7
#12	0.633	37.2	79.5	18.7
Average	0.633	37.3	79.5	18.7

4.2 Ag Particle Sintering Mechanisms

The Ag particle morphology in the metallization paste is either flakes of ~5μm size or spherical of 1nm-10μm size of which is most likely used in the commercial paste. Sintering (or densification) is a reduction of porosity among those particles in the paste by applying thermal energy when they come into contact [52]. There are three types of sintering, solid state, transient liquid phase and liquid phase sintering (LPS). Of these three, liquid phase sintering is applicable to the front Ag silver paste sintering because of the presence of the glass frit. During firing, the molten glass frit remarkably accelerates the sintering rate due to rearrangement and coarsening processes.

The three requirements for active sintering are (i) wetting angle, (ii) contact angle and (iii) neck growth. If there is a good wetting between liquid (glass frit) and

solid phases (Ag particles), solid grains can rearrange themselves under the action of surface tension forces, producing more stable packing. During the LPS, Ag particles start growing neck among each other as soon as contacting points are formed. The particles get reshaped by material transfer driven by the difference in free surface energy given in Eq. 4.1 and the pressure difference across the curved surface. The stress for a spherical shaped Ag particle with a radius of r (Eq. 4.2) causes flow of the material in a direction that minimizes the surface curvature, which contributes to lower the porosity in the gridline. The porosity in gridlines on silicon solar cells that causes a high gridline resistance after firing process is directly related to shrinkage volume (ΔV) resulted from densification depending on the radius of Ag particle (r), temperature (T) and time (t). From Eq. 4.3, ΔV decreases with increasing time and increases with smaller Ag particles size and higher temperatures which is relevant to the Tolmon's thermodynamic model that suggests the surface energy of nano particles is expected to decrease with decreasing particle size [53, 54].

$$\gamma = \gamma_{sl} + \gamma_l cos\theta \tag{4.1}$$

$$\sigma = {}^{2\gamma}/_{r} \tag{4.2}$$

$$\frac{\Delta V}{V_0} \propto r^{-6/5} \cdot t^{2/5} \cdot \left({}^{D_v}/_{T}\right)^{-2/5} \tag{4.3}$$

There are different types of sintering models reported, such as viscous flow model [55], the neck growth model [56, 57] and the K-F type model [58, 59]. Of these three models, the conventional neck growth model will be adopted in this section,

which tracks the detailed neck growth and identifies diffusion mechanisms. In order to visualize the tracking, Figure 4.3a shows geometrical configuration of sintering particles as reported by Johnson [57]. Ag particles is represented by a sphere with a radius a. ρ is the radius of the neck surface, α is a measure of the grain boundary groove angle, c is the distance of the center of the particle to the symmetry plane, δ is the extent of the overlapping of the two spheres.

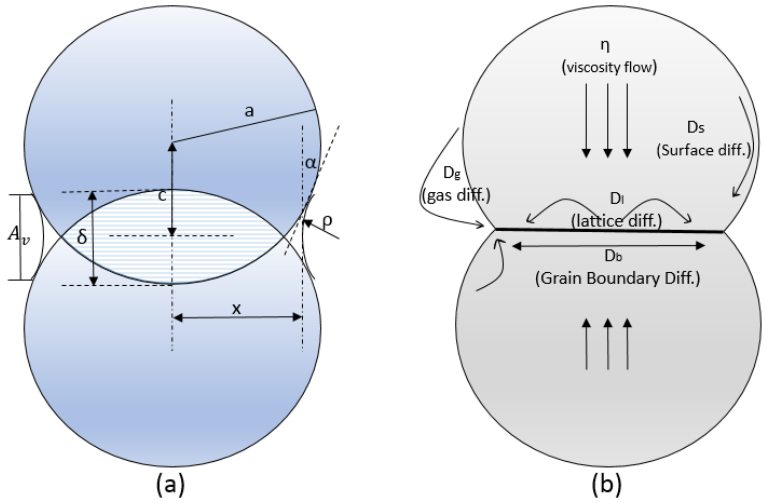

Figure 4.3: (a) Sintering geometry parameters for two spherical Ag

with additionally defined parameters of, $y=a-c/a$, $X=x/a$, $R=\rho/a$ and $\theta=sin^{-1}(a-ya+\rho sin\alpha/a+\rho)$, equations for geometric parameters as follows [57];

$$\rho = \frac{a(y^2 - 2y + X^2)}{2(1-(1-y)sin\alpha - Xcos\alpha)} \tag{4.4}$$

$$A_v = 4\pi\rho\{(\theta-\alpha)(a+\rho)cos\theta - \rho(sin\theta - sin\alpha)\} \tag{4.5}$$

$$X = (1+R)cos\theta - Rcos\alpha \tag{4.6}$$

The total volume of the Ag which moves to the neck with different mechanism between two spherical Ag particles, such as lattice diffusion, surface diffusion, grain boundary diffusion and viscous flow shown in Figure 4.3b, defined as V_T is sum of overlap volume V_B (shown as lighter area in Figure 4.3a) and the volume diffusing from Ag particle surface V_S.

$$V_T = V_B + V_S \tag{4.7}$$

The diffusion mechanisms (see Figure 4.3b) when sintering occurs need to be identified so that V_B and V_S can be accurately evaluated. Zhang, W. [60] reported that sintering of nano-sized particles is carried out only by grain-boundary and surface diffusions due to their high surface energy. If J_{GBD} represents grain-boundary diffusion flux and J_{SD} surface diffusion flux;

$$\frac{dV_s}{dt} = \Omega J_{SD} \tag{4.8}$$

where Ω is molar volume, the fluxes can be expressed by concentrations gradient. Johnson [57] also expressed these fluxes as a function of stress gradients and diffusion coefficients;

$$J_{GBD} = \frac{8\pi\gamma b D_b (x + \rho cos\alpha)}{kTx\rho} \tag{4.9}$$

$$J_{SD} = \frac{2\pi\gamma\Omega^{1/3} D_s (X + 2XR - Rcos\alpha)}{akTR^2} \tag{4.10}$$

where D_B and D_S are the diffusion coefficients, b is the thickness of the region of enhanced diffusion at the grain boundary, k is the Boltzman constant, T is the temperature and γ is the surface tension.

In order to comprehend the effect of Ag particle size on sintering, SEM images of two pastes with macro and nano sized Ag particles were taken to compare the porosity in the gridlines after firing process. Figure 4.4 and Figure 4.5 show the images of two printed gridlines for nano and macro Ag particle respectively. As marked in the image, the sizes and the amount of pores in gridline with nano sized Ag particles is much less than its counterpart, which results in lower gridline resistance for nano particles and hence lower series resistance. A grid model was used to investigate the effect of only gridline resistance on fill factor. In Figure 4.6, the FF is varying from 77.3% to 79.8% with decreasing gridline resistance from ~0.85 to ~0.35 $\Omega \cdot cm^2$, which resulted in 0.2% gain in absolute efficiency. Therefore using nano particles instead of macro size would provide an efficiency improvement due to sintering process alone.

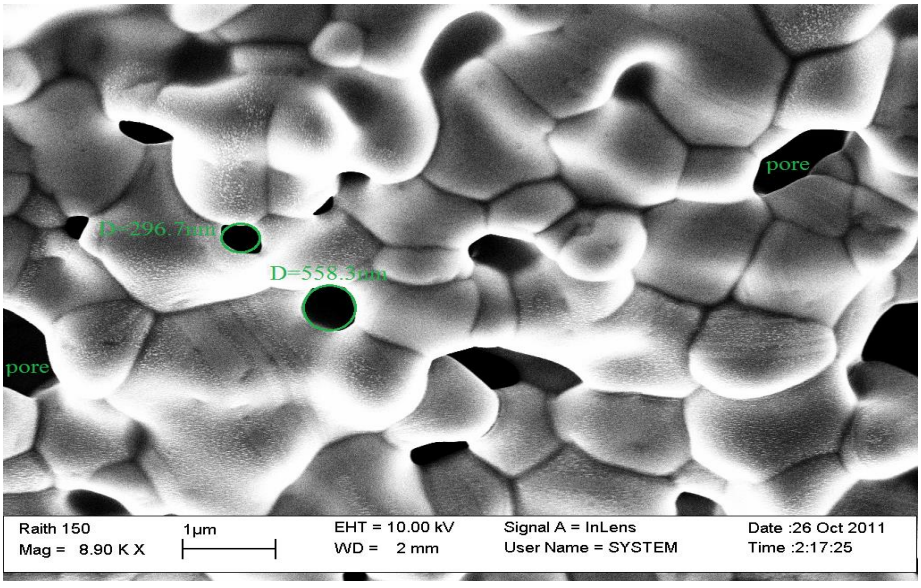

Figure 4.4: SEM image of printed gridline with nano size Ag particle. The average pore size is ~600 nm in diameter

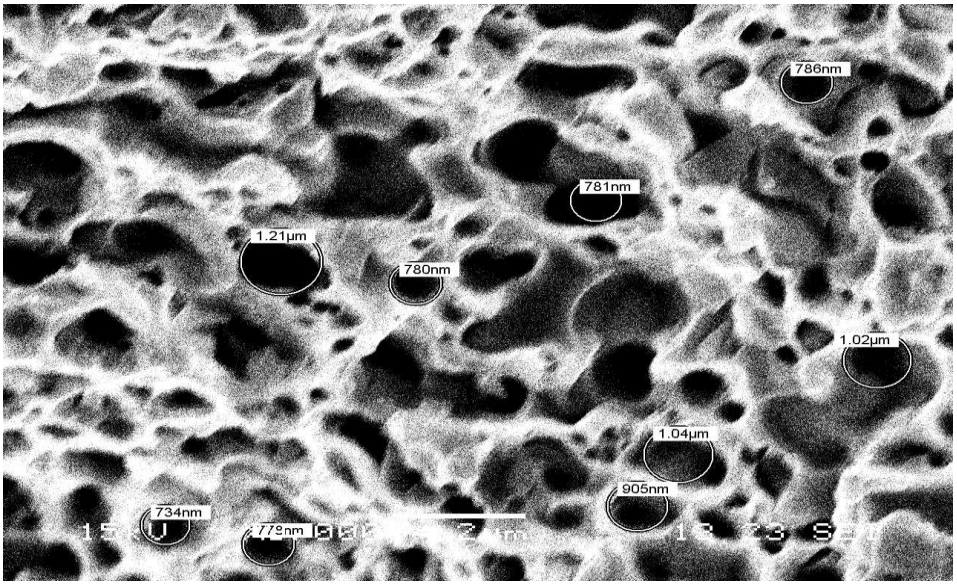

Figure 4.5: SEM image of printed gridline with macro size Ag particle. The average pore size is ~1µm in diameter

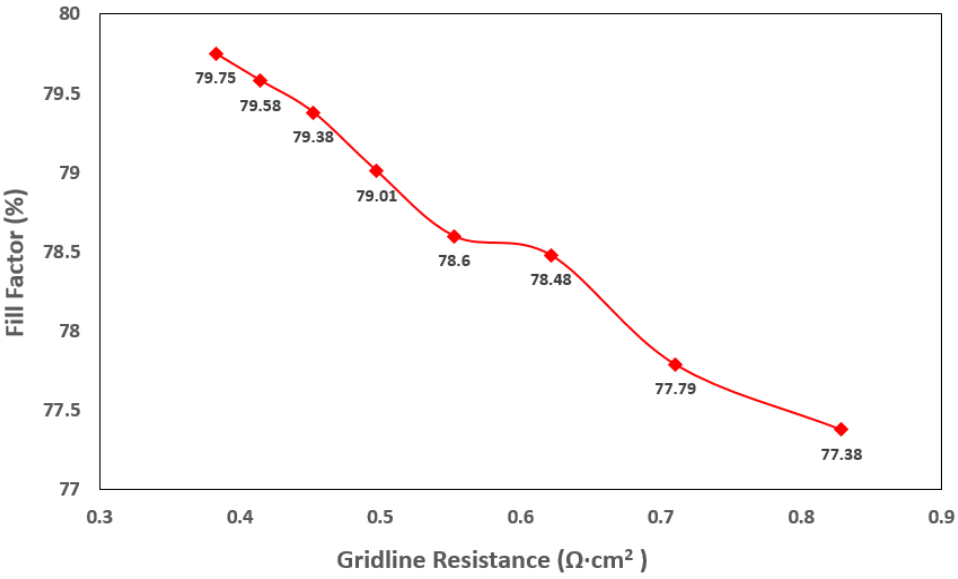

Figure 4.6: The dependence of FF on gridline resistance

4.3 Firing Process Effects on Sintering of Ag particles

It is well known that the performance of industrial silicon solar cell has a strong dependence on the final co-firing step whose typical profile is shown in Figure 4.7. because during co-firing;

i. the contact between Ag and Si is formed,
ii. line resistance is affected due to sintering process, and
iii. aluminum back contact are finalized.

Since all of above-steps has a contribution to series resistance, fill factor (FF) and hence the overall efficiency is strongly influenced by final co-firing profile of metallization.

Sintering of Ag particle is also a temperature dependent process, as seen in Eq. 4.3, and the variables such as viscosity, diffusivity, and thixotropy, discussed in rheology are expressed as an exponential function of temperature. Therefore, analyzing firing process of solar cells is essential for further understanding of the whole mechanism of sintering.

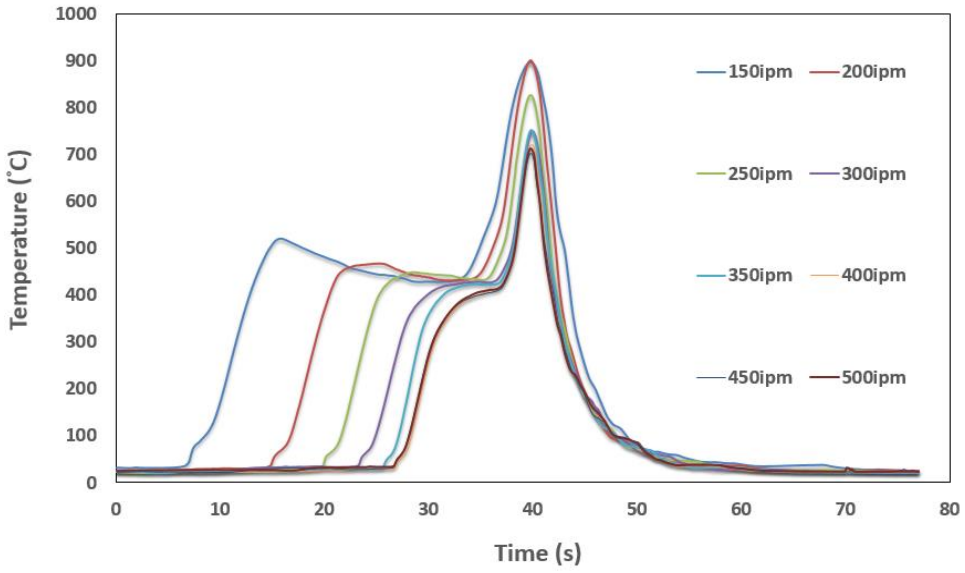

Figure 4.7: A typical firing profile for conveyor-belt furnace depending on belt speed of 150ipm to 500ipm

4.3.1 Effect of High Temperature Firing Process on Microstructure at the Interface of Ag/Si

The glass frit in the Ag paste is one of the most important factors determining the contact resistance, and ultimately the cell performance. The reactive molten glass frit on high temperature etches through the ARC and a very thin silicon surface (emitter) layer. At the interface of Ag/Si, there is a formation of a residual glass layer left behind, which creates metal-oxide-semiconductor (MOS) structure, (see Eq.4.11 and 4.12) and Ag crystallites formed by precipitation of Ag particles dissolved in glass frit [61, 62] (see Eq. 4.13, 4.14 and 4.15). While the glass layer behaves as a conductive channel for tunneling, if it is thin enough (~0.1nm), Ag crystallites embedded in glass layer act as current pick-up points. The uniformity of Ag crystallites and thin glass layer provides less contact resistance which contributes to higher fill factor.

$$6Ag_2O_{(glass)} + Si_3N_{4(wafer)} \rightarrow 12Ag + 3SiO_2 + 2N_2 \quad (4.11)$$

$$2\mathrm{PbO}_{\mathrm{Glass}} + SiN_2 \rightarrow 2Pb + \boldsymbol{SiO_{2\ glass}} + N_2 \quad (4.12)$$

$$4Ag + O_2 \rightarrow 4Ag^+ + 2O^{2-} \quad (4.13)$$

$$4Ag^+ + 2O^{2-} + SiN_x \rightarrow \boldsymbol{4Ag} + SiO_2 + \frac{x}{2}N_2 \quad (4.14)$$

$$4Ag^+ + 2O^{2-} + Si \rightarrow \boldsymbol{4Ag} + SiO_2 \quad (4.15)$$

Hilali reported [63] that there is an Ag particle size dependence of Ag crystallite formation and this is also explained by Herring's scaling law [64] It is said that as the Ag particle size gets larger in the paste (in macro scale), the density of Ag crystallites formed at the interface is higher. However, during sintering, dissolution of Ag particles into the molten glass frit also takes place, which will form crystallites by precipitating into Si when cooling down. Ag particles get larger due to long firing time before the lead oxide (PbO) in glass frit reaches to ~580 ˚C to be molten PbO which dissolves Ag particles in. So sintering should be correlated with firing time. To overcome this issue, either Ag particle sintering must be slowed down by a sintering inhibitor, which requires another additive to the paste, or the firing time should be decreased to lower the pace of sintering, which gives Ag particles enough time to be dissolved. From Eq. 4.3 if the belt speed (or firing time) is increased from 150ipm to over 300ipm, which cuts the firing time in half, the sintering rate will be reduced by ~35%. So the drop in the sintering rate will give Ag

particles a chance to be dissolved and hence precipitation onto Si at Ag/Si interface. Therefore formation of Ag crystallites is more related with firing time than particle size.

Besides crystallite formation, Cooper et al., [65] have shown that Ag/Si interfacial glass-layer thickness decreases as sinter dwell time (the time that the wafer spends above 600 ^{o}C) decreases with no dependence of Ag particle size. As the belt speed is increased, the thickness of glass layer gets thinner which eases tunneling of electrons from silicon to Ag bulk. It was shown that 0.5%$_{abs}$ efficiency gain was achieved by decreasing dwell time from 5.2s to 1.2s due to the reduction of 0.34 Ω-cm^2 in series resistance (R_S).

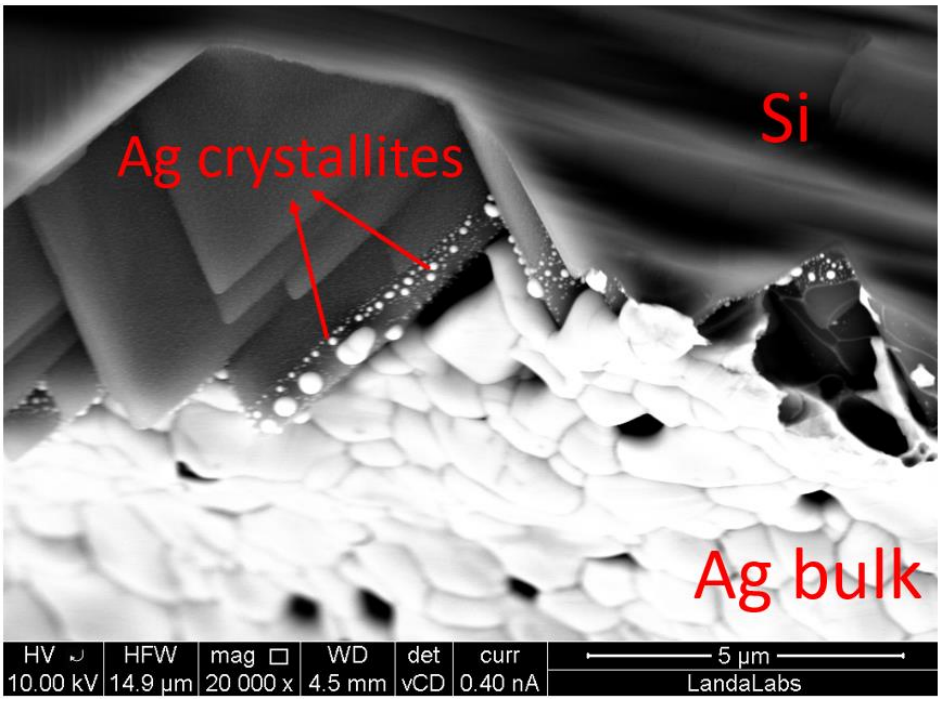

Figure 4.8: Ag crystallite and glass layer formation at the interface of Si and Ag bulk.

To prove the gain in the FF assisted by formation of uniform Ag crystallites, thin glass layer (see Figure 4.8) and reduced porosity by fast firing process, screen printed mono and multi crystalline silicon solar cells were fired with different belt speed from 200ipm to 400ipm. Figure 4.9 shows the graphs of the FF as a function of belt speed (firing time) of IR belt furnace at ~750°C peak temperature. As increasing the belt speed, a gain of 2.8% and 3.9% in the FF for mono and multi crystalline respectively can be achieved. It is demonstrated from the graphs that belt speed of 350ipm is an optimum point to fire solar cells.

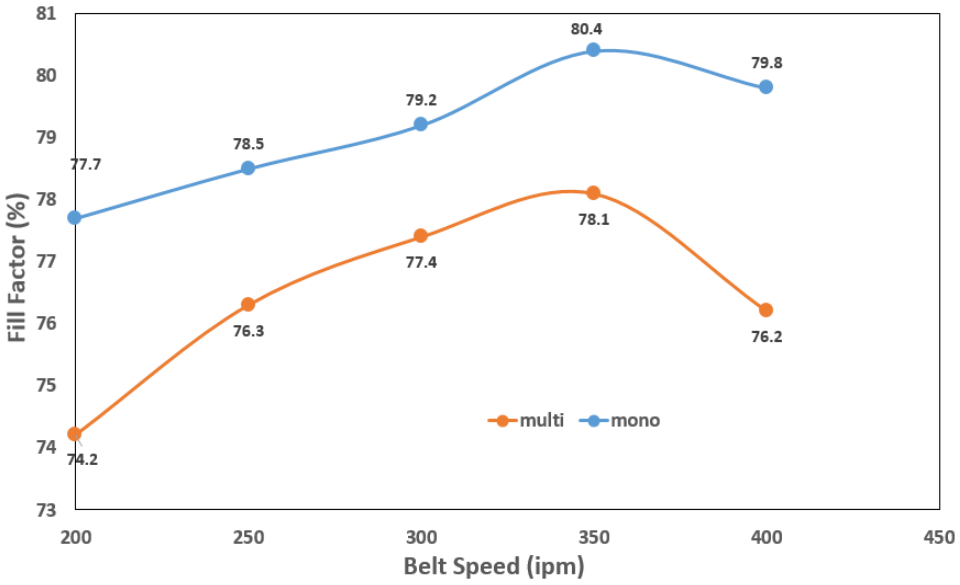

Figure 4.9: Efficiency measurements of mono and multi crystalline silicon solar cells depending on belt speed

The series resistances (R_s) of the same cells is measured to investigate the variations in the FF. It is found that the decreased contact and gridline resistance aid higher FF through lower R_s as illustrated in Figure 4.10. Therefore lowering firing time is beneficial to obtain low gridline and contact resistances. To combine the

benefits of reducing porosity using nano Ag particles, formation of thin glass layer and uniform crystallites, a very short firing time (< 1 min) is necessary to achieve a low R_S and hence high FF.

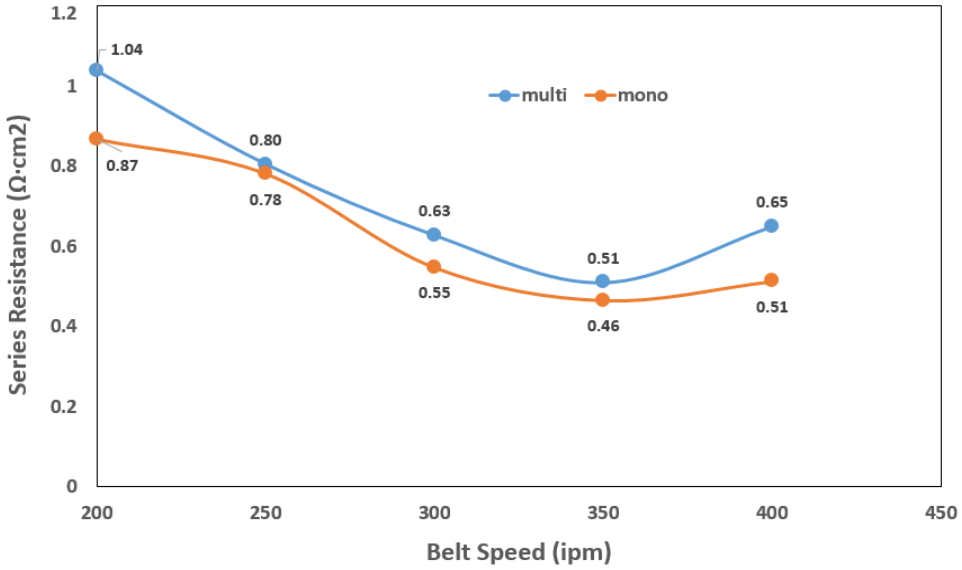

Figure 4.10: Series resistance of mono and multi crystalline silicon solar cells changing with belt speed

4.4 Conclusion

This chapter is aimed at investigating and validating the influence of Ag particle size on sintering of gridline and contact on silicon solar cell. Microstructural analyses of the contact show that the nano-sized Ag particles is advantageous in lowering both the contact and gridline resistances. Also, sintering time (dwell time at peak sintering temperature), which is synonymous with the belt speed is critical in determining the total resistance. The longer dwell time results in thicker residual glass layer, and less Ag crystallites at the interface of Ag/Si. This decreases the conduction of carriers from the semiconductor. The shorter dwell time, on the other

hand decreases the glass formation at the Si/Ag interface and has resulted in FF of ~80.4%.

CHAPTER 5 :
IMPLEMENTATION OF METTALIZATION PATTERNS

5.1 Solar Cell Fabrication Sequence

The fabrication of Al-BSF and PERC solar cell structures start with the saw damage removal[4], followed by acidic texturing and $POCl_3$ diffusion at high temperature in a conventional diffusion furnace to form the emitter. Next, phosphor-silicate glass (PSG) removal is performed along with edge isolation that removes the phosphorous from the edges to ensure the front emitter is electrically isolated from the back. The rear side polishing takes place during PSG removal in order to ensure the rear junction is completely removed Then ARC layer of SiN_X is deposited on the front surface usually by plasma enhanced chemical vapor deposition (PECVD). As shown in Figure 5.1, PERC structure differs from Al-BSF at the backside. It utilizes Al_XO_Y/SiN_X stack passivation. to enhance the reflection on the back side and to passivate the dangling bonds to reduce back surface recombination. Laser ablated openings are also applied to the stack layer (Al_XO_Y/SiN_X) to assure proper formation of local Al-BSF on Si. Screen printing of Ag paste was applied for the front contacts and Al paste for the back. As a last step of fabrication, contact co-firing process is applied to finalize the cells (see Figure 5.2).All of the front gridline designs discussed and modelled in the previous chapter are applied to cells in order to see which design gives the most benefit in terms of

[4] Cutting silicon ingots into wafers leaves the surface damaged and cutting slurry due to the action of the saw. Hot solution of NaOH is used to clean the slurry and ~10 μm of damaged Si.

both cost and efficiency. To do so, the electrical and optical parameters are compared.

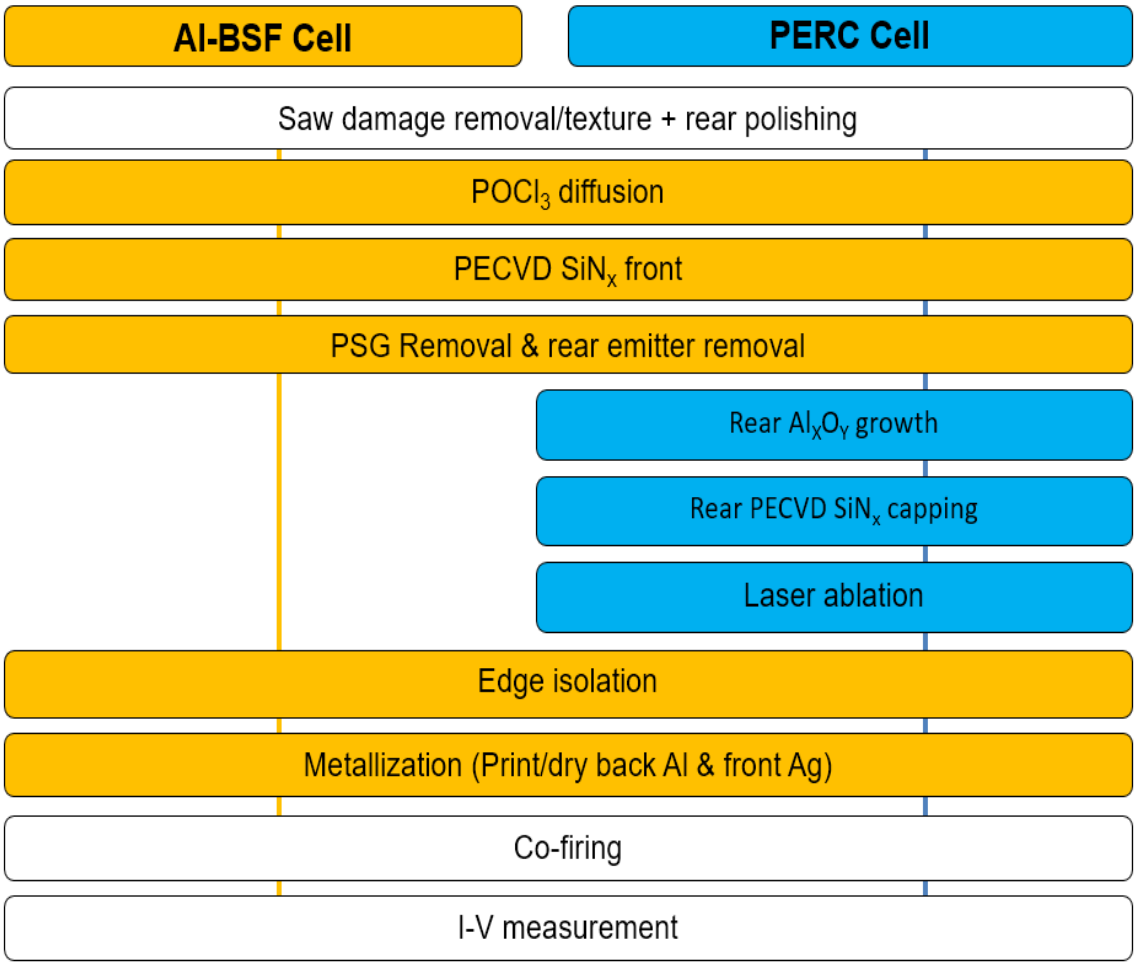

Figure 5.1: Cell processing sequence for Al-BSF and PERC solar cell structures

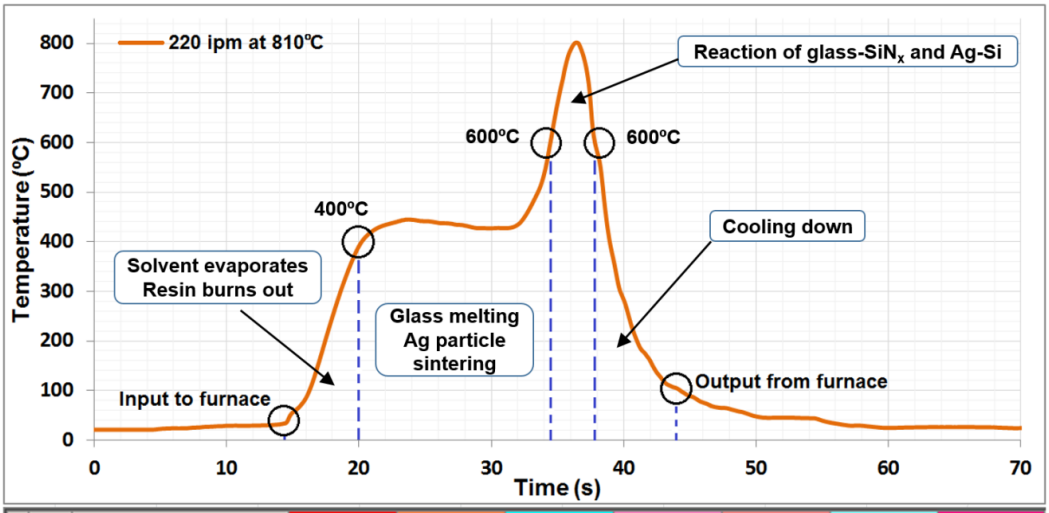

		Maximum Temperature	Maximum Positive Slope	Maximum Negative Slope	Time Between Temperature	Time Above Temperature: Rising (+)	Time Above Temperature: Falling (+)	Time Above Temperature: Total (+/-)
					390-430°C	600°C	600°C	600°C
Show All		°C	°C/sec	°C/sec	sec	sec	sec	sec
A2	Sensor 2 Location	801.7	127.83	-190.04	1.6	1.9	1.4	3.4
	Range	0.0	0.00	0.00	0.0	0.0	0.0	0.0
	Average	801.70	127.830	-190.040	1.60	1.90	1.40	3.40
	Std Deviation	-1.#IO	-1.#IND	-1.#IND	-1.#IO	-1.#IO	-1.#IO	-1.#IO
		Template: C:\ECD\MegamoleMAP\Template\DataTableCalculations.tpf						

Figure 5.2: A schematic of the firing profile with process occurring at different temperatures

5.2 Light I-V Measurements

I-V measurements, the V_{OC}, J_{SC}, FF and η, of each design, 3-, 4-, 5BB, mentioned in previous chapter for Al-BSF and PERC structure are summarized in the tables below. The measurements are the average of multiple cells and the best results are highlighted in the tables. It is shown that using uneven busbars rather than continuous rises the absolute efficiency ~0.2% regardless of the structure of the solar cell. The efficiencies for Al-BSF cells are in the range of 18.8%-19.8% with average FF of 79% while the PERC cells have the efficiency range of 20.43% - 21% with the FF more than 80%. Since the total busbar width is kept constant for each new designs regardless of number of busbars, the variation in the V_{OC} of the cells

are very small. However, having uneven busbars and segmentations on the gridlines lead to a slight enhancement in the J_{SC} because of reduced shadowing loss that will be discussed in detail in the next section. The FF, on the other hand, is decreased as the segmentation on the gridlines increases due to increasing resistive losses. In conclusion, overall absolute efficiency can be improved at least ~0.5% by using uneven busbars in conjunction with segmentations on the gridlines.

Table 5.1: Average I-V measurements for 3BB Al-BSF silicon solar cells

Cell ID	V_{OC} (mV)	J_{SC} (mA/cm2)	FF (%)	Efficiency (%)
Conventional	639.1	37.37	79.1	18.88
Uneven BB	641.6	37.68	78.8	19.05
1 mm segmentation	641.7	37.70	78.7	19.03
2 mm segmentation	641.7	37.73	78.7	19.04
3 mm segmentation	641.7	37.74	78.6	19.03
4 mm segmentation	641.8	37.76	78.4	18.99

Table 5.2: Average I-V measurements for 3BB PERC silicon solar cells

Cell ID	V_{OC} (mV)	J_{SC} (mA/cm2)	FF (%)	Efficiency (%)
Conventional	654	39.21	79.7	20.43
Uneven BB	655.1	39.61	79.2	20.55
1 mm segmentation	655.1	39.63	79.1	20.53
2 mm segmentation	655.1	39.65	79	20.52
3 mm segmentation	655.1	39.66	79	20.52
4 mm segmentation	655.2	39.68	78.8	20.48

Table 5.3: Average I-V measurements for 4BB Al-BSF silicon solar cells

Cell ID	V_{OC} (mV)	J_{SC} (mA/cm2)	FF (%)	Efficiency (%)
Conventional	639	37.17	79.5	18.88
Uneven BB	641.7	37.88	79.2	19.25
1 mm segmentation	641.8	37.90	79.1	19.24
2 mm segmentation	641.8	37.93	79.1	19.25
3 mm segmentation	641.8	37.94	78.9	19.21
4 mm segmentation	641.8	37.96	78.4	19.10

Table 5.4: Average I-V measurements for 4BB PERC silicon solar cells

Cell ID	V_{OC} (mV)	J_{SC} (mA/cm2)	FF (%)	Efficiency (%)
Conventional	655.8	39.12	80.1	20.54
Uneven BB	656.3	39.81	80	20.9
1 mm segmentation	656.3	39.83	79.9	20.88
2 mm segmentation	656.3	39.86	79.9	20.9
3 mm segmentation	656.3	39.87	79.7	20.85
4 mm segmentation	656.3	39.88	78.6	20.83

Table 5.5: Average I-V measurements for 5BB Al-BSF silicon solar cells

Cell ID	V_{OC} (mV)	J_{SC} (mA/cm2)	FF (%)	Efficiency (%)
Conventional	640	38.19	79.7	19.48
Uneven BB	641.9	39	79.5	19.9
1 mm segmentation	641.9	39.01	79.4	19.88
2 mm segmentation	641.9	39.04	79.4	19.89
3 mm segmentation	641.9	39.05	79	19.8
4 mm segmentation	641.9	39.05	78.9	19.77

Table 5.6: Average I-V measurements for 5BB PERC silicon solar cells

Cell ID	V_{OC} (mV)	J_{SC} (mA/cm2)	FF (%)	Efficiency (%)
Conventional	655.9	39.52	80.5	20.86
Uneven BB	656.8	39.89	80.2	21.01
1 mm segmentation	656.8	39.92	80.1	21
2 mm segmentation	656.8	39.95	80.1	21.01
3 mm segmentation	656.9	39.96	80	20.99
4 mm segmentation	656.9	39.97	79.8	20.95

Figure 5.3 shows the champion 4-BB 2 mm segmented PERC cell with V_{OC} of 654 *mV*, J_{SC} of 39.94 *mA/cm2* and FF of 81.7% result in 21.35% conversion efficiency. The fundamental strategy to achieve a high efficient silicon solar cell includes

i. improved surface passivation to enhance the V_{OC} and
ii. optimizing the gridlines so that shadowing and resistive losses are minimal to increase the J_{SC} and FF.

These goals are achieved by the champion PERC cell, shown in Figure 5.3, by having passivated back surface for the high V_{OC} and a gridline design that increases the short circuit current while keeping series resistance relatively low at ~0.3 R_S ($\Omega \cdot cm^2$) to keep the FF higher.

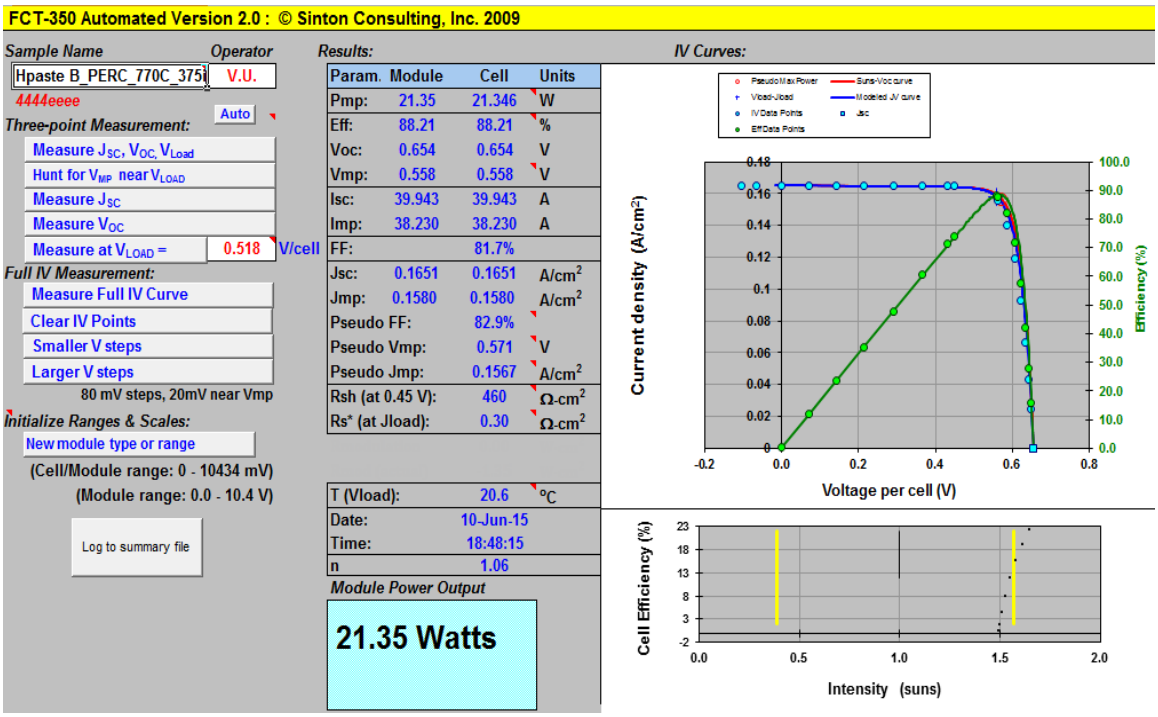

Figure 5.3: *I-V* Data for the best 4BB 2mm segmented fingers PERC solar cell

5.3 IQE Analysis

In order to have a better understanding, Figure 5.4 compares the internal quantum efficiency (IQE)[5] for 5 BB with 2 mm segmentation PERC and Al-BSF silicon solar cells. It is clear from the graph that passivation stack layer on the back surface of the PERC cell greatly improves the spectral response than its counterpart. The similar blue response on the front surface indicates that the surface passivation and doping of both cells are alike. Since gridline pattern for both cells are same, the shading on the front surface are about 4% so the reflectance responses are almost identical.

[5] IQE is the ratio of the number of carriers collected by the solar cell to the number of photons of a given energy incident on the solar cell.

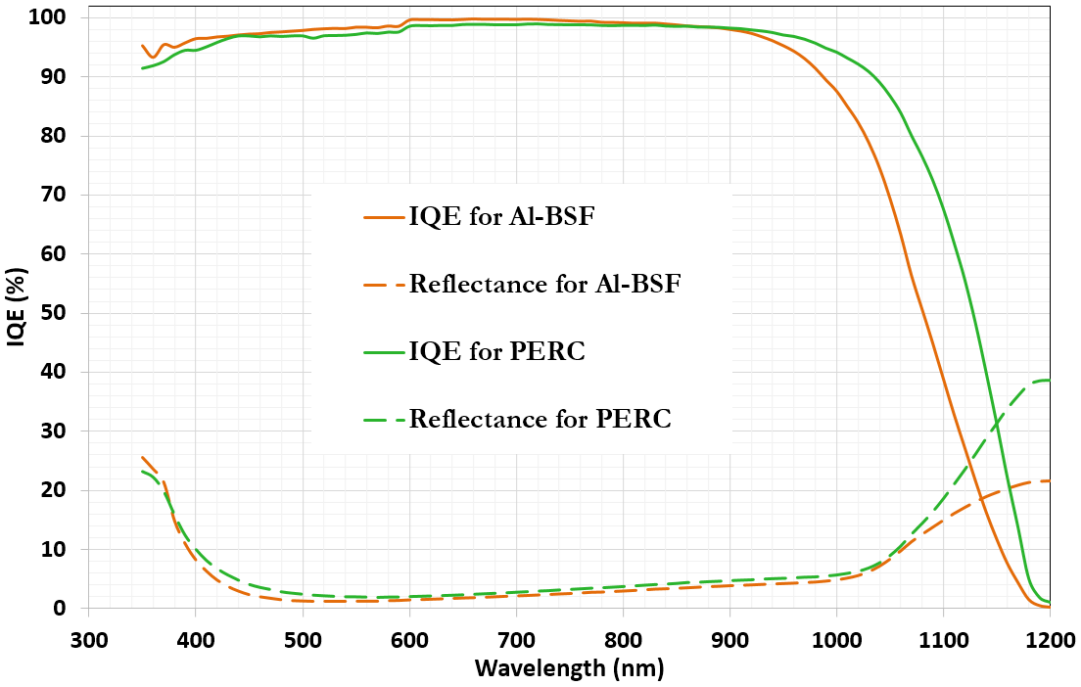

Figure 5.4: IQE analysis comparison for 4BB Al-BSF and PERC cells

5.4 Suns V_{OC} Measurements

Suns-V_{OC} measurements of Al-BSF and PERC cells for different number of busbars were taken to investigate the junction parameters such as leak currents (J_{01} and J_{02}), ideality factor (n), and pseudo FF (pFF) and efficiency. Table 5.7 and Table 5.8 summarizes the average Suns-V_{OC} data for the Al-BSF and PERC cells respectively for 3-, 4-, and 5 BB cells.

The difference in the V_{OC} between Al-BSF and PERC structure comes from the passivation layer on the back side of the PERC cells. The Suns V_{OC} measures the parameters with no series/shunt resistance on a cell, which ultimately shows the solar cell's real potential. The pseudo fill factor (pFF) of 83% for PERC cells indicates the cell has a great potential to go higher efficiencies such as >22% while for the Al-

BSF it is >20%. The low junction reverse saturation currents, J_{01} and J_{02}, for both structures along with ideality factors indicate that both cells have good junction properties. Other than the difference in the VOC, all parameters are similar which implies that the series resistance of the cells is the determining parameter.

Table 5.7: Average Suns V_{OC} measurements for 3-, 4-, 5 BB Al-BSF cells

Cell ID	V_{OC} (mV)	pFF (%)	n-factor (@ 0.1sun)	J_{01} (A/cm²)	J_{02} (A/cm²)	Pseudo Efficiency
3 BB	643	82.1	1.06	$4.5 \cdot 10^{-13}$	$5.37 \cdot 10^{-9}$	20.2%
4 BB	642	82.5	1.05	$4.42 \cdot 10^{-13}$	$7.93 \cdot 10^{-9}$	20.5%
5 BB	643	82.6	1.05	$4.32 \cdot 10^{-13}$	$5.04 \cdot 10^{-9}$	20.6%

Table 5.8: Average Suns V_{OC} measurements for 3-, 4-, 5 BB PERC cells

Cell ID	V_{OC} (mV)	pFF (%)	n-factor (@ 0.1sun)	J_{01} (A/cm²)	J_{02} (A/cm²)	Pseudo Efficiency
3 BB	656	83.6	1.04	$5.5 \cdot 10^{-13}$	$7.37 \cdot 10^{-9}$	22.3%
4 BB	655	83.3	1.05	$5.12 \cdot 10^{-13}$	$6.85 \cdot 10^{-9}$	22.5%
5 BB	658	83.9	1.04	$5.41 \cdot 10^{-13}$	$6.14 \cdot 10^{-9}$	22.4%

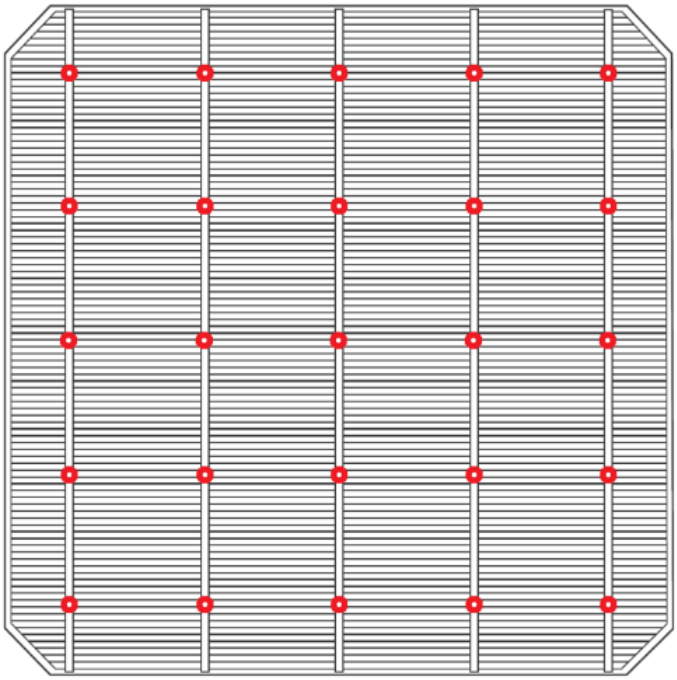

Figure 5.5: Suns V_{OC} measurement probe points marked red for the contour mapping

In order to visualize the reason for the difference between the measured FF and pFF, Suns-V_{OC} measurements were taken at the multiple probe points, shown in Figure 5.5, for 5 BB Al-BSF and PERC cells. Also the R_S is calculated for each measurements according to the equation below;

$$R_s = \frac{V_{oc} \cdot J_{sc} \cdot (pFF - FF)}{{J_{mp}}^2} \tag{5.1}$$

Figure 5.6 compares the contour map of the pFF for 5 BB Al-BSF and PERC cells, which both shows small variations in the same cell. Since the R_S is not taken into account in the pFF the results are expected to be wafer dependent rather than metallization. Figure 5.7, on the other hand, shows the R_S contour maps for the same cells that explains why we have a difference between the pFF and measured FF.

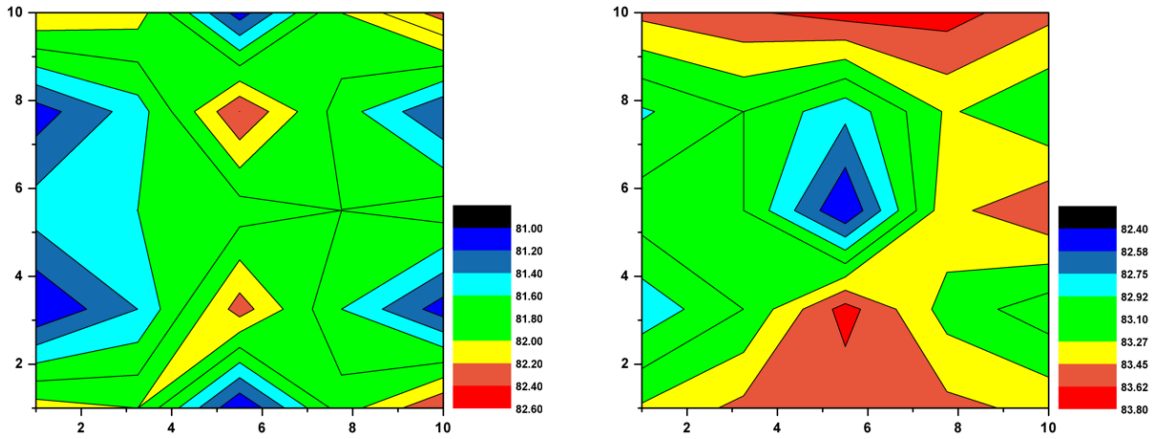

Figure 5.6: Contour map of pFF for 4 BB Al-BSF (left) and PERC (right) cells

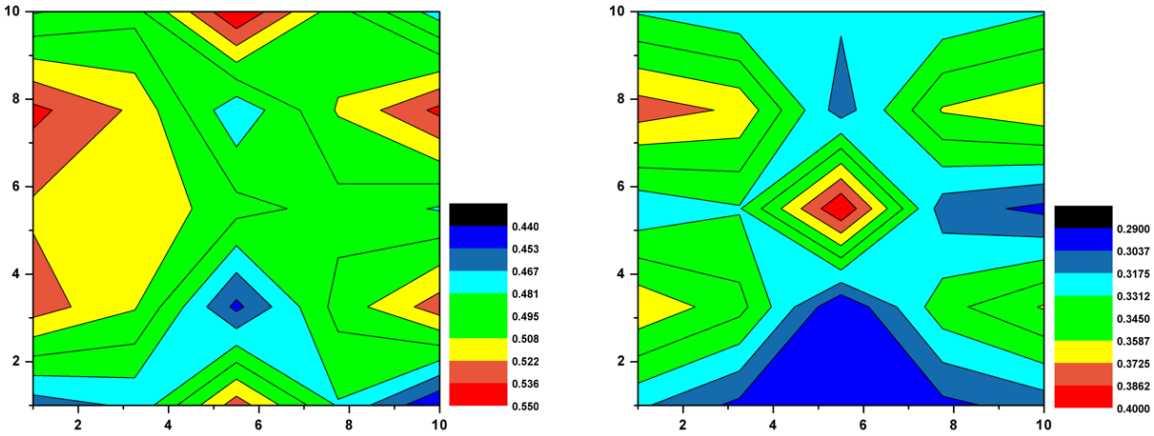

Figure 5.7: Contour map of R_S for 4 BB Al-BSF (left) and PERC (right) cells

5.5 Cost Analysis of Gridline Designs

The gridlines with segmentation in conjunction with uneven busbars has exhibited high potential to increase the efficiency. Utilizing the proposed screen designs can decrease the metal coverage from ~5.9% up to ~3.8% (see Table 5.9) while saving the amount of Ag used per cell. For instance, a regular 4-BB design having 60µm gridline width, 1mm busbars width, and 15µm height, has a 5.9% metal coverage. Ag usage per cell is ~75 mg will correspond to 4.4¢ per cell, given Ag price

of $0.55/g . On the other hand, with uneven 4-BB, 2mm gridline segmentation width, exhibits a 3.77% metal coverage and only ~54 mg of Ag, ~21 mg lower than the previous case and results in 3¢ per cell. The difference translates to ~30% Ag cost savings per cell. For a 100MW plant, it saves ~$1 million. Note that in this calculation, the density of Ag is taken as 10.49g/cm^3. The cost calculation is based on today's (04/15/2018) silver price of $0.55/g. Table 5.10 shows the Ag usage for each scenario. illustrating the experimental Ag usage per cell for each scenario and the metal coverage so that the cost can be calculated for each case. Best case scenario for both efficiency and Ag cost saving appears to be 5BB with 2mm gridline segmentation (highlighted in the Table 5.9 and Table 5.10).

Table 5.9: Modeled Shading Area with Different Screen Designs

Screen design	3BB	4BB	5BB
EB-CG	5.65%	5.90%	6.25%
UEB-CG	4.19%	4.19%	4.19%
UEB-1mm SG	4.16%	4.14%	4.12%
UEB-2mm SG	**4.12%**	**4.09%**	**4.06%**
UEB-3mm SG	4.09%	4.04%	3.99%
UEB-4mm SG	4.06%	3.99%	3.92%
UEB-5mm SG	4.02%	3.94%	3.85%

Table 5.10: Ag Usage with Different Screen Designs

Screen design	3BB	4BB	5BB
EB-CG	74.4m	74.4mg	74.4mg
UEB-CG	55.2mg	55.2mg	55.2mg
UEB-1mm SG	54.6mg	54.5mg	54.3mg
UEB-2mm SG	**54.2mg**	**53.9mg**	**53.4mg**
UEB-3mm SG	53.5mg	53.2mg	52.5mg
UEB-4mm SG	53.2mg	52.5mg	51.6mg
UEB-5mm SG	52.8mg	51.8mg	50.7mg

5.6 Conclusions

It was demonstrated experimentally that the concept of uneven busbars with segmented gridlines discussed in previous chapter benefits both Al-BSF and PERC structure silicon solar cells in terms of efficiency and cost. This was confirmed both theoretically (Chapter 3) and experimentally (chapter 4). Based on the measured *I-V* data, the cell efficiency can be increased by ~0.5% absolute when the innovative gridline patterns are implemented. It can be concluded that 5 BB with 2 mm segmentation on the gridline have a great potential to take the efficiency for Al-BSF over 20% and for PERC over 22%. Same design also decreases the Ag usage by 30 g/cell.

CHAPTER 6 :
COST REDUCTION THROUGH HIGH VOLUME MANUFACTURING

The cost of processing solar cell processing can be decreased through

i. the use of less Ag metal paste in conjunction with high sheet resistant emitters,
ii. decreased number of processing steps, and
iii. increased throughput with increased output power.

By increasing the throughput without additional cost in equipment and loss in efficiency, the overall cost of cell processing can be decreased. In this chapter, the impact of the belt speed of an IR belt furnace on the cell performance is investigated.

The rapid thermal processing (RTP) has been deployed for contact co-firing because of its high throughput accompanied by low contact resistance and uniform BSF formation through precise control of the ramp up/down rates. Meemongkolkiat et al [66] showed that ≥100 °C ramp up/down rates were required in a single tube RTP furnace, in order to achieve high open circuit voltage (V_{OC}) and low contact resistance. The RTP is also beneficial for the low thermal budget because the burst of energy from the infrared (IR) lamp can be used to heat only the desired region of the sample [67]. It started with single wafer tube system with potential promise for screen printed contact firing . And in 2005 [68], the belt furnace utilizing the IR lamps with the fast ramps to implement the RTP concept on the production floor was introduced by several manufacturers including, TP Solar, Centrotherm, Despatch Solar etc.

The performance of a solar cell greatly depends on the co-firing step. During firing; the front contact between silicon and Ag is formed, which can impact both the contact and gridline resistances as well as the uniformity of the aluminum back surface field (BSF) formation [49, 69-72]. While high ramp up rate enhances the uniform BSF, the short dwell time (the time above ~600 °C) at peak temperature ensures appropriate Al-BSF thickness. The contact resistance, on the other hand, is impacted by the ramp down rate. The fast ramp down rate enhances the cooling of the wafers to room temperature and hence the elimination of further oxide growth at the interface of metal/silicon. In this chapter, two belt speeds, 230 ipm and 375 ipm were used, which are quite higher than that used by the PV industry and thus, higher ramps up/down than the industry.

6.1 Back Surface Field Formation

Following the printing of Al paste on the back side, the cell first will be dried at ~200°C to evaporate all the solvents in the paste. After the front printing of Ag paste, the cell with printed metal contacts will be transferred to an IR-belt furnace for a three-step co-firing process: burn-out, firing and cooling (see Figure 5.2). And the formation of Al-BSF by the alloying of Al on silicon substrate occurs based on the mechanism as follows [73-76]:

i. At 300-400°C, the organic binders are burnt out;

ii. above 577 °C (the Al-Si eutectic temperature), the alloying of Al and Si starts to take place whereby Si dissolves into the Al-Si melt, leading to a homogeneously distributed liquid phase;

iii. In the cooling down process, silicon is rejected from the Al-Si melt and epitaxially recrystallizes at the interface of Al/Si, leading to the growth of Al doped p^+ BSF. When the alloying temperature is reduced to the eutectic temperature, the final solidification of the residual Al-Si melt happens, creating a compact Al-Si layer of eutectic composition above the Al-p^+ region with ~12 wt % Si.

Generally, the quality of BSF has a strong dependence on the amount of deposited Al paste and the firing condition such as the ramp-rate, the peak temperature and the dwell time [72, 75, 77]. The thickness of the regrown Al doped silicon layer is determined by the amount of aluminum paste used [72] and the amount of Si dissolved into the melt at peak firing temperature [73, 78]. The thickness ($d_{Si,dis}$) and weight ($m_{Si,dis}$) of dissolved silicon can be calculated with the corresponding relationship according to [79];

$$d_{Si,dis} = \frac{m_{Si,dis}}{A \cdot \rho_{Si}} = \frac{m_{Al}}{A \cdot \rho_{Si}} \times \frac{F(T_{peak})}{1 - F(T_{peak})} \tag{6.1}$$

where A is the screen-printed total area, ρ_{Si} the density of Si and $F(T_{peak})$ the atomic weight percentage of Si in the molten phase at the peak alloying temperature.

Since the percentage of Al in the Al doped p^+ layer is negligible, the volume of Al paste particles after final solidification can be assumed to be the same as

deposited. Therefore the thickness of the eutectic layer ($d_{Si,eut}$) corresponds to the weight percentage of Si in the eutectic layer, which can be calculated as:

$$d_{Si,eut} = \frac{m_{Al}}{A \cdot \rho_{Si}} \times \frac{F(T_{eut})}{1 - F(T_{eut})} \tag{6.2}$$

The BSF thickness (W_{BSF}) is thus obtained by subtracting $d_{Si,eut}$ from $d_{Si,dis}$:

$$W_{BSF} = \frac{t_{Al} \cdot \rho_{Al}}{\rho_{Si}} \left(\frac{F(T_{peak})}{1 - F(T_{peak})} - \frac{F(T_{eut})}{1 - F(T_{eut})} \right) \tag{6.3}$$

where t_{Al} represents the thickness of screen-printed Al layer, ρ_{Al} the density of Al.

From Eq. (6.3), the quality of Al-BSF depends on the thickness of deposited aluminum and the peak alloying temperature, and W_{BSF} can be improved by increasing t_{Al} or T_{peak}. However, a critical temperature exists for a given screen-printed thickness. This critical temperature decreases with increased amount of printed Al paste [75]. Al melt has a large surface tension and tends to ball up during the firing step, especially when the firing temperature exceeds the critical temperature, resulting in serious lateral thickness inhomogeneity of BSF [74].

On the other hand, the higher the peak alloying temperature, the more heavily Al-doped p^+ region will be obtained. For the peak alloying temperatures ranging from 740-900°C, the Al-doped p^+ layer have a peak concentration in the range of $1\text{-}3\times10^{18}$ cm^{-3}, while in most p-type silicon wafers, the base doping concentration is lower than 2×10^{16} cm^{-3}, resulting in a high-low junction from the difference in doping concentration [75]. The electric field created in between the high and low doped region introduces a barrier that keeps the minority carriers away

from high recombination rear contact, which reduces back surface recombination velocity (BSRV).

6.2 Cell Fabrication

Large-area (242 cm^2) commercial boron doped p-type Cz-Si wafers 2.5 Ω·cm were used. A 4-busbar PERC structure was used in this experiment. The cell processing includes: (i) random texturing of both front and back sides, (ii) $POCl_3$ diffusion, (iii) edge isolation plus backside planarization and phosphorus removal, (iv) Al_2O_4/SiN_X deposition on the backside, (v) SiN_X on the front side, (vi) backside laser opening for Al BSF, (vii) Al printing on the backside and dry, (viii) Ag/Al back pad and dry, (ix) front side Ag screen printing and dry. And finally (x) contact co-firing in IR belt furnace at two belt speeds, 230 and 375 ipm which typical profile is shown in Figure 6.1. It should be noted that the actual peak temperatures on the cells are the same ~785 °C even though the set temperatures are different. This was followed by light current-voltage measurement under standard conditions; Suns V_{OC}, IQE and contact resistance measurements.

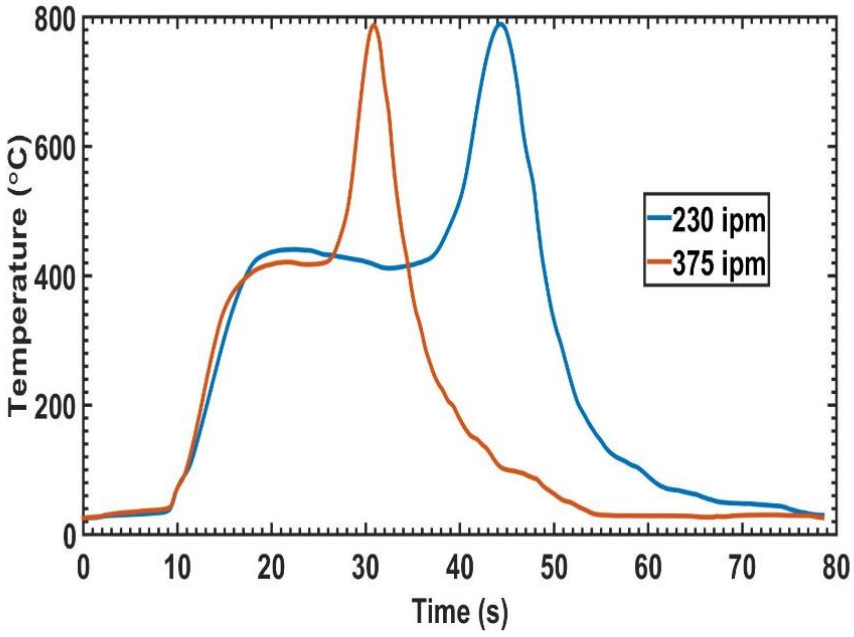

Figure 6.1: Typical firing profile for rapid thermal processing with 230 ipm and 375 ipm

6.3 Results and Discussion

The average and best electrical output parameters for the cells fired at 230 and 375 ipm belt speeds ~785 °C peak temperature are listed in Table 6.1. From Table 6.1, V_{OC} and fill factor (FF) are higher for the 375 ipm than the 230 ipm counterpart. FF is higher because of the lower series resistance (R_S). Contact resistance (R_C) measurements indicate that the increase in the FF for high belt speeds can be attributed to better contact quality. Fast ramp down rates (up to ~200 °C) (see Fig. 4.2.) for the 375 ipm belt speed brings the cells to fast cooling at room temperature and prevents oxide to grow underneath the contacts, hence very low contact resistance. From Figure 6.2a, at 375 ipm, the dwell time is as short as ~2.2 s while the ramp up and down rates are at maximum of 167 °C and 192 °C respectively, as in Figure 6.2b.

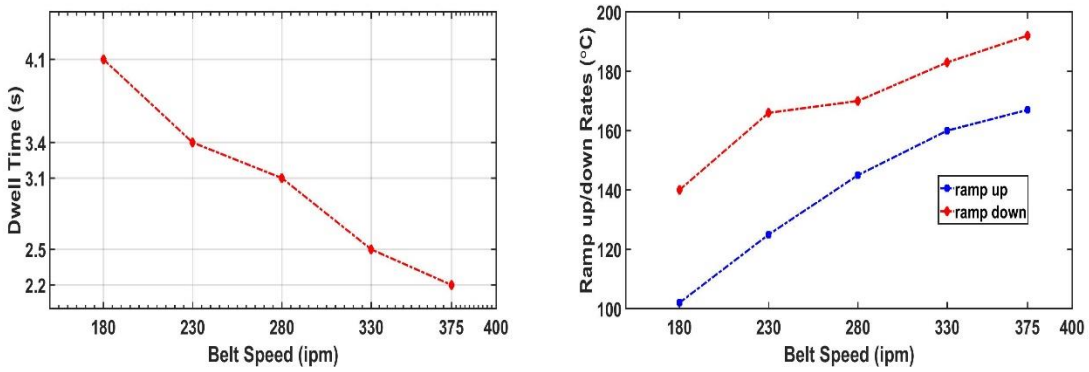

Figure 6.2: a) Dwell time (left) and b) Ramp up/down rates with increasing belt speeds (right)

Table 6.1: The Electrical Outputs of 5BB PERC (239 cm2) Silicon Solar Cells

Cell ID	V_{OC} (V)	Rsh (Ω-cm²)	Rs (Ω-cm²)	Rc (Ω-cm²)	FF (%)
230ipm-average	0.660	17600	0.683	0.0342	78.9
230ipm-Best	**0.662**	**15000**	**0.585**	**0.0262**	**79.9**
375ipm-average	0.664	10110	0.517	0.0225	80.6
375ipm-Best	**0.665**	**10200**	**0.217**	**0.0185**	**81.7**

Figure 6.3 compares the internal quantum efficiency (IQE) and the reflectance (grid and between gridlines combined) for two best cells fired with same peak temperature but different belt speeds at 375 and 230 ipm. The reflectance of both cells are very similar, which indicates uniform silicon nitride anti reflection

coating layer on both surfaces of the cell. As seen in Figure 6.3, there is also no significant difference between the two cells' IQE at short and long wavelengths. This suggests the short circuit current density (J_{SC}) is not affected by the belt speed. In fact, the J_{SC} are very similar to each other; 39.78 mA/cm² and 39.45 mA/cm², respectively for 230 ipm and 375 ipm.

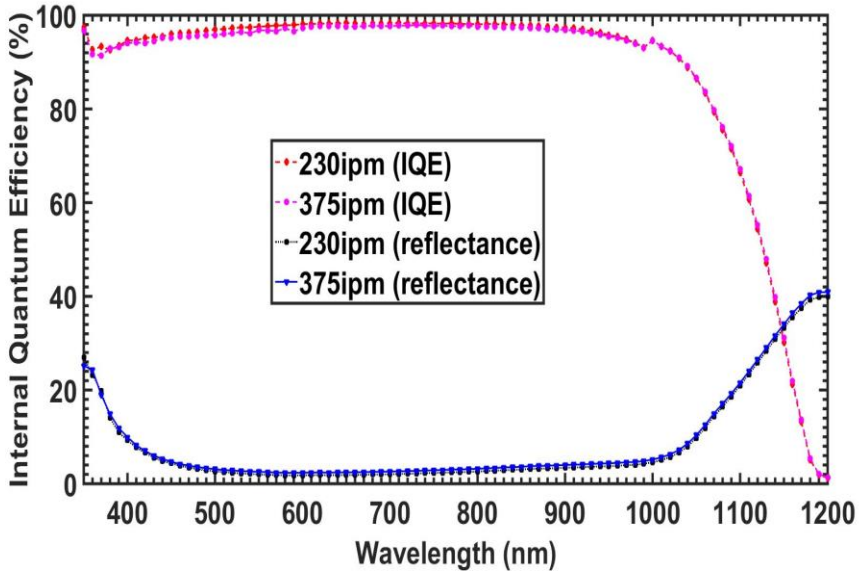

Figure 6.3: Internal quantum efficiency and reflectance measurements for high (375ipm) and low (230ipm) belt speed fired cells

Although the IQE for the two cells were identical, the V_{OC} for the 375 ipm belt speed fired cell was ~5 mV larger than the 230 ipm counterpart. In order to understand the origin of the increase in the V_{OC} of 375 ipm belt speed, microstructural analysis of back surface Al-BSF was carried out. Figure 6.4 shows the scanning electron microscope (SEM) images for the two cells that are fired with the belt speed of 230 and 375 ipm. From the SEM micrograph, the thickness of the local BSF layer was calculated as the average of 3 measurements. The average BSF

layer thickness of cells fired at 230 and 375 ipm are 0.6 µm and 1.03 µm, respectively. The cell fired at 375 ipm gave perfectly uniform and ~1 µm thick local BSF around the contact region compared to the 230 ipm counterpart in which the BSF is not uniform (not formed in some areas) and thin. This thickness and uniformity is in line with Chen et. al. [80], which recently showed that the V_{OC} is increasing as the local BSF thickness and uniformity for PERC cells and the V_{OC} after ~1 µm is less dependent on the local BSF thickness. Thus, a ~5 mV V_{OC} improvement in our work can be attributed to a thicker and more uniform local BSF layer formed in the cell fired at 375 ipm compared to 230 ipm.

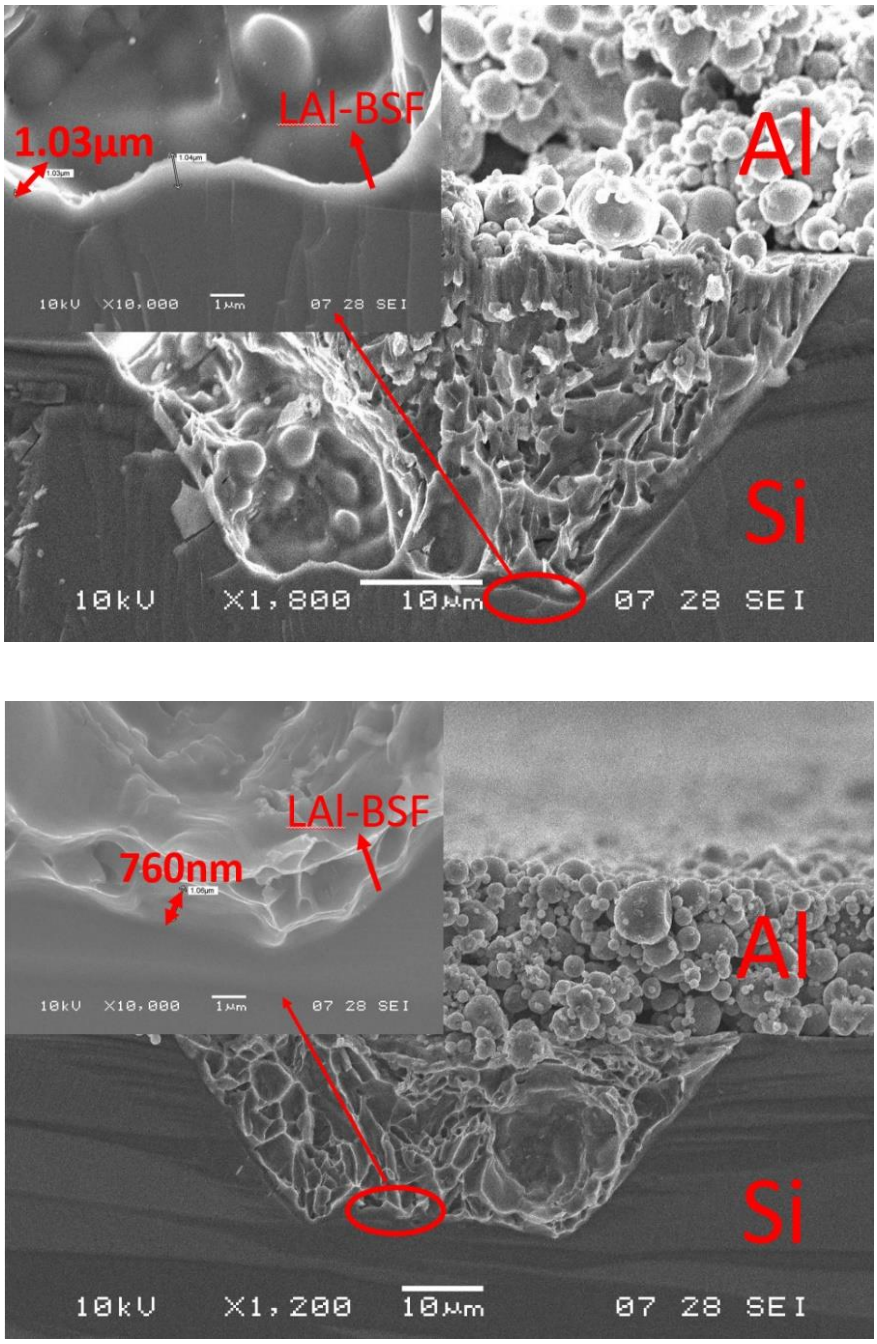

Figure 6.4: SEM images of back contact of PERC structured solar cells fired at 375 ipm (up) and 230 ipm (down) belt speeds

6.4 Conclusion

Rapid thermal processing is a key technology in the screen-printed Ag paste fire through dielectric to form excellent contacts to silicon solar cell. The ramp up

and ramp down rates are very critical in achieving the right contacts independent of the source of the paste. The ramp up/down rates are dependent on the belt speed of the furnace. The belt speed also determines the dwell time of the contact at the elevated temperature, which ranges from 750-800 ^{o}C. The faster the belt speed the shorter the dwell time, which enhances the contact quality. Although high belt speeds for contact co-firing are beneficial, due to the difficulties involved in reaching the peak firing temperature at high belt speeds, the commercial infrared (IR) belt furnaces are operated at belt speeds of between 180-200 inches per minute (ipm). Therefore, this paper reports on the development of very high belt speed for fire through dielectric Si solar cell with no additional equipment. By doubling the belt speed from 180 to 375 ipm, the open circuit voltage (V_{OC}) can be increased by ~5 mV along with ~1-2 % increase in fill factor without adding any cost to production.

CHAPTER 7 :
NEXT GENERATION COST EFFECTIVE METALLIZATION FOR SOLAR CELLS

7.1 Introduction

Screen printed Ag front contacts have dominated the solar cell market because of its simplicity and high throughput. However, the control on the gridline width of the contacts is still in the works. The paste composition with respect to viscosity and rheology, which controls the spreading and gridline continuity after dispensing is at its highest point in research. Thus, even though a typical screen printed gridline contacts in the industrial solar cell varies in width from 80 μm – 120 μm, it is certain that this will be reduced to 30-70 μm in the future. With the 80-120 μm wide gridlines, shading loss on the front surface, which decreases the J_{SC} and hence the overall efficiency, is high. Thus, the development of the non-contact technologies such as inkjet and aerosol printing, which gives precise gridline width and height, is in progress. Aerosol printing, among these emerging technologies, is used in this section to explore and exploit the benefits of:

i. finer gridlines via precise nozzle printing,
ii. lower production costs by eliminating the screen and narrowing the gridlines so that less metal paste is used per wafer, and
iii. ease of applicability by automating the process so that gridlines in the range of 30 μm - 70 μm can be achieved.

Similar to screen printing, aerosol printing process practices metal inks with formulation of metal particles, usually Ag, organic binders and metal oxide glass frit

followed by a high temperature annealing so that the glass frit etch through dielectric. Using silver in the gridlines is one of the factors what rises the overall cost to make a solar cell. Therefore alternative metals to Ag pastes such as copper (Cu) and nickel (Ni) have been investigated [81-84] in order to further decrease the cost of metallization on silicon solar cells. In this chapter, aerosol printing incorporated with different pastes is investigated to achieve gridlines composed of Ag, Cu and Ni in different height and widths as well as analysis of temperature sensitivity and reaction of the new metal pastes to high temperature annealing process.

7.2 Cell Fabrication

P-type Czochralski (Cz) mono and multi crystalline silicon with of 2 ohm-cm resistant wafers are used. The monocrystalline wafers are textured anisotropically with pyramid height of ~3-5 μm while the multicrystalline wafers are isotropically textured with ~2-3 μm pyramid heights. After cleaning the wafers, emitter formation is carried out with 85 ohm/sq. sheet resistance. This is followed by deposition of SiN_X antireflection coating before the printing of Al back contacts. For the front metallization, aerosol jet printing[6] is used. 89 gridline with 1.8 mm spacing is used based on 85 ohm/sq emitter sheet resistance so that the contact resistance is not adversely affected. Figure 7.1a shows a unit cell of 5 x 5 cm.

[6] Aerosol jet printing of the cells are performed by the National Renewable Energy Laboratory (NREL).

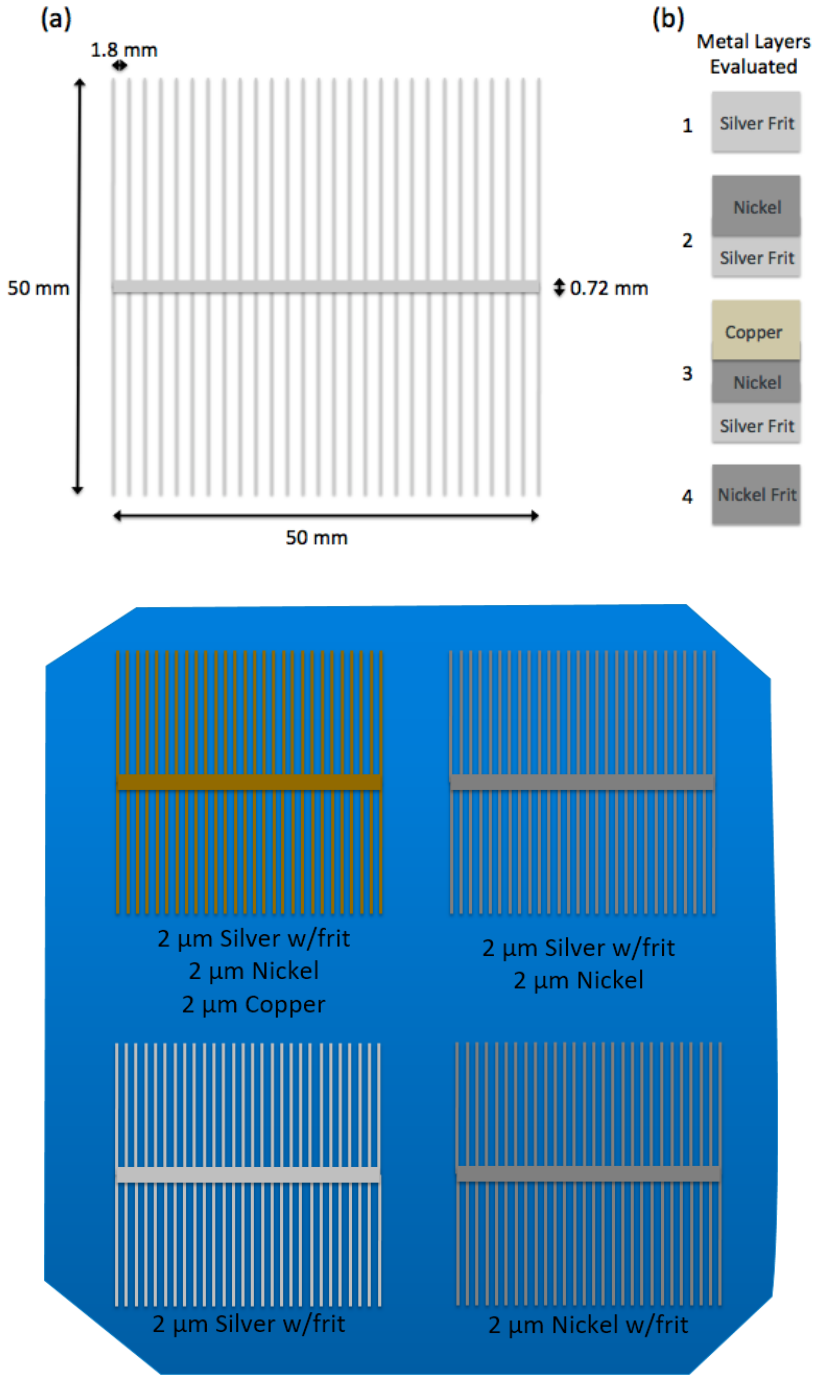

Figure 7.1: Printing pattern (a) with dimensions of the grids with central bus bar and (b) the four metal layers evaluated in this study

7.3 Ink Formulation

Metallic composition of

(i) Ag with glass frit,

(ii) Ag with glass frit and Ni,

(iii) Ag with glass frit and Ni and Cu and

(iv) Ni with glass frit are used (see Figure 7.1b) to

a. test the difference between Ag and Ni gridlines,

b. determine whether Ag can be replaced with Ni and

c. understand the barrier properties of Ni and Cu and finally

d. understand the difference in performance with layering metal stacks.

The Ag frit ink is composed of ethylene glycol and Ag trifluoroacetate (1:7 molar equivalent) with 5 wt. % lead-oxide (PbO) frit. Ni ink is a 1:2:5 molar equivalent of Ni formate, ethylene diamine, and ethylene glycol, respectively. PbO frit is then added at 5 wt.% to form a separate Ni frit ink. Similarly, a 1:2:5 molar equivalent of Cu formate, ethylene diamine, and ethylene glycol, respectively comprises the Cu ink. Ink is mixed by first adding ethylene glycol and then slowly mixing in ethylene diamine, mixing order is important since significant heat is produced.

An Optomec Aerosol Jet System with pneumatic atomization integrated onto an x-y vacuum stage in an inert atmosphere is used to print the metal inks. Using nitrogen, the ink is atomized into small droplets. The suspended droplets are

transported by means of gas flow to a virtual impactor where the velocity and average drop size is decreased using the impactor's geometry and exhaust stream. The refined aerosolized droplets travel to the nozzle and are surrounded by a nitrogen sheath that compresses the flow and directs it on to the substrate sitting 3-5 mm below the nozzle. Depending on the viscosity of the ink, the flow of nitrogen to the atomizer, from the exhaust, and to the sheath can be adjusted to produce features as small as 10 μm [85]. Table 7.1 summarizes the flow rates used for printing the metal inks. During printing, the temperature of the stage is set to 200 °C. In printing the metal layers, realignment is avoided by printing each metal immediately following the previous layer, without moving the printing nozzle nor substrate.

Table 7.1: Summary of aerosol printing factors to deposit the metal inks

Ink	Nozzle Diameter (μm)	Sheath (sccm)	Exhaust (sccm)	Atomizer (sccm)	Print Speed (mm/s)	Passes
Ag Frit	300	60	480	500	100	60
Ni Frit	300	60	520	550	100	60
Ni	300	60	480	500	100	60
Cu	300	60	480	500	100	60

It is important to note that the same firing conditions apply to the contacting schemes developed in this study. To this end, the TP Solar infra-red lamp rapid thermal processing (RTP) belt furnace with variable belt speed from 100-500 inches

per minute (ipm) is used. The ramp rates are critical to obtaining low contact resistance, which can influence the FF. The ramp up and ramp down rates of >100 ^{o}C/s is used in the contact firing of the cell with peak temperature of between 770-800^{o}C.

Suns-V_{OC} measurements is carried out to check the V_{OC}, ideality factor (n-factor), J_{o2}, pseudo FF (pFF) and pseudo efficiency for each metallization scheme. The wafers are imaged using a Nova scanning electron microscope (SEM) with integrated energy-dispersive X-ray (EDX) spectroscopy[7]. Top down and cross-sectional images of each sample are measured and analyzed.

7.4 Results and Discussion

The aerosol jet printing system in conjunction with the inks used in this work is specifically set up for making features roughly on the order of 30μm wide by 50nm height per pass. To keep the R_S low, at least 5 μm is required. However, this adds up to 100 passes in the aerosol printing system. Instead, the printed contacts are formed with 60 passes results in ~3 μm height so that the printing is optimized and to be consistent. By modifying the nozzle (printing head) and atomization of the system, the number of passes (or layers) can be reduced to 1 or 2 so that the throughput of the process is increased.

SEM and EDX images are taken of the printed contacts from the top and at the cross section before and after firing to observe how the layers behave closely, see

[7] SEM and EDX analyses are performed by NREL.

Figure 7.2. A clear separation between the printed metals, with the copper on top of the barrier layers of Ag frit and Ni, is observed. The average width of the gridlines before firing is determined to be between 100 and 165 μm and height of ~3 μm, depending on the metal stack printed. The variations observed are due to differences in wetting and concentrations, making the inks print slightly different widths and height. Table 7.2 presents the average widths before and after firing.

Table 7.2: Average Printing widths for each metal stack before and after firing

Average Print	Before Firing width (μm)	After Firing width (μm)
Ag Frit / Ni / Cu	165	108
Ag Frit / Ni	110	80
Ag Frit	100	83
Ni Frit	145	67

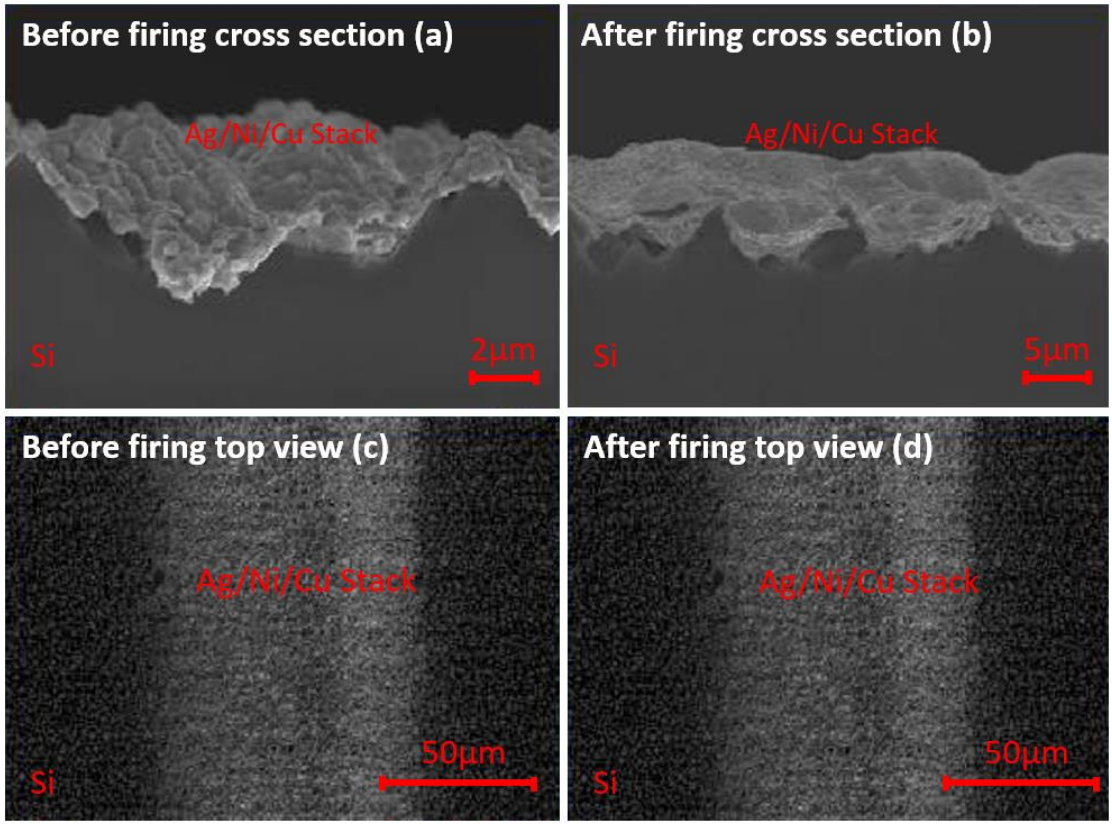
Before firing cross section (a)
Ag/Ni/Cu Stack
Si
2µm
After firing cross section (b)
Ag/Ni/Cu Stack
Si
5µm
Before firing top view (c)
Ag/Ni/Cu Stack
Si
50µm
After firing top view (d)
Ag/Ni/Cu Stack
Si
50µm

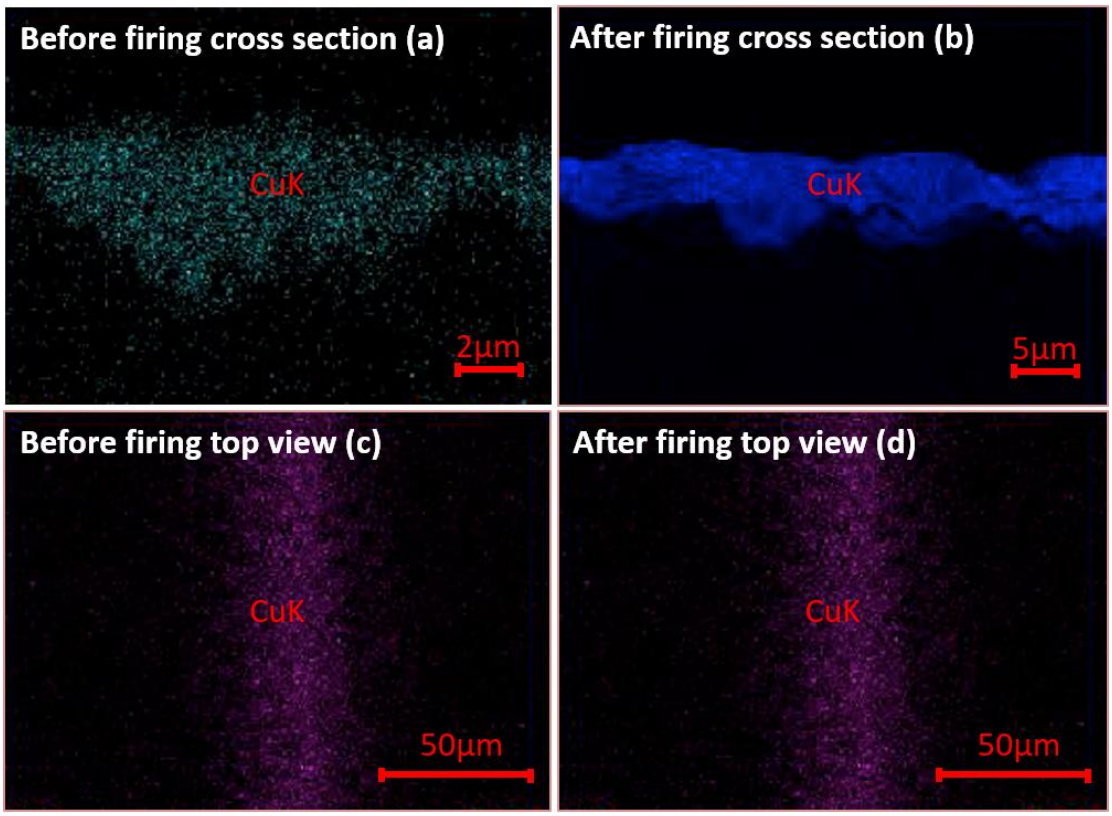
Before firing cross section (a)
CuK
2µm
After firing cross section (b)
CuK
5µm
Before firing top view (c)
CuK
50µm
After firing top view (d)
CuK
50µm

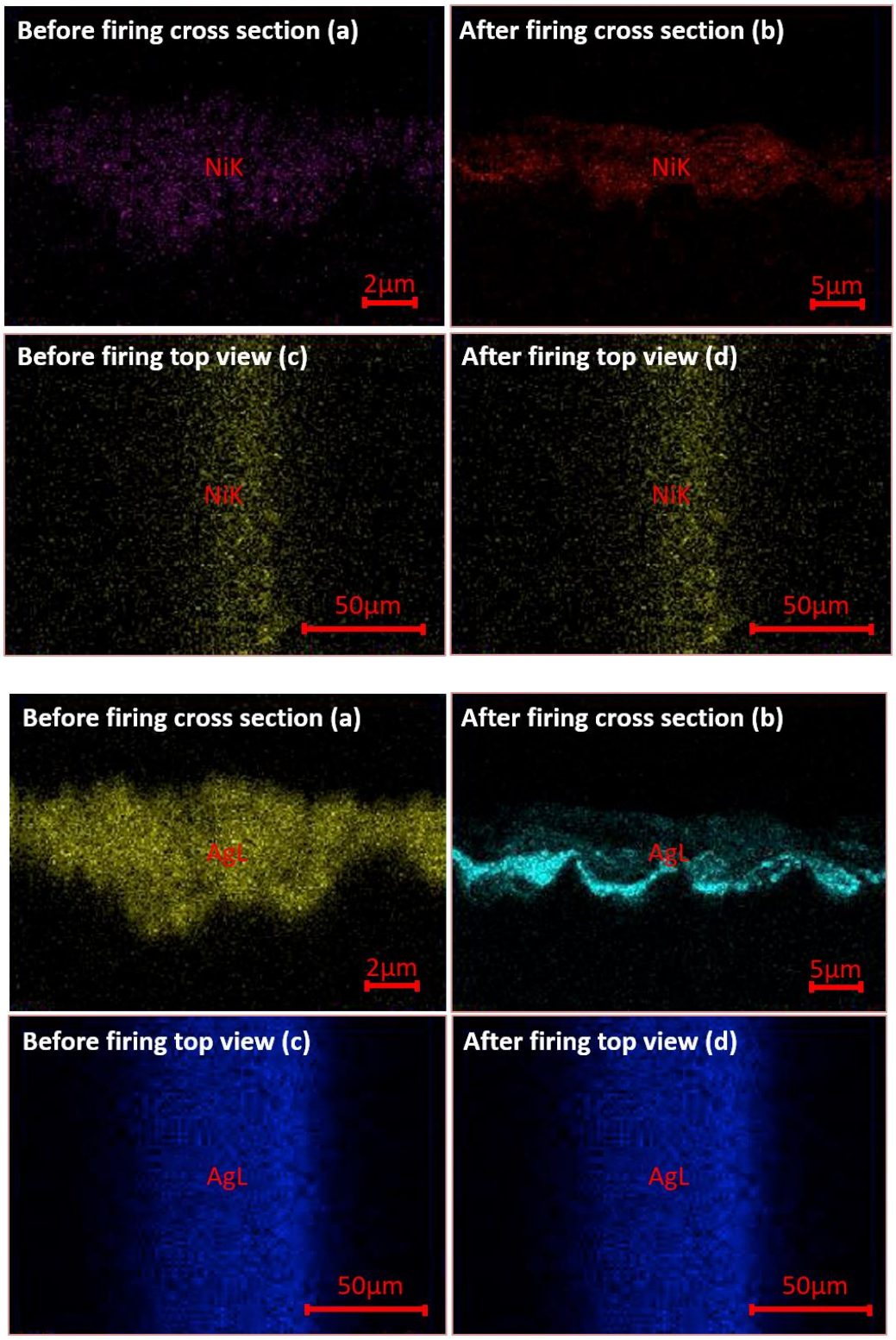

Figure 7.2: SEM and EDX of Ag Frit/Ni/Cu metal stack of (a) the cross-section before firing (b) cross section after firing (c) top view before firing and (d) top view after firing.

After firing the average width of the gridlines is observed to remain between 67 and 108µm while the average height decreases to 2µm (see Table 7.2 and Figure 7.2 c / d). This suggests that during the firing process the deposited gridlines sinters and compacts into a continuous line. From Figure 7.2 c and d, the metal layers retain their separation from one another during the firing process. Cu is shown not to have migrated into the silicon. From Figure 7.2 c, there is a clear distinction of the middle Ni layer. This can also be seen in Figure 7.2 d, where issues with different metal melting temperatures can be seen in the form of delamination of Ni on top of a Ag frit and additional delamination of the copper on top of the Ni.

In Figure 7.3 a and b, the pseudo efficiency (pFF), series resistance (R_S), and temperature are plotted against gridline width and height. Detrimental effects from firing is observed as delamination. Figure 7.3 c clearly shows an area where the contact stack detaches from the silicon in the middle of the gridline, but remains attached on the edges, creating a void underneath it. Interlayer delamination is where the metals solidifying at different temperatures. This delamination is only observed for temperatures exceeding 790 °C. For those temperatures, the differences in thermal expansion coefficients causes stress between the silicon and silver or between the metal layers, resulting in lift off and interlayer delamination, respectively. After excluding samples with significant delamination, an average pFF of over 80% is consistently measured. In addition, a general trend of increasing firing temperature results in increased gridline widths. The R_S for all metal stacks is measured in the range of 0.55 and 0.8 ohm·cm^2. A summary of the average cell for

each metal stack is shown in Table 7.3. The champion cell is recorded from the Ag Frit/Ni/Cu stack with the V_{OC} of 644 mV, the pFF of 84%, pseudo efficiency of 19.9% and the R_S of 0.6 ohm·cm^2.

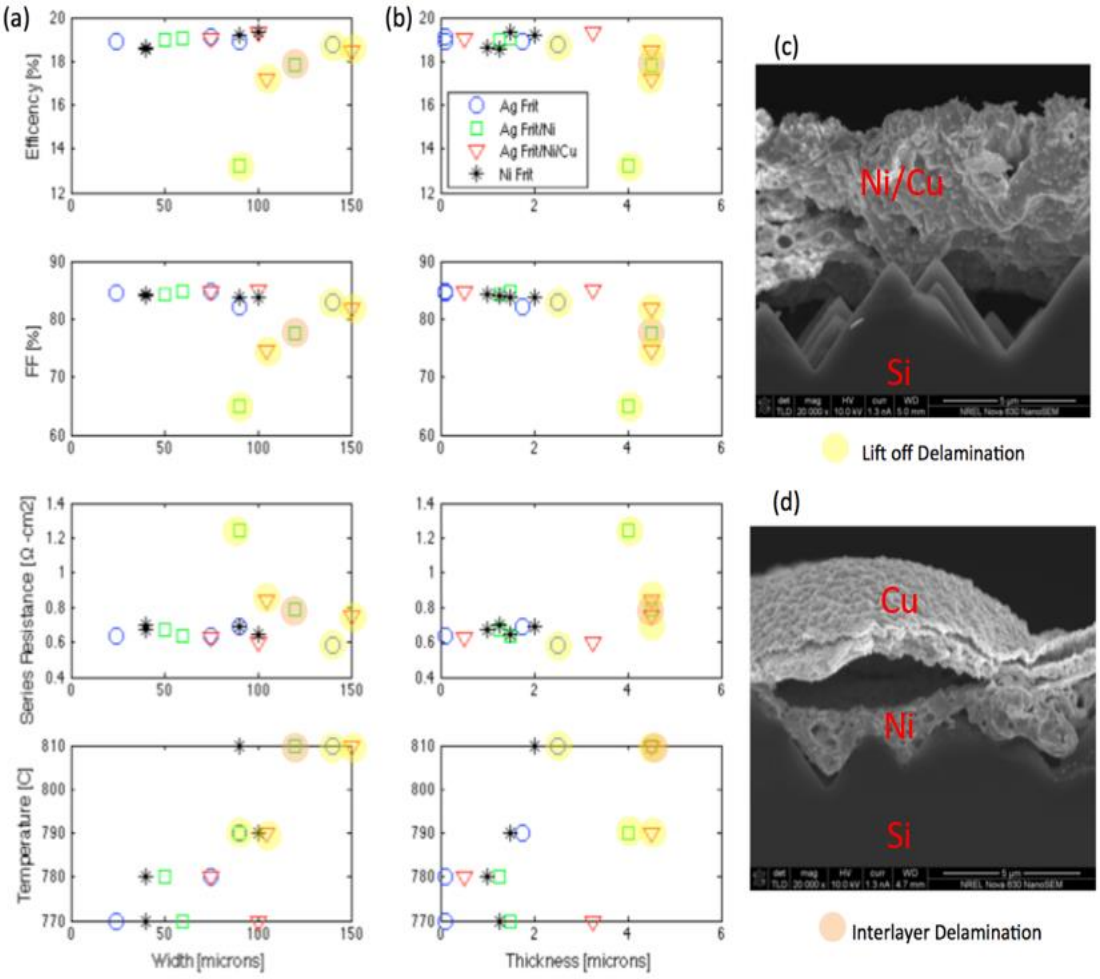

Figure 7.3: Efficiency, FF, series resistance, and temperature plotted against gridline (a) width and (b) height with denoted data points and SEM images of (c) lift off and (d) delamination.

Table 7.3: The average value of electric output parameters of the cells

Metal Stack	V_{OC} (mV)	pFF (%)	Efficiency (%)	Rs (ohm·cm²)	Temperature (°C)
Ag Frit	609	84.6	18.9	0.64	770
Ag Frit / Ni	613	79.4	17.9	0.77	785
Ag Frit / Ni / Cu	616	81.8	18.5	0.75	810
Ni Frit	602	83.9	18.5	0.69	770

Figure 7.4a compares electrical output parameters of the single layer metal contacts, Ag Frit and Ni Frit, the performance of the cells are nearly identical for each firing temperatures evaluated. Additionally, delamination is not observed in any of the Ni Frit gridlines, as seen in Figure 7.4 b and c. The Ni Frit shows greater adhesion to the substrate, where, after testing, the Ag Frit would easily flake off when the surface is touched. This is in line with studies done using plated nickel, where the formation of nickel silicide is hypothesized to act as an adhesion promoter [86]. It can also be stated that while Ag silicide produces similar adhesion promoters, the lift off delamination only occurs for temperatures above 790 °C. This suggests that the Ni has a larger processing window because it exhibits lower coefficient of thermal expansion over the peak temperature range of 770 – 810 °C.

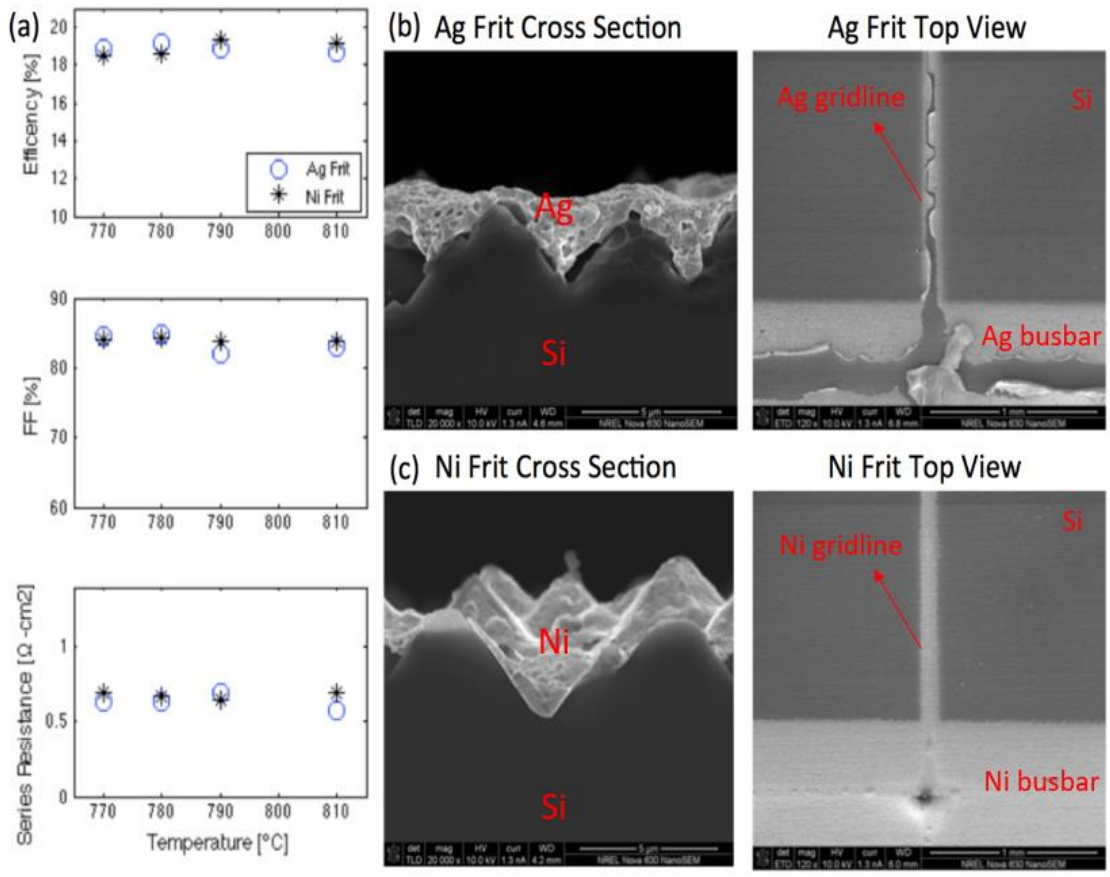

Figure 7.4: (a) Efficiency, the FF, and the R_S vs peak firing temperatures for silver frit and nickel frit single metal top contacts with corresponding SEM images of the cross section and top view for (b) silver frit and (c) nickel frit

The best cell from the Ni Frit stack is 623 mV of the V_{OC}, 84% of the pFF, 19.4% of efficiency, and the R_S of 0.6 Ω-cm². This performance is one of the top-performing cells in its group. With Ni being at a fraction of the cost of Ag, these results are favorable to move towards using all Ni metal contacts. Furthermore, the Ni barrier properties provide a means of multi-layer metal stacks without the use of Ag. Extensive studies have been conducted on electroplating Ni / Cu top contacts [82]; however, fully printed Ni / Cu has not been demonstrated. Combining this with

the increased adhesion over Ag Frit, this study provides insight into using Ni Frit ink as a replacement for Ag inks for printed technologies.

7.5 Cost Comparison of Alternative Metallization

From the preliminary results of the alternative metallization investigation, Ni glass showed better adhesion than the Ag counterpart. This suggests that Ni/Cu metallization alternative will be far more cost effective than Ag contacts, which has been the dominant metallization for the solar cell industry. From solar cell manufacturing cost analysis, Ag is the second most expensive material after Si wafer. Therefore, by replacing Ag with cost-effective alternatives such as Ni/Cu will be beneficial from the cost viewpoint.

The gridlines printed with aerosol jet printing using Ni and Cu have exhibited high potential in performance of the cells. Utilizing the proposed ink formulation after being optimized will lead to cost reduction. Kumar showed that [23] around 35% of the total cost of PERC structured cell processing is for Ag printing. Therefore, Figure 7.5 compares the cost percentage breakdown of Ag printed and Ni/Cu contacted cells with respect to individual processing steps. The cost of metallization dropped from 35% of total processing cost to only 5-6%. It is important to note that this also leads to approximately drop of 30% in the total cost of processing by switching from Ag to Ni/Cu.

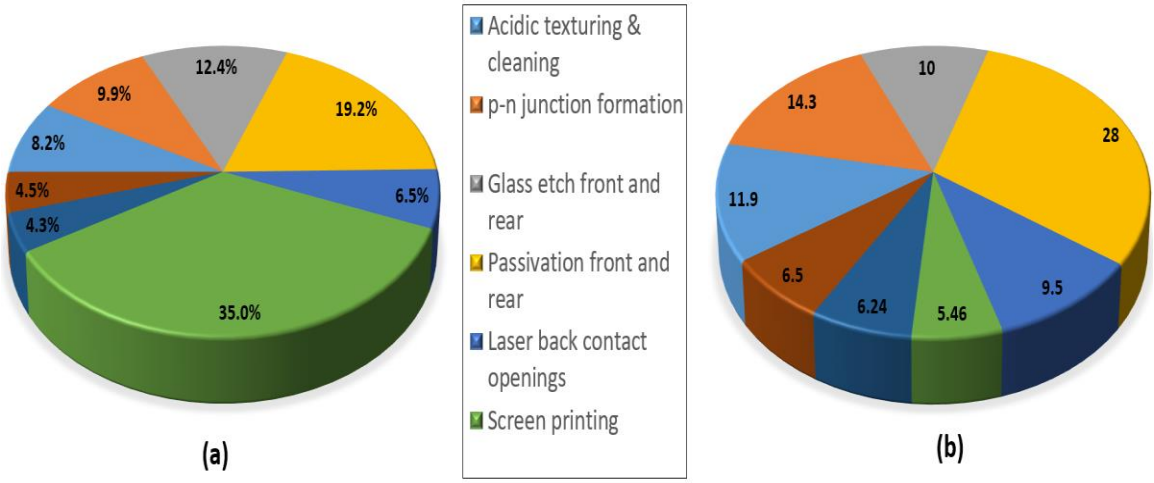

Figure 7.5: PERC structure cell processing cost percentage breakdown with respect to individual steps for (a) silver printed and (b) Ni printed contacts.

7.6 Conclusion

The front surface metallization of silicon solar cells by fully aerosol jet printing is a promising alternative to screen printing. It provides low cost, high throughput manufacturing step. It is demonstrated by using aerosol printing that the gridlines of Ag Frit, Ni Frit, Ag Frit / Ni and Ag Frit / Ni / Cu have the pseudo efficiency of ~18% and the pseudo fill factor of above 80%. The best result obtained with the Ag Frit/Ni/Cu stack, shows 19% pseudo efficiency and the pFF of 85% having gridline widths of ~100 µm and a height of ~3.25 µm. SEM and EDX images of gridlines shows that metal mixing within the stack and diffusion into the silicon are not observed. By comparing the Ni Frit and Ag counterpart, it is evident that there is a slight dependency on peak firing temperatures and performance between the two metals. More so, the adhesion of Ni Frit to silicon is better than Ag counterpart to silicon. Also, from the cost analysis comparison, it is obvious that a

30% reduction in manufacturing is achievable. This study provides analysis into using Ni Frit ink as a replacement for Ag inks for printed technologies, which will certainly lead to the ultimate goal of 3¢/kWh LCOE from photovoltaics.

BIBLIOGRAPHY

[1] U. N. D. Program, "Human Development Report Work for Human Development," 2015.

[2] U. S. E. I. Administration, "International Energy Outlook 2017," 2017.

[3] H. C. Q. E. X. G. J. H. J. M. E. M. S. P. J. R. A. S. J. S. A. Sokolov, "Food Water Energy Climate Outlook," *MIT Joint Program on the Science and Policy of Global Change,* 2016.

[4] R. K. Pachauri *et al.*, *Climate change 2014: synthesis report. Contribution of Working Groups I, II and III to the fifth assessment report of the Intergovernmental Panel on Climate Change*. IPCC, 2014.

[5] J. Hansen, R. Ruedy, M. Sato, and K. Lo, "Global surface temperature change," *Reviews of Geophysics,* vol. 48, no. 4, 2010.

[6] U. D. o. Energy, "Basic Needs for Energy Utilization," Report 2015.

[7] M. Becquerel, "Mémoire sur les effets électriques produits sous l'influence des rayons solaires," *Comptes rendus hebdomadaires des séances de l'Académie des Sciences,* vol. 9, pp. 561-567, 1839.

[8] W. G. Adams and R. Day, "V. The action of light on selenium," *Proceedings of the Royal Society of London,* vol. 25, no. 171-178, pp. 113-117, 1877.

[9] D. M. Chapin, C. Fuller, and G. Pearson, "A new silicon p-n junction photocell for converting solar radiation into electrical power," *Journal of Applied Physics,* vol. 25, no. 5, pp. 676-677, 1954.

[10] E. P. I. A. (EPIA), "Global Market Outlook for Photovoltaics 2016-2020," 2017.

[11] I. Fraunhofer Institute for Solar Energy Systems, "Photovoltaics report," 2018.

[12] "International Technology Roadmap for Photovoltaic (ITRPV) 8th Edition Report," 2017.

[13] K. H. Kim *et al.*, "Record high efficiency of screen-printed silicon aluminum back surface field solar cell: 20.29%," *Japanese Journal of Applied Physics,* vol. 56, no. 8S2, p. 08MB25, 2017.

[14] W. Deng *et al.*, "22.61% Efficient fully Screen Printed PERC Solar Cell," *Proc. 44th IEEE PVSC,* 2017.

[15] F. Ye *et al.*, "22.13% efficient industrial p-type mono PERC solar cell," in *Photovoltaic Specialists Conference (PVSC), 2016 IEEE 43rd*, 2016, pp. 3360-3365: IEEE.

[16] B. Min *et al.*, "A Roadmap Toward 24% Efficient PERC Solar Cells in Industrial Mass Production," *IEEE Journal of Photovoltaics,* vol. 7, no. 6, pp. 1541-1550, 2017.

[17] P. Campbell and M. A. Green, "The limiting efficiency of silicon solar cells under concentrated sunlight," *IEEE Transactions on Electron Devices,* vol. 33, no. 2, pp. 234-239, 1986.

[18] T. Tiedje, E. Yablonovitch, G. D. Cody, and B. G. Brooks, "Limiting efficiency of silicon solar cells," *IEEE Transactions on electron devices,* vol. 31, no. 5, pp. 711-716, 1984.

[19] A. Wang, J. Zhao, and M. Green, "24% efficient silicon solar cells," *Applied physics letters,* vol. 57, no. 6, pp. 602-604, 1990.
[20] C. Breyer and A. Gerlach, "Global overview on grid-parity," *Progress in photovoltaics: Research and Applications,* vol. 21, no. 1, pp. 121-136, 2013.
[21] B. Elliston, I. MacGill, and M. Diesendorf, "Grid parity: A potentially misleading concept?," in *Proc. Solar*, 2010, pp. 1-11.
[22] U. S. E. I. Administration, "Levelized Cost and Levelized Avoided Cost of New Generation Resources in the Annual Energy Outlook 2018," 2018.
[23] A. Kumar, M. Bieri, T. Reindl, and A. G. Aberle, "Economic Viability Analysis of Silicon Solar Cell Manufacturing: Al-BSF versus PERC," *Energy Procedia,* vol. 130, pp. 43-49, 2017.
[24] S. M. Sze and K. K. Ng, *Metal-semiconductor contacts*. Wiley Online Library, 2006.
[25] E. H. Rhoderick, "Metal-semiconductor contacts," *IEE Proceedings I-Solid-State and Electron Devices,* vol. 129, no. 1, p. 1, 1982.
[26] H. B. Michaelson, "Work functions of the elements," *Journal of Applied Physics,* vol. 21, no. 6, pp. 536-540, 1950.
[27] E. Jabari and E. Toyserkani, "Micro-scale aerosol-jet printing of graphene interconnects," *Carbon,* vol. 91, pp. 321-329, 2015.
[28] A. Mette, P. Richter, M. Hörteis, and S. Glunz, "Metal aerosol jet printing for solar cell metallization," *Progress in Photovoltaics: Research and Applications,* vol. 15, no. 7, pp. 621-627, 2007.
[29] T. Kaydanova, A. Miedaner, C. Curtis, J. Perkins, J. Alleman, and D. Ginley, "Ink jet printing approaches to solar cell contacts," National Renewable Energy Laboratory (NREL), Golden, CO.2003.
[30] K. Teng and R. W. Vest, "Metallization of solar cells with ink jet printing and silver metallo-organic inks," *IEEE Transactions on components, hybrids, and Manufacturing Technology,* vol. 11, no. 3, pp. 291-297, 1988.
[31] M. Beutel *et al.*, "Fine line metallization by coextrusion technology for next generation solar cells," *Solar Energy Materials and Solar Cells,* vol. 131, pp. 64-71, 2014.
[32] J. Hoornstra, S. Roberts, H. De Moor, and T. Bruton, "First experiences with double layer stencil printing for low cost production solar cells," *2nd World PVSEC,* pp. 1527-1530, 1998.
[33] H. de Moor, A. Weeber, J. Hoornstra, and W. Sinke, "Fine-line screen printing for silicon solar cells," in *Snowmass Conference Colorado, 6th Workshop on the Role of Impurities and Defects in Silicon Device Processing, Snowmass Co*, 1996, pp. 154-170.
[34] V. Shanmugam *et al.*, "Analysis of fine-line screen and stencil-printed metal contacts for silicon wafer solar cells," *IEEE Journal of Photovoltaics,* vol. 5, no. 2, pp. 525-533, 2015.
[35] H. Hannebauer, T. Dullweber, T. Falcon, X. Chen, and R. Brendel, "Record low Ag paste consumption of 67.7 mg with dual print," *Energy Procedia,* vol. 43, pp. 66-71, 2013.

[36] E. Ralph, "Recent advancements in low cost solar cell processing," in *11th Photovoltaic Specialists Conference*, 1975, p. 315.
[37] A. Haigh, "Fired through printed contacts on antireflection coated silicon terrestrial solar cells," in *12th Photovoltaic Specialists Conference*, 1976, p. 360.
[38] N. Chen, A. Chowdury, E. Ahmad, V. Unsur, and A. Ebong, "Assessing the impact of multi-busbars on metallization cost and efficiency of solar cells with digital inkjet-printed gridlines," in *High Capacity Optical Networks and Enabling Technologies (HONET-CNS), 2013 10th International Conference on*, 2013, pp. 60-65: IEEE.
[39] A. Ebong, N. Chen, V. Unsur, A. Chowdhury, and B. Damiani, "Innovative front grid design, four-streets and five-busbars (4S-5BB), for high efficiency industrial Al-BSF silicon solar cell," *IEEE Electron Device Letters,* vol. 37, no. 4, pp. 459-462, 2016.
[40] J. Wong, "Griddler: Intelligent computer aided design of complex solar cell metallization patterns," in *Photovoltaic Specialists Conference (PVSC), 2013 IEEE 39th*, 2013, pp. 0933-0938: IEEE.
[41] M. A. Green, "Solar cells: operating principles, technology, and system applications," 1982.
[42] L. Caballero, P. Sanchez-Friera, B. Lalaguna, J. Alonso, and M. Vazquez, "Series resistance modelling of industrial screen-printed monocrystalline silicon solar cells and modules including the effect of spot soldering," in *Photovoltaic Energy Conversion, Conference Record of the 2006 IEEE 4th World Conference on*, 2006, vol. 2, pp. 1388-1391: IEEE.
[43] D. L. Meier and D. K. Schroder, "Contact resistance: Its measurement and relative importance to power loss in a solar cell," *IEEE transactions on electron devices,* vol. 31, no. 5, pp. 647-653, 1984.
[44] N. Chen, "Understanding and development of cost-effective industrial aluminum back surface field (Al-BSF) silicon solar cells," The University of North Carolina at Charlotte, 2015.
[45] D. Meier *et al.*, "Determining components of series resistance from measurements on a finished cell," in *Photovoltaic Energy Conversion, Conference Record of the 2006 IEEE 4th World Conference on*, 2006, vol. 2, pp. 1315-1318: IEEE.
[46] D. L. Meier, V. Chandrasekaran, A. Gupta, V. Yelundur, and A. Rohatgi, "Silver contact grid: inferred contact resistivity and cost minimization in 19% silicon solar cells," *IEEE journal of Photovoltaics,* vol. 3, no. 1, pp. 199-205, 2013.
[47] L. Jiang, W. Zhang, T. Guo, D. Kapp, L. Yan, and L. Wang, "An improved mathematical modeling to simulate metallization screen pattern trend for silicon solar cell," in *Photovoltaic Specialists Conference (PVSC), 2013 IEEE 39th*, 2013, pp. 2641-2645: IEEE.
[48] A. Fallisch and D. Biro, "2-D SPICE simulation and analytical calculation of spreading resistance effects in emitter wrap-through cells with nonsquare via-hole pattern," *IEEE Journal of Photovoltaics,* vol. 1, no. 2, pp. 153-158, 2011.

[49] V. Unsur, A. Chowdhury, N. Chen, and A. Ebong, "The effects of nano Ag particles on gridline sintering for silicon solar cells," in *Photovoltaic Specialist Conference (PVSC), 2015 IEEE 42nd*, 2015, pp. 1-5: IEEE.
[50] V. Unsur, "Understanding the Solar Cell Contact Formation by Digital Inkjet Printing Technique," University of North Carolina at Charlotte, 2013.
[51] T. A. Nguty and N. N. Ekere, "The rheological properties of solder and solar pastes and the effect on stencil printing," *Rheologica Acta,* vol. 39, no. 6, pp. 607-612, 2000.
[52] S.-J. L. Kang, *Sintering: densification, grain growth and microstructure*. Butterworth-Heinemann, 2004.
[53] R. C. Tolman, *Relativity, thermodynamics, and cosmology*. Courier Corporation, 1987.
[54] G. Schubert, "Thick film metallisation of crystalline silicon solar cells: Mechanisms, models and applications," 2006.
[55] J. Frenkel, "Viscous flow of crystalline bodies under the action of surface tension," *J. Phys.(USS R),* vol. 9, no. 5, p. 385, 1945.
[56] F. Nichols and W. Mullins, "Morphological changes of a surface of revolution due to capillarity-induced surface diffusion," *Journal of Applied Physics,* vol. 36, no. 6, pp. 1826-1835, 1965.
[57] D. L. Johnson, "New Method of Obtaining Volume, Grain-Boundary, and Surface Diffusion Coefficients from Sintering Data," *Journal of Applied Physics,* vol. 40, no. 1, pp. 192-200, 1969.
[58] W. Koch and S. Friedlander, "The effect of particle coalescence on the surface area of a coagulating aerosol," *Journal of Colloid and Interface Science,* vol. 140, no. 2, pp. 419-427, 1990.
[59] S. K. Friedlander and M. K. Wu, "Linear rate law for the decay of the excess surface area of a coalescing solid particle," *Physical Review B,* vol. 49, no. 5, p. 3622, 1994.
[60] W. Zhang and I. Gladwell, "Sintering of two particles by surface and grain boundary diffusion–a three-dimensional model and a numerical study," *Computational materials science,* vol. 12, no. 2, pp. 84-104, 1998.
[61] K.-K. Hong, S.-B. Cho, J. S. You, J.-W. Jeong, S.-M. Bea, and J.-Y. Huh, "Mechanism for the formation of Ag crystallites in the Ag thick-film contacts of crystalline Si solar cells," *Solar Energy Materials and Solar Cells,* vol. 93, no. 6-7, pp. 898-904, 2009.
[62] K.-K. Hong, S.-B. Cho, J.-Y. Huh, H. J. Park, and J.-W. Jeong, "Role of PbO-based glass frit in Ag thick-film contact formation for crystalline Si solar cells," *Metals and Materials International,* vol. 15, no. 2, pp. 307-312, 2009.
[63] M. M. Hilali *et al.*, "Effect of Ag particle size in thick-film Ag paste on the electrical and physical properties of screen printed contacts and silicon solar cells," *Journal of the Electrochemical Society,* vol. 153, no. 1, pp. A5-A11, 2006.
[64] M. K. Kang, Y. S. Yoo, D. Y. Kim, and N. M. Hwang, "Growth of $BaTiO_3$ Seed Grains by the Twin-Plane Reentrant Edge Mechanism," *Journal of the American Ceramic Society,* vol. 83, no. 2, pp. 385-390, 2000.

[65] I. B. Cooper, A. Ebong, J. S. Renshaw, R. Reedy, M. Al-Jassim, and A. Rohatgi, "Understanding and use of IR belt furnace for rapid thermal firing of screen-printed contacts to Si solar cells," *IEEE Electron Device Letters,* vol. 31, no. 5, pp. 461-463, 2010.

[66] V. Meemongkolkiat, M. Hilali, and A. Rohatgi, "Investigation of RTP and belt fired screen printed Al-BSF on textured and planar back surfaces of silicon solar cells," in *Photovoltaic Energy Conversion, 2003. Proceedings of 3rd World Conference on*, 2003, vol. 2, pp. 1467-1470: IEEE.

[67] A. Rohatgi, D. Kim, K. Nakayashiki, V. Yelundur, and B. Rounsaville, "High-efficiency solar cells on edge-defined film-fed grown (18.2%) and string ribbon (17.8%) silicon by rapid thermal processing," *Applied physics letters,* vol. 84, no. 1, pp. 145-147, 2004.

[68] A. Upadhyaya, V. Yelundur, and A. Rohatgi, "High efficiency mono-crystalline solar cells with simple manufacturable technology," 2006: Georgia Institute of Technology.

[69] A. Ebong, N. Chen, A. Chowdhury, and V. Unsur, "The impact of rapid thermal processing (RTP) on crystalline silicon solar cell performance and light induced degradation (LID)," in *Photovoltaic Specialist Conference (PVSC), 2015 IEEE 42nd*, 2015, pp. 1-4: IEEE.

[70] A. Ebong, M. Hillali, and A. Rohatgi, "Rapid photo-assisted forming gas anneal (FGA) for high quality screen-printed contacts for silicon solar cells," in *Photovoltaic Specialists Conference, 2000. Conference Record of the Twenty-Eighth IEEE*, 2000, pp. 264-267: IEEE.

[71] A. Rohatgi, S. Narasimha, A. U. Ebong, and P. Doshi, "Understanding and implementation of rapid thermal technologies for high-efficiency silicon solar cells," *IEEE Transactions on Electron Devices,* vol. 46, no. 10, pp. 1970-1977, 1999.

[72] S. Narasimha, A. Rohatgi, and A. Weeber, "An optimized rapid aluminum back surface field technique for silicon solar cells," *IEEE Transactions on Electron Devices,* vol. 46, no. 7, pp. 1363-1370, 1999.

[73] M. Rauer, C. Schmiga, J. Krause, R. Woehl, M. Hermle, and S. W. Glunz, "Further analysis of aluminum alloying for the formation of p+ regions in silicon solar cells," *Energy Procedia,* vol. 8, pp. 200-206, 2011.

[74] V. Mehta, B. Sopori, R. Reedy, B. To, H. Moutinho, and N. M. Ravindra, "Screen-Printed Al Back Contacts on Si Solar Cells: Issues and Some Solutions," *MRS Online Proceedings Library Archive,* vol. 1210, 2009.

[75] V. Meemongkolkiat, K. Nakayashiki, D. S. Kim, R. Kopecek, and A. Rohatgi, "Factors limiting the formation of uniform and thick aluminum–back-surface field and its potential," *Journal of the Electrochemical Society,* vol. 153, no. 1, pp. G53-G58, 2006.

[76] W. Shockley and W. Read Jr, "Statistics of the recombinations of holes and electrons," *Physical review,* vol. 87, no. 5, p. 835, 1952.

[77] J. A. Amick, F. J. Bottari, and J. I. Hanoka, "The effect of aluminum thickness on solar cell performance," *Journal of the Electrochemical Society,* vol. 141, no. 6, pp. 1577-1585, 1994.
[78] J. Krause, R. Woehl, M. Rauer, C. Schmiga, J. Wilde, and D. Biro, "Microstructural and electrical properties of different-sized aluminum-alloyed contacts and their layer system on silicon surfaces," *Solar Energy Materials and Solar Cells,* vol. 95, no. 8, pp. 2151-2160, 2011.
[79] J. Del Alamo, J. Eguren, and A. Luque, "Operating limits of Al-alloyed high-low junctions for BSF solar cells," *Solid-State Electronics,* vol. 24, no. 5, pp. 415-420, 1981.
[80] D. Chen *et al.*, "Analysis of morphologies and distribution of Al-doped local back surface field for screen printed i-PERC solar cells," *Proc. 27th EUPVSEC, Frankfurt,* pp. 1303-6, 2012.
[81] J. D. Fields *et al.*, "The formation mechanism for printed silver-contacts for silicon solar cells," *Nature communications,* vol. 7, p. 11143, 2016.
[82] A. ur Rehman and S. H. Lee, "Crystalline silicon solar cells with nickel/copper contacts," in *Solar Cells-New Approaches and Reviews*: InTech, 2015.
[83] S. G. Kang *et al.*, "Nano-glass frit for inkjet printed front side metallization of silicon solar cells prepared by sol–gel process," *physica status solidi (RRL)-Rapid Research Letters,* vol. 9, no. 5, pp. 293-296, 2015.
[84] C. Curtis, M. van Hest, A. Miedaner, T. Kaydanova, L. Smith, and D. Ginley, "Multi-layer inkjet printed contacts to Si," National Renewable Energy Laboratory (NREL), Golden, CO.2005.
[85] S. Binder, C. Schmiga, M. Glatthaar, and S. W. Glunz, "Optimized aerosol jet printed silver contacts on lowly doped phosphorus and boron emitters."
[86] A. Mondon, M. Jawaid, J. Bartsch, M. Glatthaar, and S. Glunz, "Microstructure analysis of the interface situation and adhesion of thermally formed nickel silicide for plated nickel–copper contacts on silicon solar cells," *Solar energy materials and solar cells,* vol. 117, pp. 209-213, 2013.

PUBLICATIONS

[1] M. Kim, S. Wenham, V. Unsur, A. Ebong and B. Hallam, "Impact of Rapid Thermal Process to Meta Stable Defects: Preformation of the LeTID and Suppression of B-O Defects", *World Conference on Photovoltaic Energy Conversion (WCPEC-7)*, 2018.

[2] K. Ren, V. Unsur, A. Chowdhury, Y. Zhang, and A. Ebong, "The Impact of Tellurite Glass on Contact Resistance of the Fire through Dilectric (FTD) c-Si Solar Cell with Lightly Doped Emitter", *World Conference on Photovoltaic Energy Conversion (WCPEC-7)*, 2018.

[3] Ebong, N. Bezawada, V. Unsur, R. Keming and A. Chowdhury, "Investigation of Telluride Based Fire through Dielectric (Ftd) Ag Pastes Contacts for Si Solar Cell with High Sheet Resistant Emitter", *7th Workshop on Metallization and Interconnection for Crystalline Silicon Solar Cells*, 2017

[4] A. Chowdhury, Y. Hsu, V. Unsur, and Aba Ebong, "Exploiting the Potentials of the Front Surface Field (FSF) Industrial Silicon Solar Cell", *44th IEEE Photovoltaic Specialists Conference (PVSC)*, 2017.

[5] V. Unsur, B. Hussain, and A. Ebong, "Complete Recovery of Light Induced Degradation of Cz Silicon Solar Cells with Rapid Thermal Processing", *43rd IEEE Photovoltaic Specialists Conference (PVSC)*, 2016.

[6] B. Hussain, A. Ali, V. Unsur and A. Ebong, "On Structural and Electrical Characterization of n-ZnO/p-Si Single Heterojunction Solar Cell", *43rd IEEE Photovoltaic Specialists Conference (PVSC)*, 2016.

[7] A. Ebong, N. Chen, V. Unsur, A. Chowdhury and B. Damiani, "Innovative Front Grid Design, Four-Streets and Five-Busbars (4S-5BB), for High Efficiency Industrial Al-BSF Silicon Solar Cell", IEEE Electron Device Letters vol. 37, no. 4, pp 459-462, 2016.

[8] V. Unsur, A Chowdhury, N. Chen and A. Ebong, "The Effects of Nano Ag Particles on Gridline Sintering for Silicon Solar Cells", *42nd IEEE Photovoltaic Specialists Conference (PVSC)*, 2015.

[9] K. Batchu, A. Ebong and V. Unsur, "The Impact of Ag Particle Size and Rapid Thermal Processing Belt Speed on Contact Resistance of a Silicon Solar Cell", *12th High Capacity Optical Networks and Enabling/Emerging Technologies (HONET)*, 2015.

[10] A. Ebong, N. Chen, A. Chowdhury, and V. Unsur, "The impact of rapid thermal processing (RTP) on crystalline silicon solar cell performance and light induced degradation (LID)", *42nd IEEE Photovoltaic Specialists Conference (PVSC)*, 2015.

[11] A. Ebong, V. Unsur, N. Chen, and A. Chowdhury, "Understanding the Sintering of Digital Inkjet Printed (DIP) Contacts to Achieve Low-Contact Resistance on Silicon Solar Cells", *1st Africa Photovoltaic Solar Energy Conference and Exhibition Proceedings*, 2014.

[12] N. Chen, A. Chowdhury, E. Ahmed, V. Unsur and A. Ebong, "Assessing the impact of multi-busbars on metallization cost and efficiency of solar cells with digital inkjet-printed gridlines", *High Capacity Optical Networks and Enabling/Emerging Technologies (HONET)*, 2013.